

**Master thesis : WHERE TENDONS MEET BONES STRUCTURAL AND
MECHANICAL ANALYSIS OF A CHILLES TENDON INSERTION INTO CALCANEUS**

Auteur : Tits, Alexandra

Promoteur(s) : Ruffoni, Davide; 3475

Faculté : Faculté des Sciences appliquées

Diplôme : Master en ingénieur civil biomédical, à finalité spécialisée

Année académique : 2017-2018

URI/URL : <http://hdl.handle.net/2268.2/4640>

Avertissement à l'attention des usagers :

Tous les documents placés en accès restreint sur le site MatheO sont protégés par le droit d'auteur. Par conséquent, seule une utilisation à des fins strictement privées, d'enseignement ou de recherche scientifique est autorisée conformément aux exceptions légales définies aux articles XI. 189 et XI. 190. du Code de droit économique. Toute autre forme d'exploitation (utilisation commerciale, diffusion sur le réseau Internet, reproduction à des fins publicitaires, ...) sans l'autorisation préalable de l'auteur est strictement interdite et constitutive de contrefaçon.

UNIVERSITY OF LIEGE
FACULTY OF APPLIED SCIENCES

UNIVERSITY OF AUCKLAND
AUCKLAND BIOENGINEERING INSTITUTE



WHERE TENDONS MEET BONES

STRUCTURAL AND MECHANICAL ANALYSIS OF ACHILLES TENDON INSERTION INTO CALCANEUS

Master thesis conducted by

ALEXANDRA TITS

with the aim of obtaining the degree of Master in Biomedical Engineering

SUPERVISOR
Davide Ruffoni

CO-SUPERVISOR
Justin Fernandez

Olivier Bruls Liesbet Geris
Jean-Francois Kaux Harry Van Lenthe

ACADEMIC YEAR 2017-2018

Abstract

Soft tissues such as tendons or ligaments are attaching to bone thanks to a multi-material interface exhibiting gradients in composition, structure, and mechanical components. This complex region is called enthesis and is able to efficiently transmit stresses between two materials displaying a mismatch in material properties of at least two orders of magnitude.

Musculoskeletal injuries are frequent and whenever they require the reattachment of soft tissue to bone, the failure rate is high, due the lack of integrative solutions for the repair of entheses. Therefore, an improvement in our understanding of mechanisms allowing those interfacial regions to reach their efficiency is still required for clinical purposes, but also regarding the development of biomimetic strategies for engineering practise.

This thesis proposes a new approach for the investigation of entheses functioning. Research has been mainly focused on understanding composition and structure of the interface, which is a very tiny region of about 500 [μm]. Our project aims at studying structural and mechanical adaptation of the bone beneath the insertion, with the main assumption that this region plays a pivotal role for facilitating the force transmission from tendon to bone. Our work is based on high resolution micro-computed tomography images of calcaneus bone of rats.

Bone morphology is first assessed by characterizing three features: bone porosity, anisotropy and the roughness at the surface. This analysis teaches us that porosity is gradually increasing from the insertion site to the interior of the bone. This gradual increase seems to be more controlled than when considering another location on the bone surface far from the insertion point. We also quantify that the insertion region shows significantly more anisotropy than the rest of the bone: bone micro-architecture seems to be well align with the loading coming from the tendon. Finally, we prove that the bone surface at the insertion is characterized by a significantly higher roughness than other locations. A higher surface roughness is known to increase the toughness of bimaterial interfaces.

Second, we develop a microstructural finite element model of the Achilles tendon and bone in order to evaluate biomechanical behavior arising from the interfacing of such dissimilar materials. It turns out that the transmission of the stresses from the tendon results in a non-trivial pattern within the bone, generating compression regions aligned with the trabeculae of the growth plate, and tension regions perpendicular to those ones. Tension regions are also found to be aligned with the micro-architecture located directly beneath the insertion, corroborating assumptions of a "line-of-force" between Achilles tendon insertion and the insertion of the plantar fascia located at the bottom of the foot. We also show that the material mismatch generates high, but localized, stresses at the interface. Finally, we demonstrate that the biological insertion is robust towards changes in the orientation of the force that may occur during the physiological range of motion. This concept is demonstrated by conducting a "thought" experiment consisting in comparing the behavior at the biological insertion with a "wrong" insertion located at the top of the bone.

Acknowledgements

It has been a first experience for me to conduct such a long term work that has also allowed me to be immersed in the world of experimentation and research. Defining my own project, from the questions to the tools used to answer them, has been highly challenging at times and I definitely would not have been able to complete this thesis without support.

First and foremost, I would like to express my gratitude to my supervisor Professor Davide Ruffoni for giving me the opportunity to work on such an exciting topic. I especially want to thank him for having been helpful and responsive (no matter the time delay) all along the achievement of this thesis. Besides from providing me indispensable advice, he has always been enthusiastic towards my work and supportive, even during setbacks.

The experimental part of this project has been conducted in Liege, Belgium, and I would like to thank personally all the persons that have contributed to it. First of all, I am grateful to Professor Alain Colige, his PhD student Laura Dupont and the biology laboratory of connective tissues, for providing me support and advice regarding the histological sections of the bone that we wanted to carry out. Even though we have not reached to expected results, they have been welcoming and helpful. Secondly, I am thankful to Professor Harry Van Lenthe for his perfect assistance regarding the μ CT scans. Besides providing the data we needed promptly and efficiently, he has been highly responsive and available whenever I had questions. However, those experimentations would not have been possible without rat samples. I would therefore like to mention the indispensable help of Professors Pierre Drion and Jean-François Kaux for the extraction of the samples and their valuable advice. They have been profoundly cooperating and have answered my questions all along this project. Finally, a special acknowledgment to Cristina Gatti and Laura Zorzetto without whom I would not have been able to conduct the last step of the experimental process.

The second part of this thesis has been conducted in Auckland, New Zealand. I am very appreciative to my co-supervisor Professor Justin Fernandez for sharing with me his expertise regarding the modeling side of this project, but also for giving me the opportunity to work in such an inspiring environment that is the Auckland Bioengineering Institute. It has been a pleasure to conduct my research surrounded by passionate and inspiring researchers. I would like to thank all the PhD students of the musculoskeletal modelling department for their enlightening opinions about my work, but also for the countless coffee breaks and discussions that have been an integral part of the achievement of my thesis.

Moreover, I am deeply grateful to my family that has provided unwavering moral support all along the ups and downs of this project. My thesis being also the conclusion of my five years of study, I feel particularly lucky that they have been so encouraging and stimulating during all this time, whichever way I went.

In closing, a special thanks to my boyfriend that has believed in me and encouraged me, no matter what, each and every time I had doubts or fears. I would not have made it without you.

Table of contents

Abstract	I
Acknowledgements	II
Introduction	1
1 Background	3
1.1 The musculoskeletal system	3
1.2 Soft-tissue-to-bone interface	9
1.3 Bone adaptation mechanisms	16
1.4 Main aims of the master thesis	21
2 Experimental part	22
2.1 Introduction	22
2.2 Sample preparation	22
2.3 Image acquisition	24
2.4 Discussion	26
3 Structural analysis	28
3.1 Introduction	28
3.2 Preliminary analyses	28
3.3 Methods	31
3.4 Results	44
3.5 Discussion and conclusions	51
4 Biomechanical study	53
4.1 Introduction	53
4.2 Methods	53
4.3 Results	61
4.4 Discussion and conclusions	68
5 Perspectives	70
5.1 Limitations	70
5.2 Future work	71
Conclusion	72
Appendices	73

Introduction

Entheses are complex biomaterial junctions able to effectively transfer stresses between very dissimilar materials. Those insertion sites fulfill the crucial role of integrating soft tissues, such as tendon or ligament, to hard tissue, meaning bone. Tensile Young's Modulus of tendons and ligaments have a range of values from minimum 0.03 in ligaments to maximum 2.3 [GPa] in tendons, whereas bone exhibits a value up to 20 [GPa]. This gap of at least two orders of magnitude is one the greatest interfacial material mismatches found in nature. Human body actually provides a great source of inspiration regarding attachment of dissimilar systems: interfaces responsible for tooth attachment is another example. Beyond the intellectual curiosity triggered by such an effective interfacial system, the study of this region is not only inspiring for biomimetic purposes, but has been shown to be clinically relevant.

Firstly, from what we know about interfacial engineering, such a mismatch should raise failure due to stress concentrations [61]. Thus joining dissimilar materials remains a challenge in engineering. Applications in various fields may require such a junction. For example, metal hip prostheses (and orthopedic joint implants in general), in addition to challenges of biocompatibility, may generate issues along the bondline between metal and bone. Indeed, it can cause pain, loosening of the implant and even failure [113]. In other engineering applications, there is also a high demand for new techniques of attachment of dissimilar materials like metals and polymers. Indeed, manufacturing of hybrid structures offer a wider range of properties and optimized versatility, whether it is for aerospace or automotive industries [61]. Current techniques of bolting or adhesive bonding may suffer from residual stresses, stress concentrations and even debonding. Typical example of adhesively bond systems are hybrid metal-composite structures, where properties of the materials used (metal, composite and adhesive) are highly dissimilar. Another example may be found in electronic packaging. Stresses may occur from the junction between the chip and substrate because of differential thermal expansion coefficients [113].

Secondly, it is known that musculoskeletal disorders weigh heavily on health budget. Among them, musculoskeletal injuries involving tendon or ligament rupture may require surgical reattachment back to bone. Most commonly injured entheses are the ones of the rotator cuff tendon, the torn anterior cruciate ligaments and the Achilles tendon. Such operations exhibit a high rate of failure because the enthesis rarely regenerates and does not recover its mechanical properties [71]. Surgical attempts for the rotator cuff tendon exhibits failure rates up to 94 % and cruciate ligament grafts are still painful for half of the patients treated. Regarding the Achilles tendon, even though 55 to 65 % of the cases of tendinopathy refer to mid-portion issues, 20 to 25 % of the disorders involve another type called insertional Achilles tendinopathy (IAT) and consists in a degeneration of tendon's insertion into the calcaneus. Treatment of IAT remains difficult: 25 % of the surgical attempts for reattachment do not show good results and complications include wound issues, infection and even tendon detachment [108]. This clinical issue is clearly due to a lack of understanding of the healthy attachment, as well as of the healing process that may occur in such regions.

However, even though IAT features a non negligible clinical occurrence, it is widely accepted that tendon ruptures are much more likely to occur than enthesis failures. Given what we know about attachment of dissimilar materials, enthesis should be the weak and failure-inducing region: how is it possible that is not the case? Answering that question may be intellectually as interesting as improving current surgical procedures for reattachment or engineering practises.

So far, research about entheses has been focused a lot on the understanding of the enthesis in itself, and specifically about

the study of structure and function at this location. In addition, mechanisms of failure minimization have been identified. Actually, it turns out that very little attention has been paid to the bone beneath the enthesis. Nonetheless, bone is known to exhibit amazing remodelling properties, and has already been shown to feature adaptation to mechanical loading and orientation [132, 100, 117, 102].

Therefore, given the high scientific interest in that region on one hand, and the lack of research regarding bone adaptation beneath insertion on the other hand, the question we have decided to address is the following: does calcaneus bone show structural and mechanical adaptation to the insertion of Achilles tendon ?

This thesis is divided into five main chapters. The first one is dedicated to the definition of the general context of the project. Basic notions about the biological entities considered in this thesis are provided. Also, more details are given about soft-tissue-to-bone interface, such as structure and function relationship, clinical relevance of studying it, current approaches for interface regeneration and main mechanisms allowing entheses to reach their efficiency. After, bone adaptation concepts are reminded in order to introduce the main aims of the master thesis in details.

Our second chapter focuses on the experimental part of the project, and describes how samples have been prepared as well as the procedure followed for image acquisition.

Chapter three describes the first part of our study: the structural analysis. Its aim is to investigate three features of bone morphology: porosity, anisotropy and roughness at the surface. Our purposes are introduced, and after preliminary analyses of our scans, the methodologies are explained in details. Results are then presented for the three parameters of interest. Afterwards, our procedure is discussed and the limitations are highlighted. Main conclusions are then summarized.

The fourth chapter provides information about the biomechanical study we have conducted. Indeed, after having investigated structural effects of the insertion of the tendon, the purpose is to evaluate the propagation and distribution of stresses within the bone and use information provided by our structural analysis to put those results into perspective. This chapter is also divided into an introduction, a description of the methods followed for the building of the model (in terms of geometry, meshing and boundary conditions), as well as a presentation and discussion of our main results. Main conclusions are also emphasized at the end of this chapter.

Our last chapter presents critical view on our results. General limitations of our approach are given, and ideas of improvement for future work are described.

Chapter 1

Background

The aim of this chapter is to provide the general context of the project. In the first section, basic biological notions of the musculoskeletal system are presented. Then, we review the current knowledge about the soft-tissue-to-bone interface: its structure and function, but also the clinical relevancy of studying that region, as well as current approaches for interface regeneration. After having introduced our research questions, further details about the concepts behind bone adaptation, required to better understand the approach followed in the study, are given. Finally, the main contributions of this master thesis are presented.

1.1 The musculoskeletal system

In this section, we remind the basics of the biological entities we deal with in this thesis.

The human musculoskeletal system may be defined as an incredibly complex system allowing us to achieve a task we are however perceiving as completely effortless and ordinary: moving. Besides locomotion, it also provides form, support, protection and stability to the human body. Its major components are bones, muscles, cartilage, tendons, ligaments and joints.

As the main focus of this thesis is on the insertion of soft tissues into bone, called enthesis, we present in more details the key players of this system: bone, tendons, ligaments, and cartilage. The final part of this section is dedicated to the description of the specific entities considered in our study.

1.1.1 Bones

Bones come in various shapes and sizes. Light and yet strong, they accomplish vital functions for the human body thanks to a fine hierarchical structure down to the nanoscale. At the nanoscale, bone is a composite material featuring a protein matrix reinforced by mineral crystals. Bone is also a cellular material with a porous inner structure going from nanometers to millimeters. The aim of this section is to provide a brief description of bone structure and function.

► Structure

Bone structure may be described at different levels. Essentially, bone is composed of three major components: an organic phase (basically collagen and other proteins), an inorganic phase (mainly hydroxyapatite minerals that form platelets between collagen fibers), and water. Table 1.1 shows the proportion of each constituents. The crystalline complex provides hardness and rigidity to bones, whereas collagen fibers provide elasticity and toughness [38].

► Role

As already said, bones serve multiple functions. From a biomechanical point of view, their rigidity provides support to the

	Inorganic phase (mineral crystals)	Organic phase (proteins)	Water
BONE	60 [%]	30 [%]	10 [%]

Table 1.1: Relative amounts of constituents in bone (% of wet weight), in humans [101].

musculoskeletal system and allows motion. They also protect various organs of the body. However, in addition to that, bones serve vital biological roles such as the storage of calcium and phosphorus and they contain critical components of the hematopoietic system, which is the machinery forming red blood cells. Regarding mineral storage, it is interesting to notice that bones contain 99% of the whole body calcium. As we will see later, bones are regulating level of calcium in bloodstream thanks to a continuous remodelling of bone tissue [27].

1.1.2 Tendons and ligaments

Tendons and ligaments are both fibrous connective tissues, "keeping together" of the whole musculoskeletal system. Tendon attaches muscles to bone, whereas ligaments connect bone to bone. The knee complex allows us to illustrate both tendon and ligament at the same location, as can be seen in Figure 1.1. Although quite similar, they have specific functions to accomplish. Tendons and ligaments also have the same basic components but their structure varies slightly, leading to distinct material properties [12].

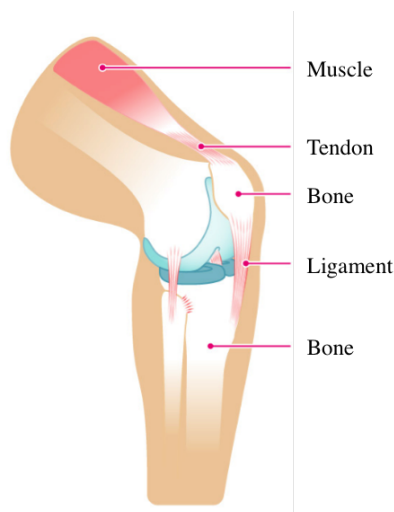


Figure 1.1: Schematic illustration of a tendon and a ligament in the knee joint (adapted from [24]).

► Structure

Tendons and ligaments are both made of water, collagen, elastin and proteoglycans. Therefore, the constituents are similar but the relative amounts differ, as shown in Table 1.2 .

Moreover, as it is the case for many biological tissues (such as bone), they exhibit a hierarchical structure obviously essential for their mechanical behavior. Figure 1.2 shows this hierarchy as well as the main length scales for tendons (ligaments have a similar

	Collagen	Elastin	Proteoglycans
TENDONS	75-85 [%]	1-3 [%]	1-2 [%]
LIGAMENTS	70-80 [%]	1-15 [%]	1-3 [%]

Table 1.2: Relative amounts of constituents in tendons and ligaments (% of dry weight) in humans [101].

structure). First, the largest structure refers to the tendon or ligament itself. Then, they are split in substructures called fascicles. Fascicles contain the basic unit of the tendon or ligament, the fibers, as well as tenocytes (elongated fibroblast type cells). Fibers themselves contain the collagen fibrils that interact with each other through proteoglycans.

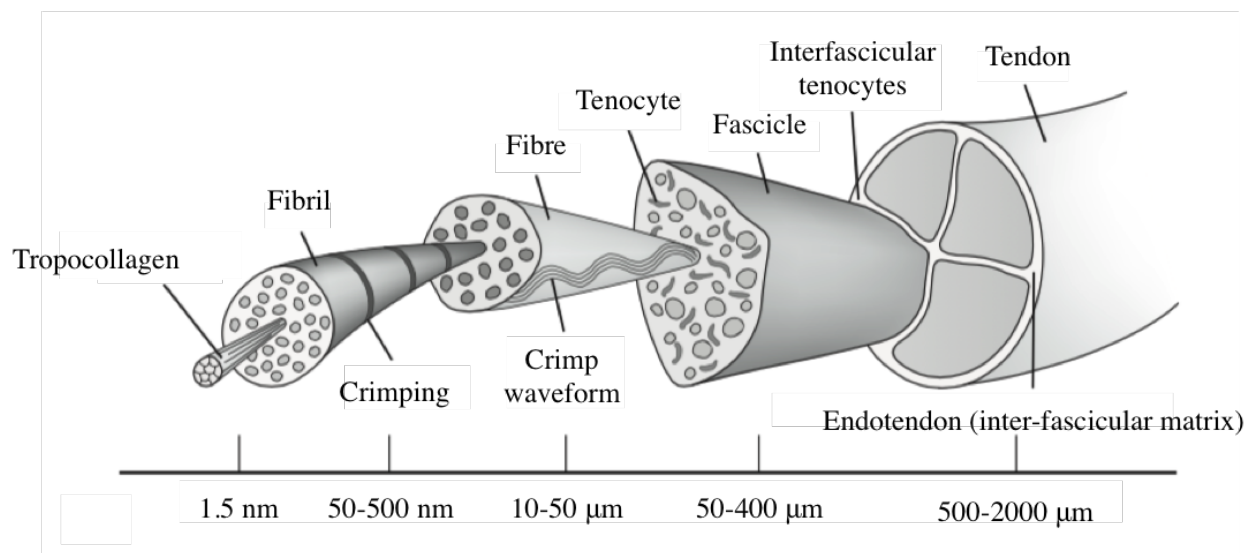


Figure 1.2: Hierarchical structure of tendons, showing fiber organization from nanoscale up to milliscale (adapted from [93]).

The main difference between tendons and ligaments is related to the degree of alignment of fibrils and fascicles. The presence of substantial waviness has been shown in the fibrils of ligaments, whereas fibrils of tendon are more straight. Also, in ligaments, the fascicles are not always parallel to the main orientation but can show substantial twist [101].

Mechanical properties of tendons and ligaments show strong dependence on biological and experimental factors such as anatomical site, age, and strain rate. However, one can determine a range of values for the tensile Young's modulus extending from 30 to 500 [MPa] for ligaments and from 60 to 2300 [MPa] for tendons (in humans) [101].

► Role

Loaded in series with muscles, the role of a tendon is to move the bone it is attached to. Although tendons are tissues, meaning they transmit force without actively producing work, they are very efficient at storing only minimal amounts of deformation energy which is almost entirely recovered. This avoids that work produced by muscles is dissipated in deforming the tendon [101].

Ligaments are believed to provide the stability of joints, by controlling the range of motion and restricting specific movements.

Forces involved are small (but get higher close to the full range of motion, [101]).

1.1.3 Cartilage

Cartilage is another tissue of the musculoskeletal system worth mentioning. It covers and protects the ends of long bones at the joints and is also a structural element of several body components [123]. Its stiffness and flexibility lies between the ones of bone and muscles. Cartilage is classified into three different types, depending on the amount of its constituents: elastic cartilage, hyaline cartilage and fibrocartilage.

► Structure

Cartilage cells are called chondrocytes. They produce the main constituents: proteoglycan and elastin. Cartilage of the knee joint can be spotted in Figure 1.3.

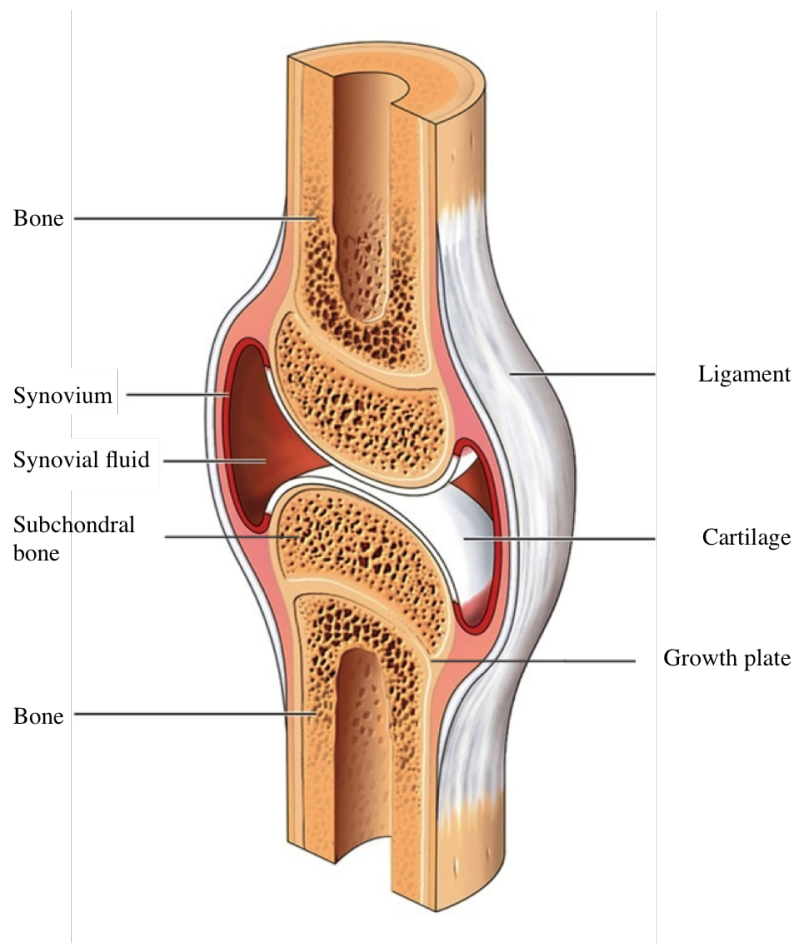


Figure 1.3: Schematic representation of the knee joint components showing cartilage and subchondral bone (adapted from [85]).

► Role

Cartilage serves many different functions [13]. In joints, hyaline cartilage (also called articular cartilage) plays the role of a cushion, preventing bones from rubbing onto each other and facilitating shock absorption. Elastic cartilage is the most flexible one because it contains more elastin. It is used for "holding tubes open" in the body (such as the trachea). Finally, fibrocartilage is the strongest and the most rigid type of cartilage because of its higher amount in collagen. Fibrocartilage is found in interver-

tebral disks and, as we will see in subsection 1.2.1, in the insertion of tendons and ligaments into bone. Fibrocartilage is usually present at regions submitted to high shear and compressive stresses.

1.1.4 Region of interest

In this thesis, we focus our interest on a particular anatomical site, meaning a specific tendon, bone and cartilage. Indeed, we have decided to study the insertion of Achilles tendon into the calcaneus bone. Therefore, a few reminders about ankle anatomy are provided, as well as the specificities of this bone and tendon. Also, we are working with an animal model: a rat. Therefore, a brief parallel between human and rat anatomy is drawn.

► Ankle anatomy

We broadly refer to the "ankle" as the region where the foot and the leg meet. This region includes several joints, among them the most used during walking are the talocrural joint (medical terminology of what we usually refer to when mentioning "ankle"), the subtalar joint and the transverse tarsal joint. The main bones of the ankle region are the tibia and fibula (in the leg) and the talus and calcaneus (in the foot). Those joints and bones are shown in Figure 1.4 for humans. Rat ankle is anatomically similar to human ankle in terms of bones, joints and main tendons.

Regarding ligaments and tendons, they are numerous at the ankle joint. We will thus focus on the ones directly attaching to the calcaneus in the following paragraph.

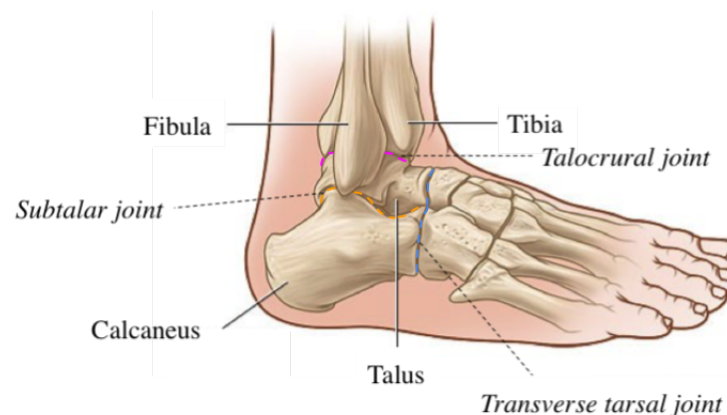


Figure 1.4: Lateral schematic view of the biggest bones and main joints of the ankle region (adapted from [53]).

► The calcaneus

The calcaneus is the largest bone of the foot and forms the prominence of the heel. It is covered with six surfaces (anterior, posterior, superior, plantar, lateral and medial), being either articular and non-articular. On the posterior surface, the calcaneus receives the insertion of the Achilles tendon at the posterior calcaneal tuberosity [78]. This tuberosity can be observed in Figure 1.5. On the plantar surface, there is a prominence at the bottom, called the medial calcaneal tuberosity. From this tuberosity runs the plantar fascia, gathering several ligaments reaching the metatarsal bones. This fascia is also shown in Figure 1.5. In addition, many other smaller ligaments attach to the calcaneus, such as the bifurcate ligament on the dorsal surface, or the calcaneofibular ligament on the lateral side.

Although rats are known to exhibit the same constituents (joints, bone and connective tissues), one observation can be made regarding the orientation of calcaneus at rest. Indeed, human calcaneus is pointing downwards whereas X-rays of rat ankles

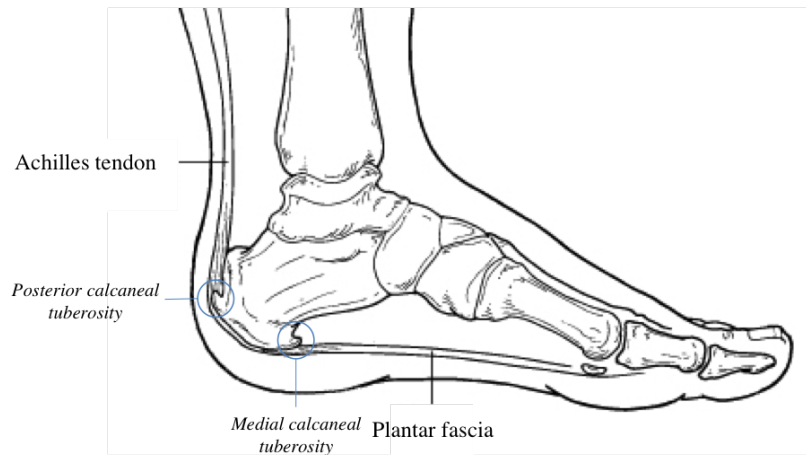


Figure 1.5: Simplified lateral view of human ankle showing Achilles tendon and plantar fascia attachments into the calcaneus [94].

indicates a rather flat orientation. Comparison is illustrated in Figure 1.6.

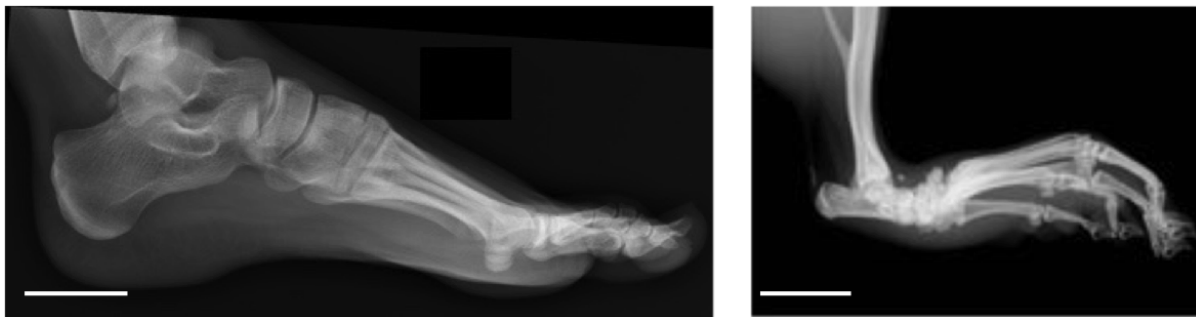


Figure 1.6: Comparison of an ankle lateral X-ray in human (left, [95]) and rat (right, [23]). Scale bars: 5 [cm] (for the human foot) and 0.5 [cm] (for the rat foot).

► The Achilles tendon

The Achilles tendon, also called calcaneal tendon (*tendo calcaneus*) is a tendon inserting into the calcaneus at the back of the leg. It is the thickest in human body [126]. The Achilles tendon is attaching muscles to the calcaneus. As shown in Figure 1.7, those ones are the gastrocnemius, soleus, and the plantaris muscles. Notice that the plantaris may also have its own independent insertion into the calcaneus (it depends from one individual to another). The group of soleus and the two heads of gastrocnemius may be referred to as "triceps surae". Achilles tendon is surrounded by a thin sheath of tissue, called the paratenon that allows the tendon to glide relative to adjacent structures [11]. Two bursae also assist the tendon in its motion: the superficial bursa, located between the skin and the tendon, and the retrocalcaneal bursa between the tendon and the superior calcaneal tuberosity. Those two are shown in Figure 1.8. Similar building principles may be found in rats. As we will see in the next paragraph, the activity of those muscles, transmitted by the tendon, allows the flexion of the foot.

► Ankle motion

Plantar flexor muscles induce joint movements that make the foot move. The two main (or most used) motions are shown

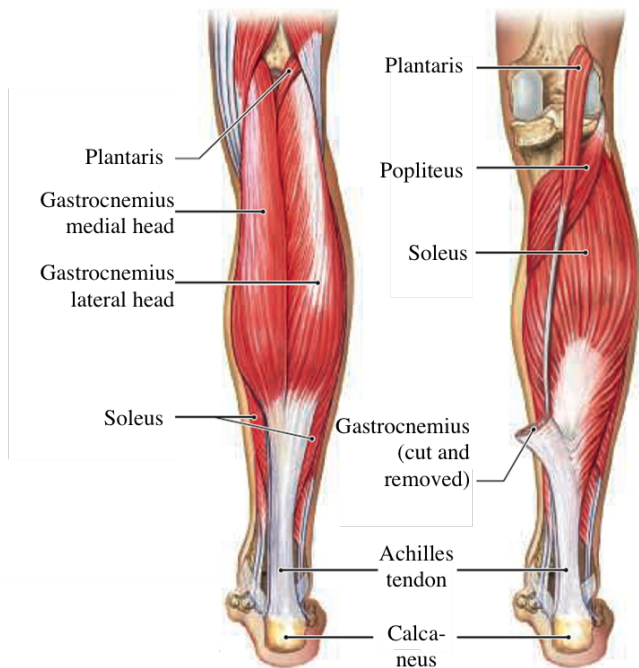


Figure 1.7: Schematic illustration of the calf muscles inserting into the Achilles tendon in humans (adapted from [48]).

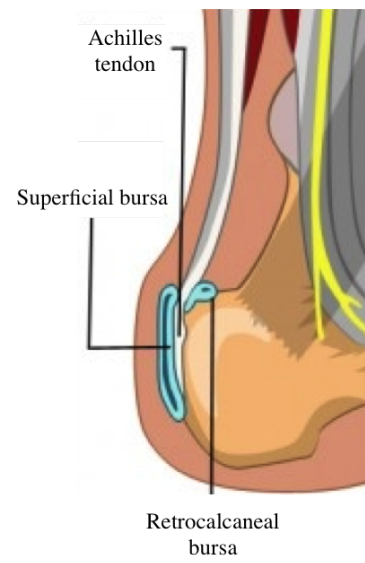


Figure 1.8: Schematic representation of the superficial and retrocalcaneal bursa (adapted from [107]).

in Figure 1.9. Dorsiflexion and plantarflexion consists in rotation around the ankle joint in the sagittal plane. Eversion and inversion are allowed by subtalar joint and transverse tarsal joint. This motion is induced when walking on uneven surfaces for example. The most solicited joint during walking is the ankle joint and is resulting in the stretching of the Achilles tendon [92].

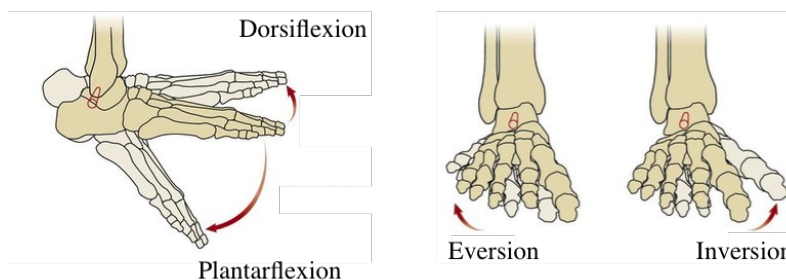


Figure 1.9: Schematic illustration of the main ankle motions (adapted from [82]).

Rats are quadrupeds, therefore, their locomotion is very different from the one of humans. However, dorsi- and plantarflexion of the ankle are also predominant when walking, and therefore stretching remains one of the main solicitation undergone by the Achilles tendon during normal gait.

1.2 Soft-tissue-to-bone interface

This project aims at studying the insertion of soft tissues (tendons and ligaments) into bone, and the corresponding bone adaptation. This region, called enthesis, is a complex biomaterial junction that is able to effectively transfer stresses between very dissimilar materials. Indeed, tensile Young's Modulus of tendons and ligaments have a range of values from minimum 0.03 in ligaments to maximum 2.3 [GPa] in tendons, whereas bone exhibits up to 20 [GPa]. This variation of at least two orders of

magnitude is one of the greatest interfacial material mismatches found in nature. For what we know about junctions between mechanically dissimilar materials, huge stress concentrations could be present, which would increase risk of failures [114]. However, entheses are somehow able to bear loads of multiple body weight [99]. Beyond the intellectual curiosity triggered by such a seemingly illogical but yet effective interfacial system, the study of this region has been shown to be clinically relevant and is also inspiring for biomimetic purposes.

In this section, we start with a short description of what is known regarding structure and function of the enthesis. Then, we describe the three clinically most relevant entheses, focusing more on Achilles tendon pathologies. Then, approaches for interface regeneration are presented. Finally, we present the current progress in understanding of the mechanisms that nature uses to minimize failure at the interface.

1.2.1 Structure and function of the enthesis

The proper functioning of the musculoskeletal system depends on the coordinated action of multiple types of tissues. This coordinated action is ensured thanks to entheses. In comparison to the vast literature on bones, tendons and other parts of the musculoskeletal system, very little is known on this interface region. Those insertion sites fulfill the role of integrating soft tissues, such as tendon or ligament, to hard tissue, meaning bone. Given the huge mismatch in the mechanical properties of those two types of tissue, this role is anything but easy and those regions have triggered research in order to understand how nature allows the effective transfer between mechanically dissimilar materials. We see in details in subsection 1.2.4 the progress of the scientific community in the understanding of this efficient region.

Papers describing entheses generally focus on one type of soft tissue: either ligaments [81, 110, 135]), tendons [88, 41, 69, 54, 99, 80], or meniscus [2]. Meniscus is a cartilaginous tissue providing structural integrity to the knee.

Entheses may be classified into two groups based on their morphology: indirect or direct. Indirect or "fibrous" insertions means that the soft tissue approaches the bone with an acute angle, over large areas, and via fibers projecting in the bone [135, 72]. It is for example the case of the medial collateral ligament insertion to the tibia, or the deltoid tendon attachment to the humeral head. Direct or "fibrocartilaginous" insertions are more common and refer to a gradual and continuous transition between soft and rigid tissue that can be divided into four distinct zones [135, 72]:

- Zone I refers to the actual tendon, ligament or meniscus;
- Zone II is made of unmineralized fibrocartilage;
- Zone III is mineralized fibrocartilage;
- Zone IV is proper bone.

The border between the two fibrocartilaginous region can be seen on histological sections thanks to a "tidemark" representing the calcification front [115]. With this type of insertion, the soft tissue is known to approach the bone with a high angle [135]. It can be found in bony attachments of the rotator cuff tendons, the anterior cruciate ligament, and also the Achilles tendon. Table 1.3 shows the constituents of each zone. Figures 1.10b and 1.10a show stained sections of tendinous and ligamentous insertions, and Figure 1.10c illustrates the evolution of the constitutive components along the insertion.

Those are general features and characteristics that are taken for granted among all studies. Notice that size, alignment, and footprint of the entheses depends on the loading requirements of the specific attachment. Besides, it is recognized that the mechanical environment of entheses is complex, as it combines tensile, compressive and shear forces [72].

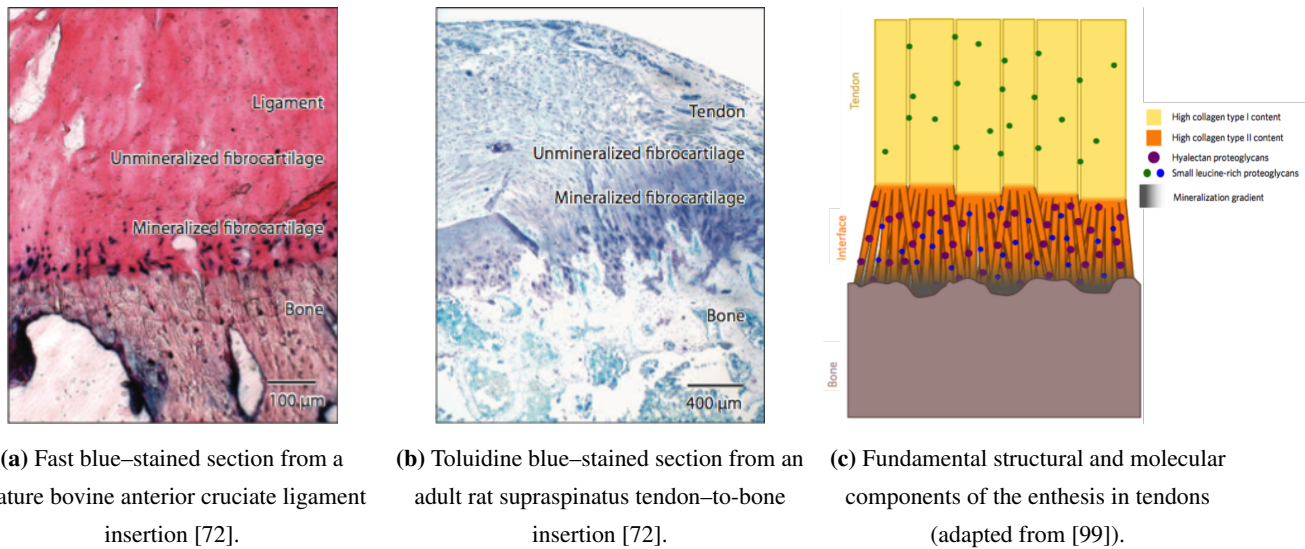


Figure 1.10: Illustrations of the typical four zones of insertions: stained sections of tendon (a), ligament (b), and explanatory attachment sketch (c).

	Tissue type	Constituents
ZONE I	Tendon / Ligament / Meniscus	Fibroblasts, linearly arranged collagen type I
ZONE II	Unmineralized fibrocartilage	Fibrochondrocytes, types I, II and III collagen, aggrecan
ZONE III	Mineralized fibrocartilage	Fibrochondrocytes, mineralized fibrocartilage, type II collagen, type X, aggrecan
ZONE IV	Bone	Osteoblasts, osteocytes, osteoclasts, mineralized type I collagen

Table 1.3: Specific components found in the four regions characterizing the insertion [72].

Fibrochondrocytes are typical fibrocartilage cells. Over 90 % of the collagen in the human body is type I [131]. However, several types of collagen have been defined because of differences in its specific structure. Finally, aggrecan is a type of proteoglycan found in cartilage.

1.2.2 Clinical relevance

In this subsection, we demonstrate why the insertion of soft tissues into bone is relevant from a clinical perspective.

First of all, it is known that musculoskeletal disorders weigh heavily on related costs of health budget. Musculoskeletal injuries involving tendon or ligament rupture may require surgical reattachment back to bone. Such operations exhibit a high rate of failure because the enthesis rarely regenerates and does not recover its mechanical properties [71]. This clinical issue is clearly due to a lack of understanding of the healthy attachment, as well as of the healing process that may occur in such regions. In the following paragraphs are presented the most commonly injured entheses and their associated surgical complications.

► Rotator cuff ruptures

First of all, in the shoulder, rotator cuff tendon (shown in Figure 1.11a) ruptures typically require surgical reattachment to its bony insertion (here, the humeral head). In such situations, scar tissue fills the repair site [69] and the enthesis does not regenerate properly. This results in a region highly prone to re-injury: failure rates range from 20 to 94% depending on the severity of the case and the patient's age [40].

► Torn anterior cruciate ligaments

In the knee, similar issues occur in the case of torn cruciate ligaments (see in Figure 1.11b). This injury is as frequent as 200 000 cases per year in the US [127]. It may often require reconstruction using tendon grafts [72]. However, approximately half of the patients experience knee pain one year post surgery [28]. Moreover, graft stability is compromised by the lack of proper regeneration at the insertion and long-term clinical outcome are still controversial [39, 98].

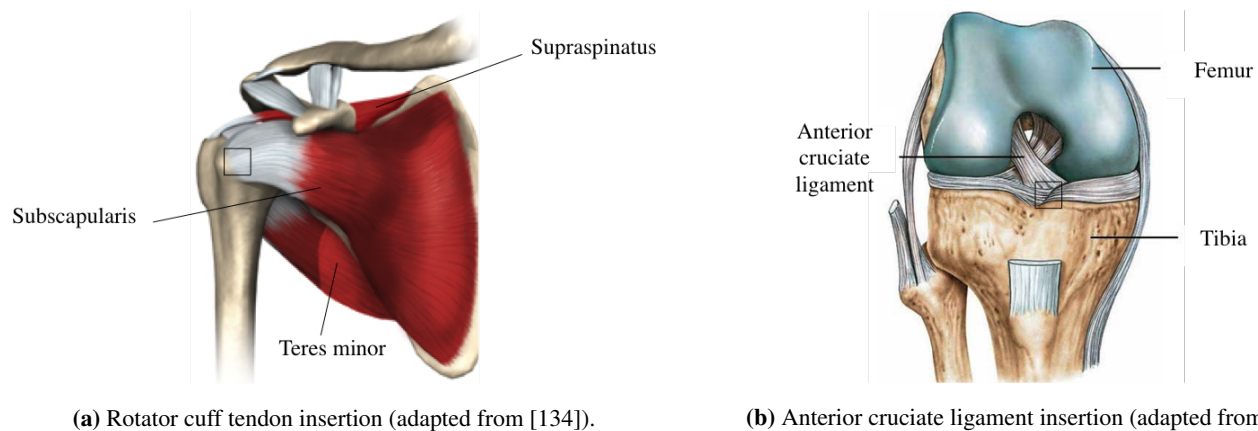


Figure 1.11: Schematic representation of a tendon (a) and ligament (b) insertion (localised with squares), respectively in the shoulder and knee joint.

► Achilles tendinopathy

Rotator cuff tendon and anterior cruciate ligament are the main focus among previous insertions studies. This project concentrates rather on Achilles tendon attachment to calcaneus. That being said, progress in the understanding of enthesis structure and function at one location may be enlightening for other sites as well.

In this paragraph, we describe in more details the pathology of this anatomical region. Indeed, the most common diseases of the Achilles tendon are overuse syndromes, not only among athletes but more generally among active people [119]. Runners exhibit an annual incidence of disorders of the Achilles tendon of 7 to 9 % [73].

When mentioning Achilles tendinopathy, one usually refers to mid-portion regions (also called non-insertional tendinopathy, NAT) and insertional tendinopathy (IAT) gets forgotten. However, if the first one is indeed more frequent (55-65% of the cases), 20 to 25% of Achilles's tendon disorders involve this second type and therefore occurs at the insertion into the calcaneus [34]. Insertional Achilles tendinosis consists in a degeneration of the collagen fibers that insert into the calcaneus. The cause is again mechanical overuse. In the acute state, clinical symptoms may be noticed such as pain and movement restriction [37], [89]. This pathology may come along with other complications such as Haglund deformity, calcification or thickening of the Achilles tendon. Haglund deformity consists in an enlargement of the posterosuperior prominence of the calcaneus, resulting in a mechanical irritation of the Achilles tendon. A typical X-ray is shown in Figure 1.12a. This may lead to an inflammation of the bursa called a bursitis, as shown in the schematic representation in Figure 1.12b. This pathology is said to coexist with IAT in 60 % of the patients [26]. However, the correlation with IAT is not really clear [62], and patients may exhibit Haglund deformity without having an IAT. Calcification, and specifically calcific spurs, occasionally grow from the calcaneal insertion. X-ray showing calcification of the insertion is presented in Figure 1.12c. In such case, we may refer to the patient's condition as insertional calcific

tendinopathy [59]. Finally, thickening of the Achilles tendon may be observed on MRI of IAT patients.

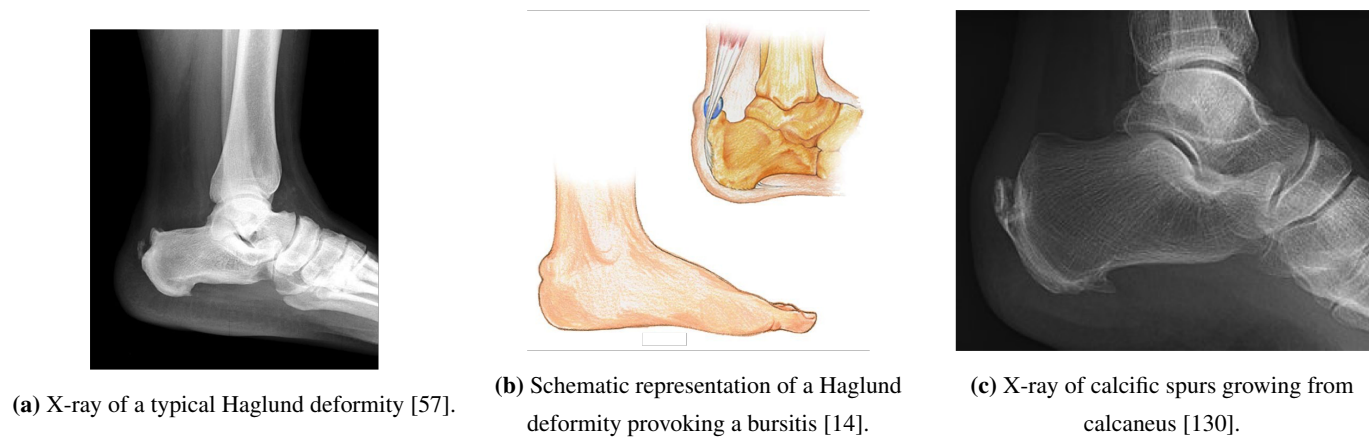


Figure 1.12: Complications often associated with IAT.

Options for treatment of IAT are either non-surgical or surgical. Conservative non-surgical attempts include drugs, stretching, rest or elevate leg. If this is not enough, cast or brace may be necessary [89].

If conservative treatment fails, surgery may be considered. Information about the whole procedure is hard to find in literature, also because of the controversy regarding efficiency of such an operation. However, it is likely that the surgery implies the removal of the degenerative parts of the tendon, as well as any bony part in case of Haglund deformity and the bursa if inflammation has occurred. The most common technique is called calcaneal osteotomy and consists in the debridement of the insertion zone [89]. Lengthening of the tendon may also be required, depending on how advanced the disease is [108]. Several techniques exist regarding the reattachment of the tendon to the bone [89]. Although some of those procedures show good results, there is no clear agreement regarding the best one in terms of success and complications. Moreover, good recovery only cover 75 % of the cases. Complications may include wound healing issues, infection and tendon detachment [108].

If treatment of IAT remains difficult, it is of course because its underlying mechanisms are not well mastered and because enthesis structure and function are not yet fully understood. Therefore, treatments of Achilles tendinopathy are more efficient for NAT than for IAT [34]. This triggers the need for a better understanding of Achilles tendon bony insertion.

One additional comment may be made regarding the surgical intervention in case of IAT. Indeed, it must be acknowledge that the removal of Haglund's deformity will potentially lead to an increase in stress concentration at the enthesis [11]. Indeed, in dorsiflexion, the tendon presses the calcaneal tuberosity and this actually helps to reduce stresses at the interface. Removal of the bony tuberosity should therefore be considered twice in such a surgery.

However, one can also look at the problem from a different perspective. Indeed, even though IAT features a non negligible clinical occurrence, it is widely accepted that tendon ruptures are much more likely to occur than enthesis failures. Given what we know about attachment of dissimilar materials, enthesis should be the weak and failure-inducing region: how is it possible that is not the case? Answering that question may be intellectually as interesting as improving current surgical procedures for reattachment, and also inspiring for other fields of engineering. Better understanding the mechanisms providing efficiency to this biological system could be useful for various applications (from metal hip prostheses to adhesive bond systems).

1.2.3 Current approaches for interface regeneration

Given the clinical relevance of the interfaces, there is an interest in scientific community in trying to regenerate them. Attempts currently include tissue engineering (TE) techniques. This means using combination of cells, growth factors and biomaterials to mimic the natural tissues. The optimal strategy would be to have spatial control over mineral distribution within the biomaterial (typically a stratified or multiphased scaffold [72]). Other challenges have also to be addressed such as osteointegration as well as effectively reaching the functional gradient of mechanical properties as in native interfaces. An example of a stratified scaffold is shown in Figure 1.13 (in the case of ligaments).

Thus the first problem to tackle when considering tissue engineered interfaces is the pre-engineering of the scaffold in order to reach multiphase scaffold design. Then a cell-based approach should be followed in order to really mimic to complex organization of the native interface [72]. However, many challenges remain before those TE approaches can be applied clinically.

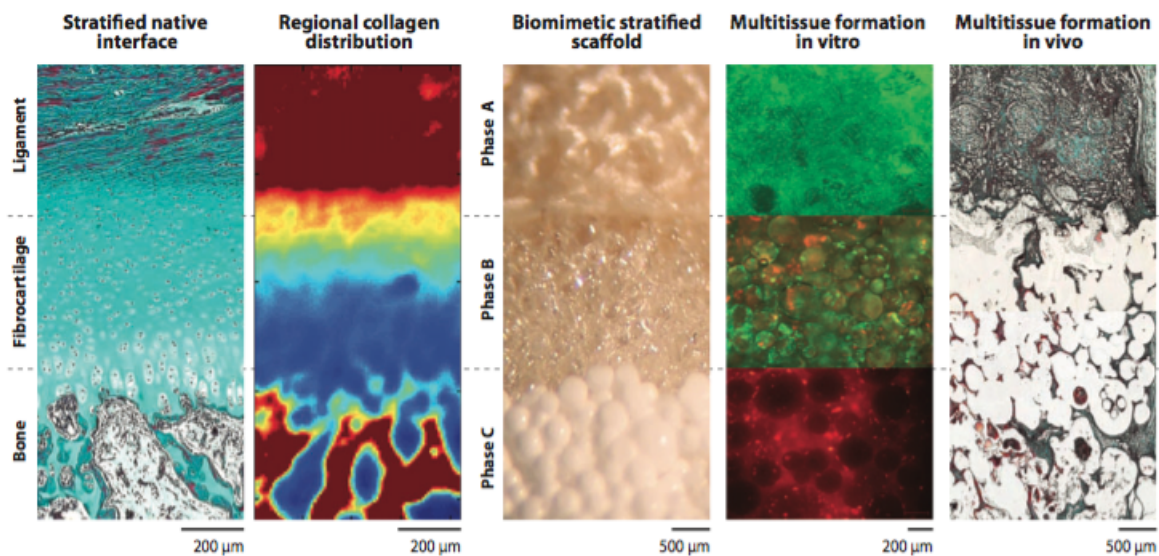


Figure 1.13: Illustration of a biomimetic strategy for engineering a ligament-to-bone interface [72].

The first two figures exhibit the features of the native enthesis (stratification and variation in collagen distribution) that have to be mimicked. Last three figures show the biomimetic stratified scaffold. The use of a triphasic scaffold (Phase A-B-C in the third figure) combined with a spatial control over cell distribution results in the formation of a multitissue both *in vitro* (fourth figure) and *in vivo* (fifth figure).

1.2.4 State of the art

In order to better understand diseased interface, and thus to improve current surgical options and interface regeneration approaches, research has been focused on healthy interface, referred to as a gold standard. Although studies all agree about the 4 regions organization of the enthesis, scientists are still trying to understand how this arrangement is leading to such an efficient transfer of stresses. Regarding tendons, four strategies have been proved to contribute to the efficiency of the insertion site [69].

Those strategies include a shallow attachment angle at the insertion and an optimization of the shape of the outward splay. The aim of those first features is to improve resistance to mechanical loads by reducing stress concentrations.

Secondly, interdigitations of the bone within the tendon have been shown to be efficient for toughening purposes, more than for reducing stress concentrations. Interdigitations can be described as wave-like structures with specific amplitudes and wavelength. They can be seen clearly in Figure 1.10b. Biological values of those two parameters allow a gain in toughness overcoming the loss in strength, a better distribution of stresses and a greater fraction of tissue implied in toughness mechanism [54]. It has also

been suggested that one issue in tendon repair could be that the insertion mechanism lacks of interlocking: this could show the importance of interdigitations for the toughness of the attachment [80].

Finally, a functional grading of transitional tissue between tendon and bone is modulating the stress field. This grading originates from the fibrocartilaginous region cited here above and operates at distinct levels: in the mineralisation, in the density of collagen fibers and in their organization [41, 133]. It has also been discovered that the combination of those three factors leads to an intermediate zone more compliant than either tendon or bone [116]. Mathematical models and optimization methods confirmed that such a region is useful to reduce and even eliminate stress concentrations [70, 41, 99]. Figures 1.14a, 1.14b and 1.14c show the main results of mathematical modelling to understand the role of compositional and structural gradients (if the materials to be connected are anisotropic). Notice that those strategies are of direct interest for engineering applications [113].

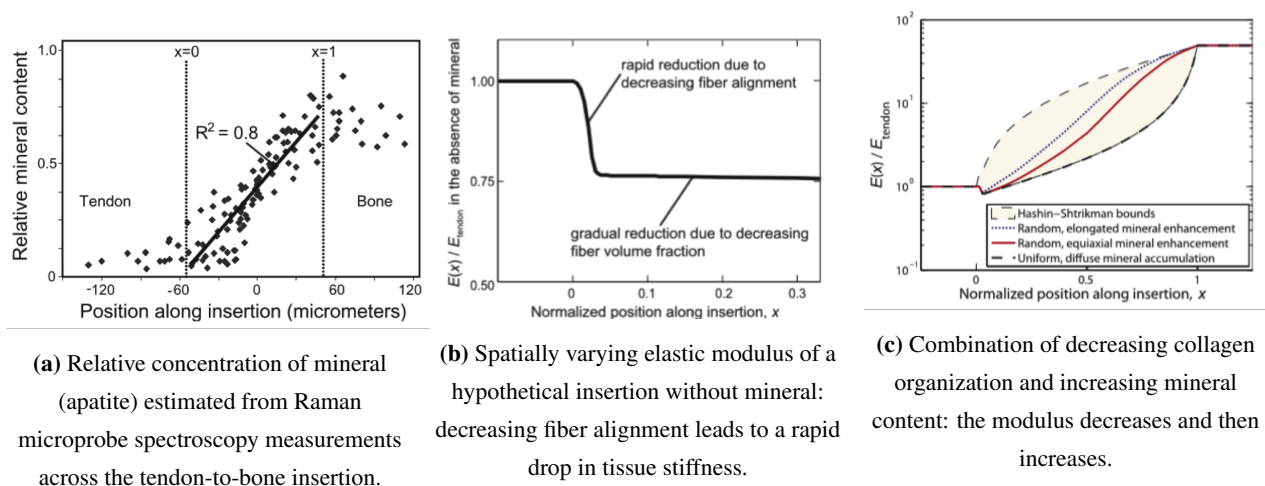
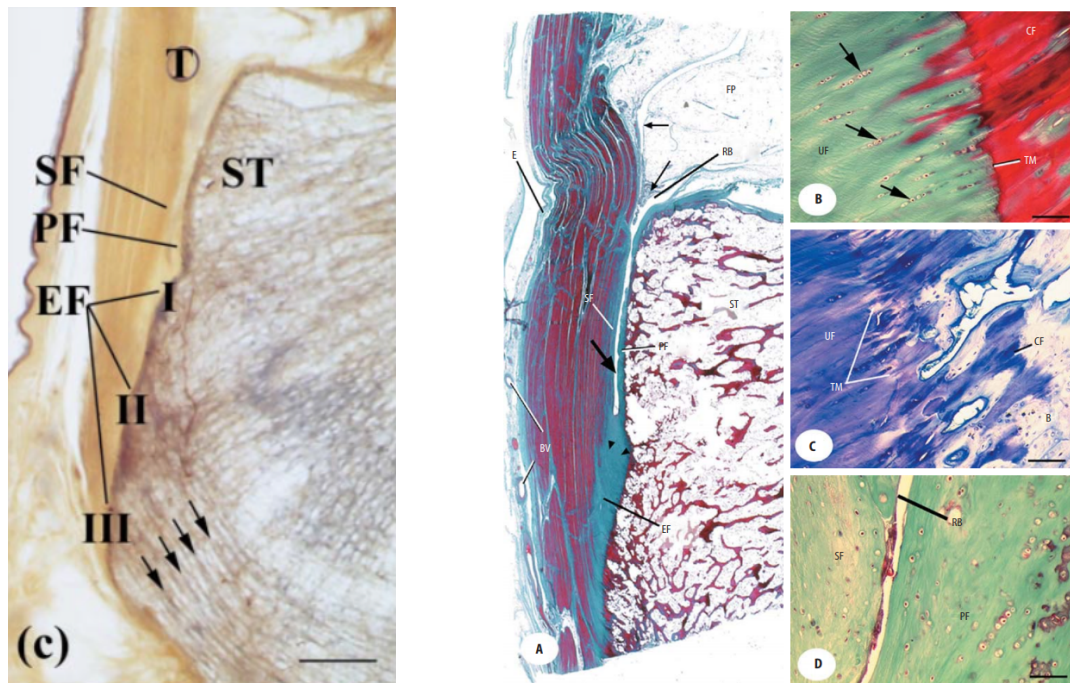


Figure 1.14: Proposed model aiming at better understanding the role of compositional and structural gradients [41].

Regarding Achilles tendon, a few additional observations can be made. Indeed, its insertion into calcaneus is particular: tendon is not in contact with calcaneus only at the insertion site, and this has lead to structural specializations at bone surface and more precisely additional fibrocartilage (FC) called periosteal and sesamoid. Thus, rather than enthesis, the term of "enthesis organ" is used and refers to the enthesis itself, periosteal and sesamoid FC, as well as retrocalcaneal bursa and fat pad [11, 80]. This one can be defined as a collection of tissues that assists the interaction between tendon and bone. Sesamoid FC is located in the deep surface of the tendon and periosteal FC covers the posterior calcaneal tuberosity. The main function of those FC is to serve as articular cartilage and they are therefore subject to compression in case of dorsiflexion of the foot. Those specific FC are shown in Figures 1.15a and 1.15b, as well as the traditional regions described here above.

Finally, we have already introduced the fact that our study will be based on rats rather than humans and we now try to justify briefly that choice. Because our model will be experimental based, ethical reasons are obviously our main justification. Moreover, their size also allows easier manipulation for experiments: neither too small (mice might be harder to operate) nor cumbersome. However, the understanding the behavior of rat musculoskeletal model might be enlightening at human level as well. Indeed, rats have been the first mammalian species to be used in laboratories, due to their physiological similarity to humans. Moreover, they have a bony architecture similar to that of humans [118], which makes them very suitable for the study of soft tissues insertion into bone. In addition, rat has been shown to be the most appropriate animal model for human rotator cuff tendon pathology [109]. Also, several studies have demonstrated the utility of rat models for developing strategies to enhance healing in tendons [43], [42], [112]. Those successful previous studies enable us to believe that a rat model can help us understanding human structures. However, one must not forget that the predictive aspect of rat models is controversial, especially regarding reactions to drugs and chemicals [104]. That being said, caution is advised when extrapolating conclusions from rat model up to human



(a) Unstained resin section. Notice that zones I, II and III correspond to regions used for the reconstruction purposes in the original paper. ST stands for superior tuberosity. Arrows show the orientation of trabeculae (this will be discussed in Section 1.4).

Scale bar = 0.5 [cm] [80].

(b) Sections stained with Masson's trichrome except toluidine blue staining for (C).

(A) Low power section. (B-C) High power views of the enthesis fibrocartilage. (D) High power view of the distal part of the retrocalcaneal bursa

Scale bars (A) = 2 [mm], (B-D) = 100 [μ m] [11].

Figure 1.15: Sagittal views of the posterior part of the calcaneus showing the enthesis organ, with the enthesis (EF), periosteal (PF) and sesamoid (SF) fibrocartilages. RB = Retrocalcaneal bursa, FP = Fat pad, E = epitenon, BV = blood vessels, TM = tidemark, UF = uncalcified fibrocartilage, CF = zone of calcified fibrocartilage.

level.

1.3 Bone adaptation mechanisms

As it can be noticed from the previous subsections, major part of the efforts developed to better understand entheses has been placed in either the interface itself or on the region coming from the tendon. We have decided to focus on the bone it. Before going into the details of our research question, this section describes in more details bone structure and its adaptation mechanisms. Indeed, those concepts are required to understand the approach followed in this project.

1.3.1 Types of bone

Bone is composed of two different types of tissues : cortical or compact bone and trabecular or cancellous bone. Figure 1.16 shows the hierarchical nature of cortical and trabecular bone along with the scale at which each level may be investigated and how. While the first one consists in a outer layer, strong and tough, the second one refers to an inner region lighter and very much less dense. Although they have the same basic constituent, that is mineralized collagen fibrils, trabecular and cortical bones exhibit distinct architectures that have huge influence on their mechanical properties: porosity can be as low as 5 % in cortical bone and 85 % in trabecular bone (in young people, [101]).

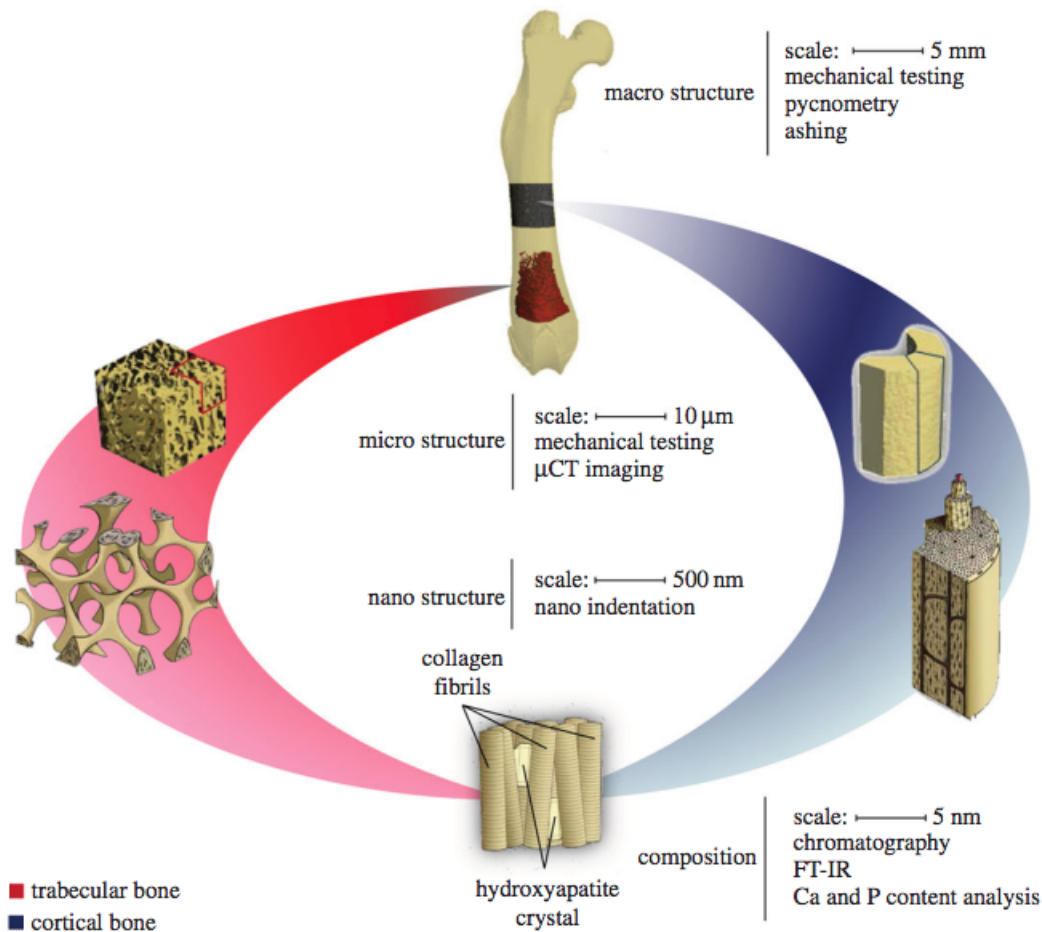


Figure 1.16: Illustration of the different constituents of trabecular and cortical bone, from macro- to nano-structure, as well as observations methods. Macro- and micro-structure can be assessed with common mechanical testing, whereas nano-structure requires nano-indentation and composition of this nano-structure can only be observed through chemical techniques such as chromatography or fourier-transform infrared spectroscopy [87].

Trabecular bone is the internal part of bone tissue and shows an open cell porous network. The functional unit of cancellous bone is called trabecula. Trabeculae arrangement is forming bone microstructure. The high surface area of trabecular bone (ten times the one of cortical bone [128]) makes it suitable for metabolic activities like such as the exchange of calcium.

Cortical bone is much denser and its basic unit is called osteon. As can be seen in Figure 1.17, each osteon is composed of concentric layers of compact bone called lamellae. Those layers surround the Haversian canals, which provides blood to the bone. Cortical bone is also metabolically active.

Regarding mechanical properties, cortical bone is stiffer in longitudinal direction (longitudinal modulus of around 18 [GPa] for human bone), and shows transverse isotropy (transverse modulus of around 10 [GPa] for human bone). This anisotropy is probably partly due to the highly anisotropic structure of the constitutive collagen fibrils arranged in the concentric lamellae [35].

The outer surface of cortical bone is called periosteum and inner surface, delineating cortical and trabecular bone, is called endosteum. Mechanical properties of trabecular bone are strongly dependent on apparent density and architecture and may therefore vary from one location of the skeleton to the other.

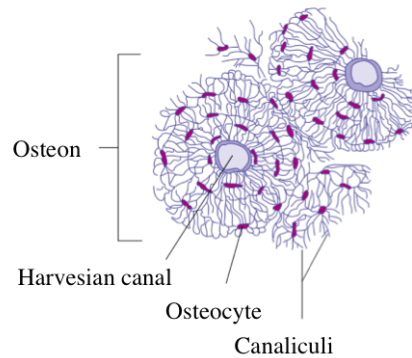


Figure 1.17: Illustration of the structure of an osteon (adapted from [129]).

1.3.2 Subchondral bone

Subchondral bone is a type of bone tissue that refers to bone that lies immediately below cartilage. The main role of subchondral bone is to maintain the integrity of the overlying articular cartilage and provide support [75].

Although papers dealing with morphology of subchondral bone give different meanings to the adjective "subchondral", it is admitted that from the tidemark, the calcified cartilage extends for a varying distance toward the marrow cavity, where it is remodeled and replaced by bone. As shown in Figure 1.18, subchondral bone can be separated into two main parts: the subchondral bone plate, a thin cortical lamella lying beneath the cartilage, and subchondral trabecular bone [44].

Subchondral bone has also a particular mechanical behavior. Indeed, it is known that articular cartilage deforms much more than underlying bone, therefore protecting the bone. However, in the event of specific loadings such as rapid dynamic activities, the ability of cartilage to absorb the impact drops and the subchondral bone has to act as the primary shock absorber [75]. Subchondral bone may also be important for cartilage nutrient supply and metabolism [21].

Moreover, subchondral bone plays a crucial role in the initiation and progression of osteoarthritis (OA) [21]. However, there is still a controversy about its contribution to the pathogenesis of the OA. Indeed, it is not clear whether it is the trigger or the consequence of cartilage degeneration [67].

Subchondral bone and its link with cartilage has been dominantly studied in the knee [136, 74] or hip [20] joints. However, it will be of major importance for our study as well because, as we have seen, insertion of ligaments and tendons into bone are involving a fibrocartilaginous region.

1.3.3 Bone development

Notions about bone development are also interesting to understand because even adult bone is exhibiting features originating from that growth.

Most bones, therefore called endochondral bones, are formed by endochondral ossification. This type of ossification means that hyaline cartilage is progressively replaced by bone. The process is illustrated in Figure 1.19. Briefly, the first step consists in the infiltration of cartilage with blood vessels and osteoblasts that start to transform the cartilage into a periosteum (of compact bone thus), while the center of the diaphysis (central part of a long bone) is disintegrating and progressively replaced with spongy bone. This is the first center of ossification. The second ones are located in the epiphyses (end parts) of the bone. They are

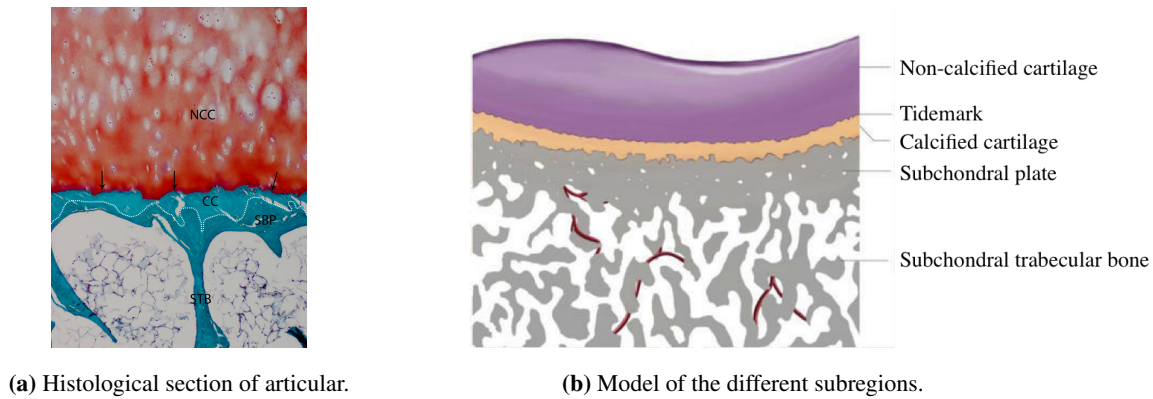


Figure 1.18: Structure of articular cartilage and subchondral bone in a normal human joint [67].

formed later than the first one. At the end of ossification, only two areas still contain cartilage: over the surface of the epiphysis and between the epiphysis and diaphysis. The latest is called growth plate or growth region. Even when ossification is complete, bone keeps on growing. The process is then similar to endochondral ossification: cartilage grows and osteoblasts follow to ossify cartilage. Bone growth is considered to stop in the adolescence (early twenties).

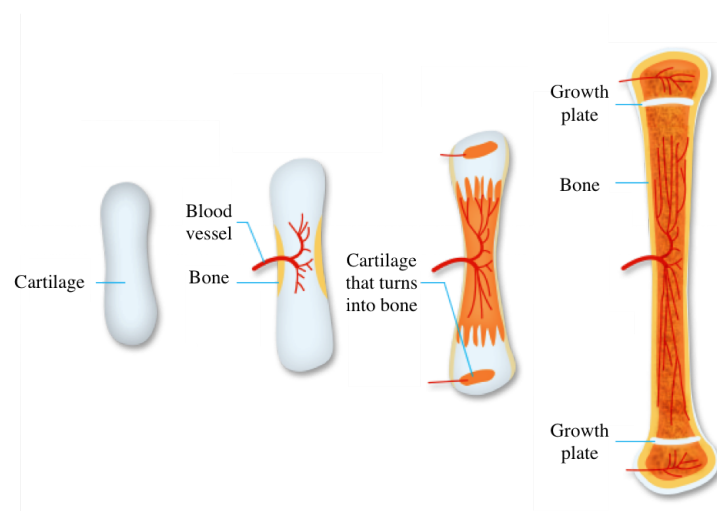


Figure 1.19: Simplified illustration of bone growth process from early fetus until adolescence (adapted from [46]).

1.3.4 Bone remodeling and adaptation

Bone is not only characterized by its hierarchical structure up to nanoscale: it is a truly living cellular network, allowing a continuous renewal process to repair damages. But not only bones repair themselves, they also can adapt their structure to mechanical load.

This is all done thanks to cells that live within bone. As shown in Figure 1.20, four types of cells coexist, namely osteocytes (typical bone cells), osteoblasts (bone forming cells), osteoclasts (bone resorbing cells) and bone lining cells (old osteoblasts that stay at the surface of the bone).

Bone remodelling is allowed thanks to mechanical stimuli that generate signals somehow received by those cells, probably the osteocytes [79]. The exact mechanism is still unknown. However, those external stimuli are effectively translated into bone formation or resorption. For example, as we know, one of the primary functions of bone is to support the body. It has actually been proven that bone tissue was adapting to mechanical stresses generated by the physical activity of a specific individual, enabling

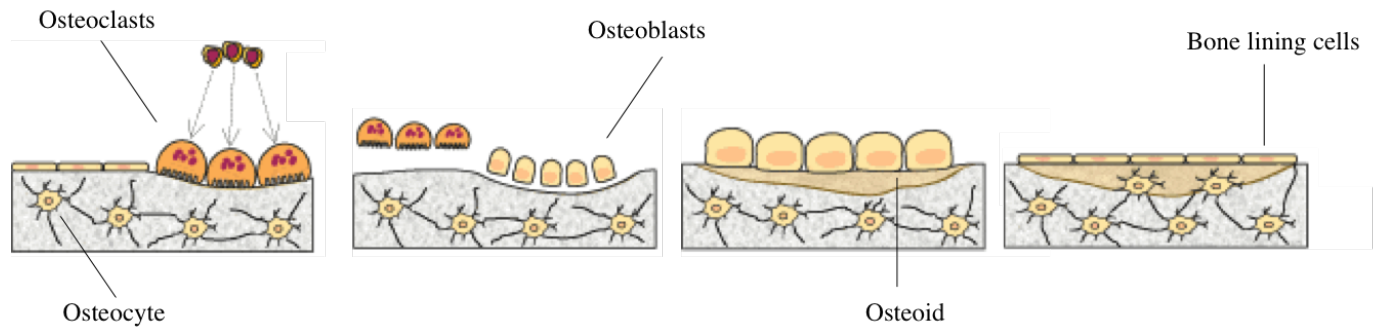


Figure 1.20: Illustration of the bone cells and remodelling process (adapted from [56]).

bone structure to bear the load of the body as efficiently as possible. Specifically, an increase in the mechanical loading would lead to an increase of bone mass, while a reduction of it would cause bone removal [32].

However, bone is also able to provide an even finer adaptation in order to translate the mechanical "signals" into appropriate changes in bone architecture. This has been first assumed by Roux and Wolff more than 100 years ago [132], [100]. Wolff believed that bone architecture was determined by mathematical laws: the thickness and number (i.e. distribution of mass) of trabeculae would correspond to the quantitative distribution of mechanical stress, and the trabeculae must be stressed axially in compression or tension. The assumption was based on the correspondence between stress trajectories and trabecular architecture in the proximal femur [132], [117]. This is illustrated in Figure 1.21. Later, it has been shown that trabecular bone was even more finely replying to loading, with a thickening of the trabeculae in highly loaded regions and reduced anisotropy [102]. Bone remodeling is nowadays believed to be a stochastic process under some mechanical control.

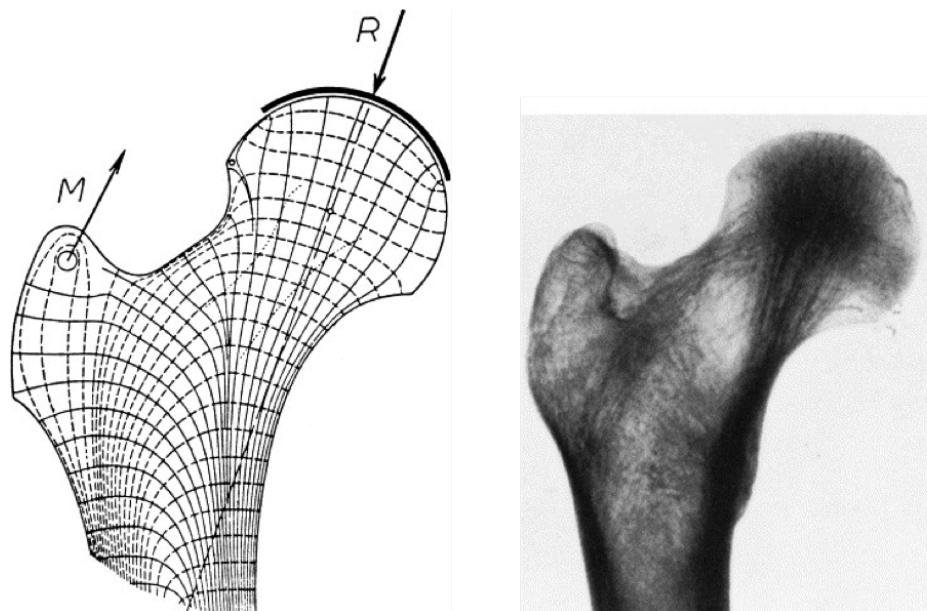


Figure 1.21: Illustration of the Wolff's law in the proximal femur: there is an obvious correspondence between stress trajectories and trabecular architecture [117].

1.4 Main aims of the master thesis

So far, research has been focused on the understanding of the structure and function of the enthesis in itself, as well as on the mechanisms allowing its efficiency. A lot of effort is also provided in understanding tendons behavior, whether it is from a material point of view or regarding pathologies [106, 105, 7]. But, finally, little attention has been paid to the bone beneath the enthesis. A few observations have been made but no quantitative study has been focused on whether bone was effectively adapting to accommodate the loading coming from the tendon. Therefore, this is the question we have decided to address: does calcaneus show structural and mechanical adaptation to the insertion of Achilles tendon ?

To address that question, we investigate adaptation at different length scales by analyzing various aspects of bone morphology. At the microscale, we assume surface roughness to be higher at the insertion site compared to other locations at the surface of the bone. At a higher length scale, we assume the presence of a gradient in porosity when progressing from the bone surface towards the porous trabecular interior. Finally, at the length scale of trabeculae, we make the hypothesis of a local change in the orientation of trabecular architecture. This last adaptation is supposed to favor load transmission. Indeed, it has already been proposed that trabeculae beneath insertion were oriented along the long axis of the Achilles tendon, and that this could possibly suggest a "line-of-force" transmission from Achilles tendon to the plantar fascia [67, 11].

As a second step, we exploit image-based high resolution micro-structural finite element analysis in order to demonstrate that structural adaptation at the insertion locations are reflected into biomechanical advantages.

Chapter 2

Experimental part

2.1 Introduction

This chapter aims at describing the experimental part of the project. In order to either quantify tissue structure in the region of interest or build a realistic finite element (FE) model, an assessment method or imaging technique has to be chosen. Because it is nondestructive and noninvasive, micro computed tomography (μ CT) has been selected. Indeed, this method has been shown to provide accurate results when compared to, for example, conventional static histology analysis, both in humans [66, 83, 36, 3, 22] and animals [103, 15, 120, 4, 9]. These studies show that morphological measurements obtained with μ CT have a high correlation coefficient with outputs from histology analyses. Moreover, μ CT allows to analyze a significantly larger volume of interest in a reduced amount of time. Furthermore, μ CT has been proved to be accurate in evaluating surface roughness of additive manufactured porous materials [63], and roughness assessment is an important point of our study. Finally, FE based on high resolution μ CT imaging systems has enabled to generate models with fine details allowing to determine stresses and strains at resolutions that were not previously possible using continuum FE based on clinical CT scanners [17].

In conclusion, the method we follow here has been widely accepted as an accurate and "gold standard" way to assess bone morphology and structural mechanics.

Regarding experimental data that has been acquired, we have chosen to focus our attention on calcaneus structure. Indeed, the purpose of this project is to investigate the structure of the bone around the insertion site, therefore high resolution data from this region is required.

The purpose of this chapter is to describe, first, samples collection and preparation. Then, details of the image acquisition procedure are given. We finish with a short critical discussion about the followed methodology.

2.2 Sample preparation

Because μ CT does not require any cutting through the sample, there is no need to decalcify the bone. On the opposite, histological analyses require a lengthy step of demineralization in order to be able to actually cut the sample. This implies, in addition to the extraction, fixation, dehydration and embedding, a decalcification step. This can be done by immersing the samples in a decalcifying agent (such as formic acid) for a long period (up to three weeks) and even with such a long period the cutting of the paraffine embedding can be delicate.

Nevertheless, even for μ CT, the sample preparation step is of major importance. Any improper manipulation can lead to artifacts in the reconstructed images.

2.2.1 Extraction

First, the legs have been extracted from two frozen rats. Animals were available at the university hospital of Liege (CHU) to be used in another study for which ethical approval had already been received.

More precisely, the extraction was done following the gastrocnemius muscle, as can be seen in Figure 2.1, down to the ankle and then cutting the foot. After that, the Achilles tendon has to be located. This step has to be carefully conducted in order to extract the proper tendon. Indeed, confusion may occur because of the soft tissue surrounding the region.

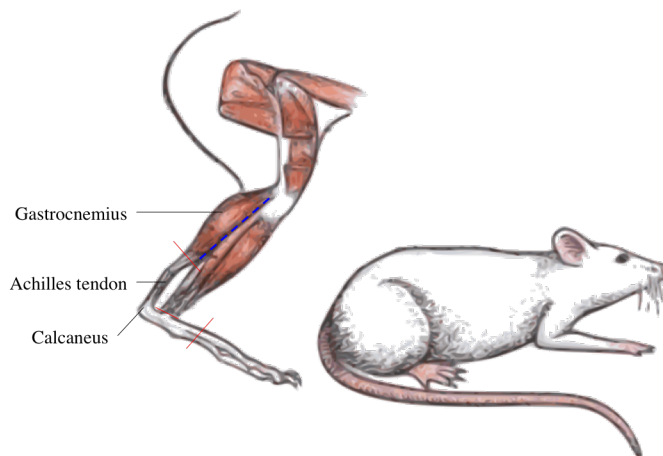


Figure 2.1: Anatomical details for the extraction phase [10]:

- - - preliminary cutting line and — final cuts.

2.2.2 Fixation

Once the extracted specimens have reached satisfying apparent quality (removal of undesired soft tissues), they have been placed in a bath of 70% ethanol for 24h at room temperature. This step is called fixation. The aim is to preserve the biological tissue and avoid its degradation. As suggested by the name, the goal of the fixation process is to terminate all the ongoing biochemical reactions. The choice of the fixative depends on the specimen under study and the objective of the analysis: in our case, we have chosen chemical fixation with alcohol. Indeed, ethanol is a common choice for fixing frozen samples [125].

2.2.3 Dehydration

The next step consists in dehydrating the specimen. Indeed, water needs to be removed from the tissue to insure a proper infiltration of the embedding resin, which is hydrophobic.

Therefore, the tissue has been immersed in baths of ethanol with increasing concentration (70, 80, 90 and finally 100%, water free), at room temperature. It is preferable to increase gradually the amount of alcohol to avoid any excessive distortion of the tissue.

2.2.4 Embedding and cutting

Once the specimens are completely dehydrated, they must be embedded in a resin that creates a kind of 'cocoon' around it. This ensures that the positioning of the specimen in the scanner remains stable, as well as to prevent movement and artifacts.

First, specimens are placed in cylindrical molds as shown in the first picture in Figure 2.2. Those ones have to be clean and dry before encapsulating. For the embedding itself, two products from Buehler company were used: EpoThin 2 Hardener and EpoThin 2 Resin. Epothin 2 is a clear, very low viscosity epoxy system. Epoxy resin alone has poor properties. However, reaction of epoxy resin and hardener allow to reach mechanical properties required for a correct embedding. This process is called curing or gelation [124]. In our case, we used a double syringe (see picture in Figure 2.2) in order to carefully collect 5 [mL] of hardener and 10 [mL] of resin for each sample. Then they have to be mixed for two minutes with a stirring stick using slow and controlled motion until mixture is blended. Afterwards, mixture is poured into the cylinder and specimens have to be let for rest overnight (for 9 hours) at room temperature in order to allow the epoxy to cure. Then the mold can be removed (see last picture of Figure 2.2).

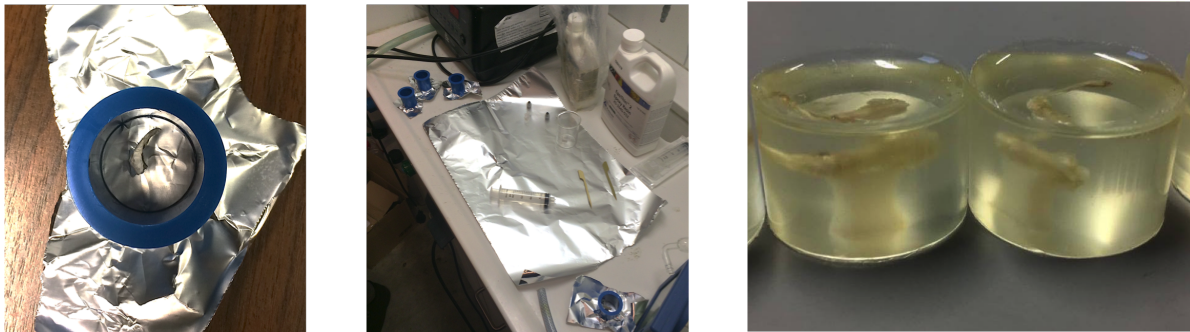


Figure 2.2: Illustration of the embedding process.

From left to right: cylindrical mold, workbench and resulting embedded samples.

The final step before scanning consists in cutting the samples so that they get as small as possible for a higher resolution. This step has been done with a simple manual saw. Final samples are shown in Figure 2.3 .

2.3 Image acquisition

In this section, details about the scanning process are given. The scanner used is presented, as well as its specific working parameters. Then we go through the key parameters of the images acquired with the scanner.

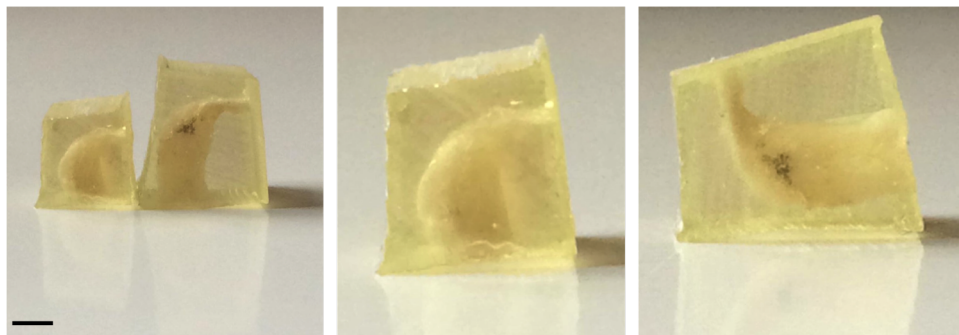


Figure 2.3: Final samples after the cutting phase. Specimen 1 is the biggest one (on the right and then on the third picture). Scale bar: 2.5 [mm] (approximately).

2.3.1 Scanner

For this study, we used a particular scanner from Bruker company called SkyScan-1272, shown in Figure 2.4. This scanner can be used for 2D/3D image analysis, surface and volume rendering.

As a reminder, μ CT scanners are based on X-ray attenuation measurements taken from different angles to produce cross-sectional images of a scanned object without cutting it, which makes the procedure nondestructive. Basic components of a μ CT scanner are the x-ray tube, the collimator and some filters, the sample holder and the detector. The x-ray tube emits x-rays that are collimated and filtered, then attenuated through the sample and collected by the detector. This is represented in Figure 2.5. Each projection is used to reconstruct the full object. Therefore, for the study to be reproducible, several key parameters should be stated. First, parameters of the x-ray tube should be described, including the tube potential, which is the peak electric potential originally applied on the electrons to produce the photons, and the x-ray intensity, which is the current in the x-ray tube. SkyScan-1272 x-rays are characterized by an energy in the range of 20 to 100 [kV], which is typical for μ CT systems [16]. Source current will be given when considering the specific samples. Moreover, voxel size, integration time and frame averaging should be specified as well.

Complete technical details about the scanner may be found in Appendix A.

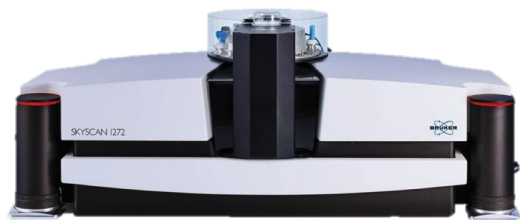


Figure 2.4: Picture of the SkyScan-1272 from Bruker company [19].

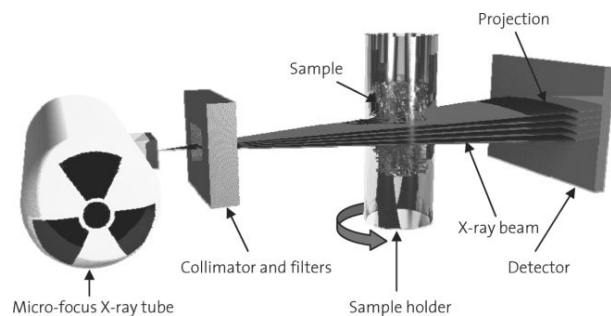


Figure 2.5: Key components for a standard μ CT scanner [16].

2.3.2 Parameters of the acquisition

Specimens were always positioned at the same distance from the source. Precise values may be found in Tables 2.1 and 2.2. Other key parameters are the x-ray tube potential and intensity. Those were kept constant for both specimens as well, with 80 [kV] of source voltage and 124 [μ A] of source current. However, the two specimens had different sizes because of the manual embedding and cutting process. Therefore, this has led to distinct image resolutions. As we will see later, the impact of this parameter is considerable for the quality of the images.

► Specimen 1

The first sample is the largest in size. Output images exhibit a voxel size of 5 [μ m]. It has been exposed to x-rays during 1700 [ms]. Frame averaging option was activated with 4 repeated measurements for each projection. Reconstruction lasted 0.06 [s] per slice. Final stack of scans consists of 1059 slices in the $x - y$ plane, each of 2016 voxels side. For easier forward manipulation, those images were compressed, which leads to a sequence of 797 slices of 1024 voxels side. All key parameters of the acquisition may be found in Table 2.1. The complete range of parameters characterizing the μ CT may be found in Appendix B.

ACQUISITION		RECONSTRUCTION	
<i>Parameter</i>	<i>Value</i>	<i>Parameter</i>	<i>Value</i>
Camera to Source [mm]	221.88	Reconstruction duration per slice [s]	0.062323
Object to Source [mm]	61.63	Total reconstruction time (1059 slices) [s]	66
Source Voltage [kV]	80	Sections Count [slices]	1059
Source Current [μ A]	124	Result Image Width [voxels]	2016
Image voxel Size [μ m]	5	Result Image Height [voxels]	2016
Depth [bits]	16		
Exposure [ms]	1700		
Frame Averaging [-]	ON (4)		

Table 2.1: Key parameters of the μ CT scan acquisition for specimen 1.

► Specimen 2

The second specimen was embedded in a smaller matrix, leading to a voxel size of 2.5 [μ m]. Exposure duration was 3000 [ms], with 4 repeated measurements per projection. Reconstruction duration was also increased with 0.26 [s] per slice. The resulting 2470 slices of 4032 voxels side were again compressed in order to end up with 1741 slices in the $x - y$ plane of 2048 voxels side each. Key parameters of the acquisition may be found in Table 2.2 , and the complete range of parameters characterizing the μ CT may also be found in Appendix B.

2.4 Discussion

More attention could have been paid to the animal status prior to extraction. Indeed, because we had to work with specimen from another study, little information was available about gender, age and health. As we know that aging may affect bone structure, this is a point we should keep in mind when discussing our results.

Acquisition		Reconstruction	
<i>Parameter</i>	<i>Value</i>	<i>Parameter</i>	<i>Value</i>
Camera to Source [mm]	221.88	Reconstruction duration per slice [s]	0.257490
Object to Source [mm]	61.63	Total reconstruction time (2470 slices) [s]	636
Source Voltage [kV]	80	Sections Count [slices]	2470
Source Current [μ A]	124	Result Image Width [voxels]	4032
Image voxel Size [μ m]	2.5	Result Image Height [voxels]	4032
Depth [bits]	16		
Exposure [ms]	3000		
Frame Averaging [-]	ON (4)		

Table 2.2: Key parameters of the μ CT scan acquisition for specimen 2.

Chapter 3

Structural analysis

3.1 Introduction

This first part of the project focuses on the analysis of structural aspects of bone beneath the insertion of the Achilles tendon. Our study consider three specific features: bone porosity, its anisotropy and the roughness at the surface. The aim is to demonstrate that, at the insertion of the tendon, bone shows interesting adaptation abilities at different length scales. Porosity and orientation have been chosen because of their relevancy in the study of bone. Roughness has been barely considered in the context of bone surface evaluation. The lack of literature or references has lead us to the development of a new approach to characterize it.

The subsequent qualitative analysis has been conducted with ImageJ, CTAn and CTvol¹, whereas Matlab has been the reference software for quantitative characterization of bone morphology.

This chapter begins with a preliminary presentation of the images obtained with the μ CT. Then, the procedure followed in order to investigate the mentioned parameters is described. Afterwards, the results of this investigation are presented, along with a discussion calling for a critical consideration of those results. We conclude with presenting how our findings about bone structure may improve our understanding of Achilles insertion into calcaneus.

3.2 Preliminary analyses

The aim of this section is to present an overview of the images obtained with μ CT. A first insight of the scans obtained are shown in Figures 3.1 and 3.2. Slices from each plane at approximately middle depth (in each direction) are represented, along with the full reconstructed volume. Notice that when comparing Figures 3.1 and 3.2, the difference in resolution between both samples can already been observed.

In this section, we start with explaining the reasoning that we have followed to deduce where the Achilles tendon is inserting. Then, we note additional observations about bone morphology.

3.2.1 Deduction of the insertion site

Deduction of the insertion site is delicate as our experimental procedure has not included any staining of the tendon. However, soft tissues are generating noise in the images, which can already be helpful. In addition to that, observation of the freshly extracted samples and knowledge from the literature has allowed us to deduce where tendon was entering the bone.

First of all, spectrum LUT visualization of ImageJ allows us to see quite clearly the noise generated by the insertion of the soft tissue. 3D reconstruction and an example of a $y - z$ slice are shown in Figures 3.3 and 3.4. The global shape of the bone exhibits a valley in the $x - y$ plane, approximately at middle depth, where the tendon seems to insert.

Therefore, based on pictures such as the one shown in Figure 3.5, as well as histological cuts such as the one presented pre-

¹Both of those softwares belong to BRUKER company, advised for image visualization when using Skyscan scanners.

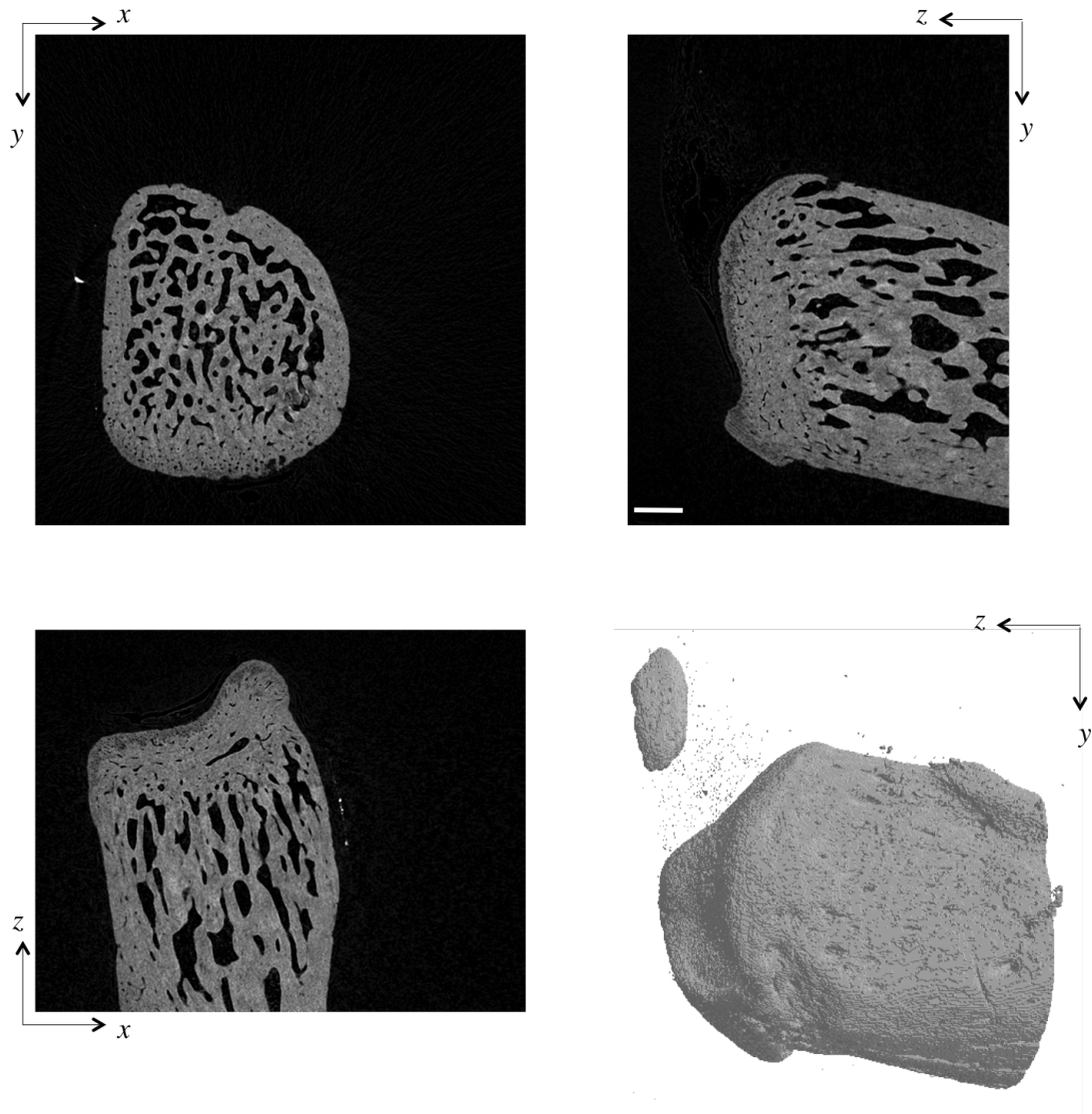


Figure 3.1: Examples of slices obtained in the three planes for specimen 1, visualized in ImageJ with the Volume viewer tool. Bottom left: 3D reconstruction of the sample based on the scans. Volume visualized in CTVol and created with CTAn (after resizing the scans of 50%). Notice the presence of a bony artifact or debris in the upper left corner. Scale bar: 500 [μm]

viously in Figures 1.15a and 1.15b, we have deduced that the position of insertion was on the bottom posterior position of the calcaneus, approximately at half depth with respect to sagittal plane. This is an assumption, and a staining of the tendon for the scans would have allowed us to be more accurate in this deduction.

3.2.2 Qualitative observations

Our analysis deals with $y - z$ plane slices, meaning slices in the sagittal plane. Therefore we focus our additional observations on two representative slices on that plane, for each specimen: those are our reference slices along this project. They are shown in Figures 3.6a and 3.6b. Notice that both specimens have been cut and rotated so that upper surface of the bone is aligned with horizontal plane, which seems to be the most natural position of the bone (at least at rest). However, orientation of the bone obviously varies during physiological activities: this rotation is applied in order to ensure fair comparison between samples. First of all, one can notice that porosity of specimen 2 is bigger than the one of specimen 1. Specific values are computed in next section. However, loss of bone with aging is of common knowledge so it could be that the specimen 2 is simply older.

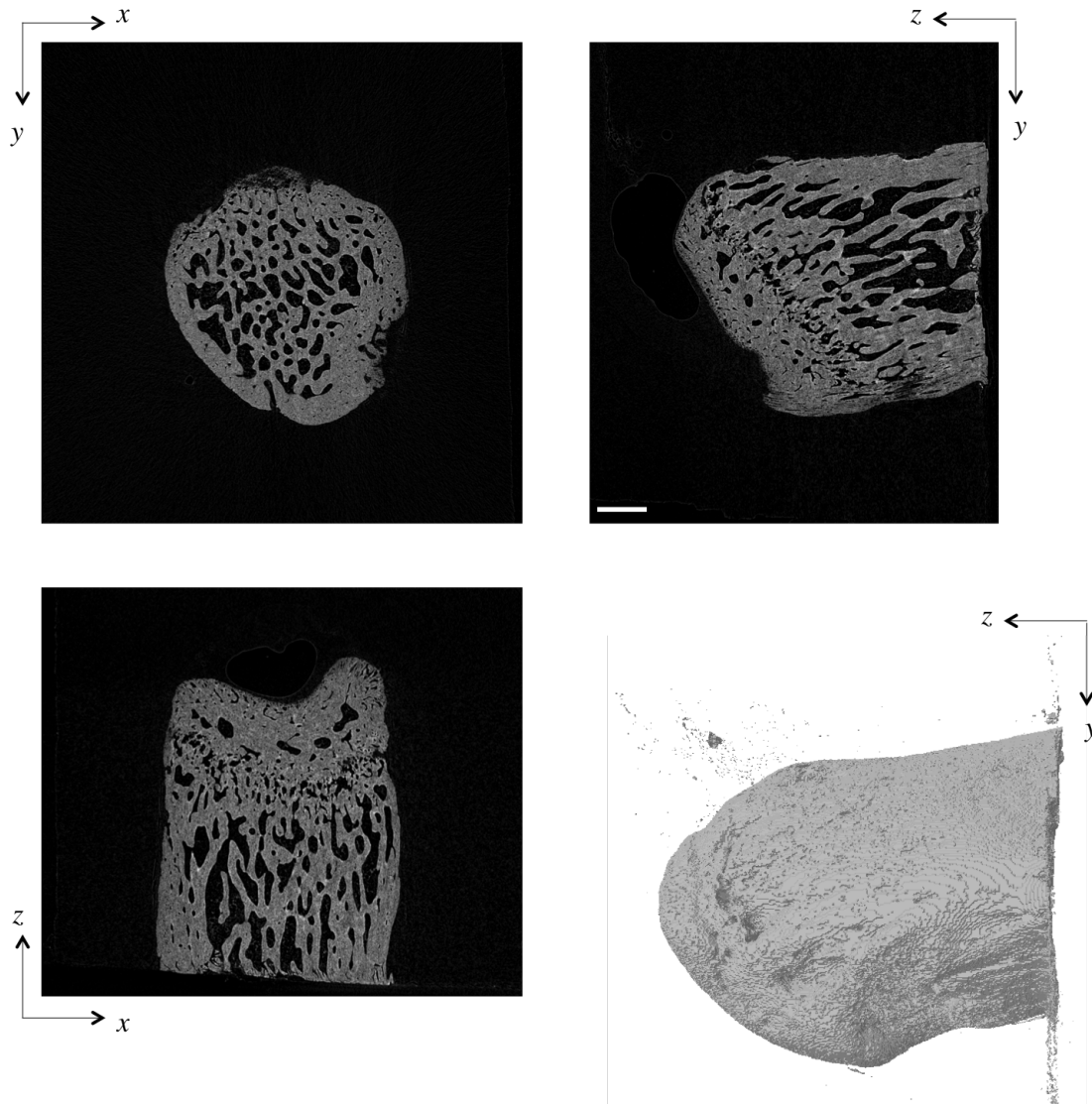


Figure 3.2: Examples of slices obtained in the three planes for specimen 2, visualized in `ImageJ` with the `Volume viewer` tool
 Bottom left: 3D reconstruction of the sample based on the scans. Volume visualized in `CTVol` and created with `CTAn` (after resizing the scans of 25%). Scale bar: 500 [μm]

Secondly, we can comment on the general structure of the bone. We start with specimen 2, the one that has the highest resolution (Figure 3.6b). At the insertion (red circle), interdigitations of the bone can clearly be observed, as well as presumably mineralized fibrocartilage. Beneath the insertion, the oriented "trabecular" structure can also be spotted. Additionally, the orange circle shows what is likely to be the growth plate. Therefore, majority of the bone we are looking at is subchondral bone, which is why segmentation of trabecular and cortical bone would be delicate in our case. Next, it is probable that we are able to spot blood canals as well as osteocytes. Sizes of those components are obviously smaller in rats than humans, but this is investigated in details when computing bone anisotropy (Section 1.3.3). Going now to specimen 1, one can notice that interdigitations are less clearly noticeable. This is probably due to the low signal to noise ratio in comparison with specimen 2. Growth plate is also less easy to spot. However, a supplementary feature can be noted: it is indeed quite likely that the observed tuberosity at the bottom (circled in blue) of the bone is the plantar fascia ligament insertion. This would also corroborate the assumption that trabeculae are oriented from one insertion (the one of the calcaneal tendon) to the other (the one of plantar fascia). However, this insertion cannot be identified as readily in specimen 2. Still, it could be that the blue circled region exhibit very fine trabeculae because

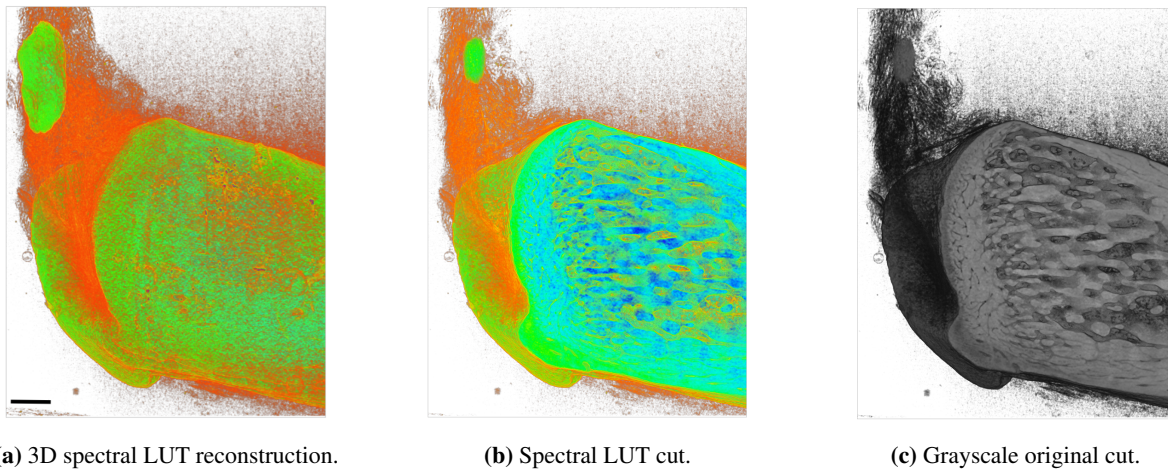


Figure 3.3: 3D spectral LUT volume and cuts in the y - z plane (LUT and Grayscale) of specimen 1, showing the noise generated by the surrounding soft tissue and indicating the position of insertion at mid-depth along the x -axis. All the images have been generated with ImageJ. Scale bar: 500 [μm]

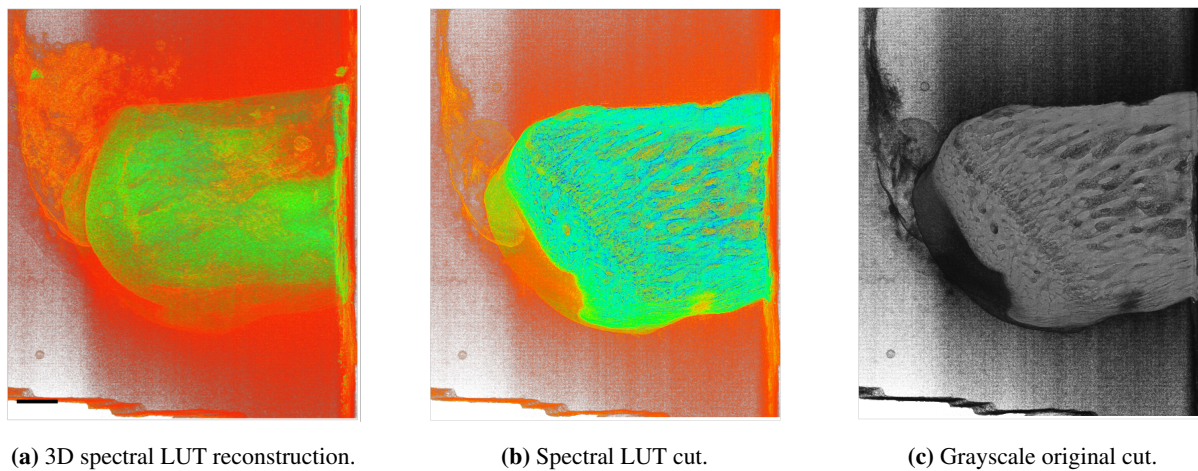


Figure 3.4: 3D spectral LUT volume and cuts in the y - z plane (LUT and Grayscale) of specimen 2. Noise is again visible (and even stronger). Notice the presence of an artifact in LUT images, that could be an air bubble. Also note the presence of a hole at the bottom right, it will be discussed later. All the images have been generated with ImageJ. Scale bar: 500 [μm]

of a close insertion site. In order to further investigate this possibility, other slices are explored (deeper in the x -axis direction). Figure 3.6c shows a slice in which plantar fascia location is more likely to be accurate. In addition, it turns out that this region is indeed the origin of the one circled in our reference slice (see more pictures in Appendix C).

3.3 Methods

Before getting into the details of the method followed for each aspect of the analysis, we start this section by describing our general procedure.

Indeed, as it has been described in Chapter 2, μCT data provide access to $x - y$ plane slices covering the whole sample and resulting in a reconstructed volume. Therefore, one could study volumetric variation of bone features based on such data. However, we have chosen to focus on 2D analysis. As it will be discussed in Chapter 5, an extension of the present work is of course to

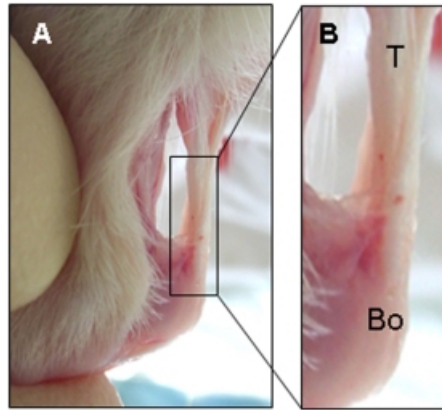


Figure 3.5: Picture showing a rat Achilles tendon insertion into bone [86].

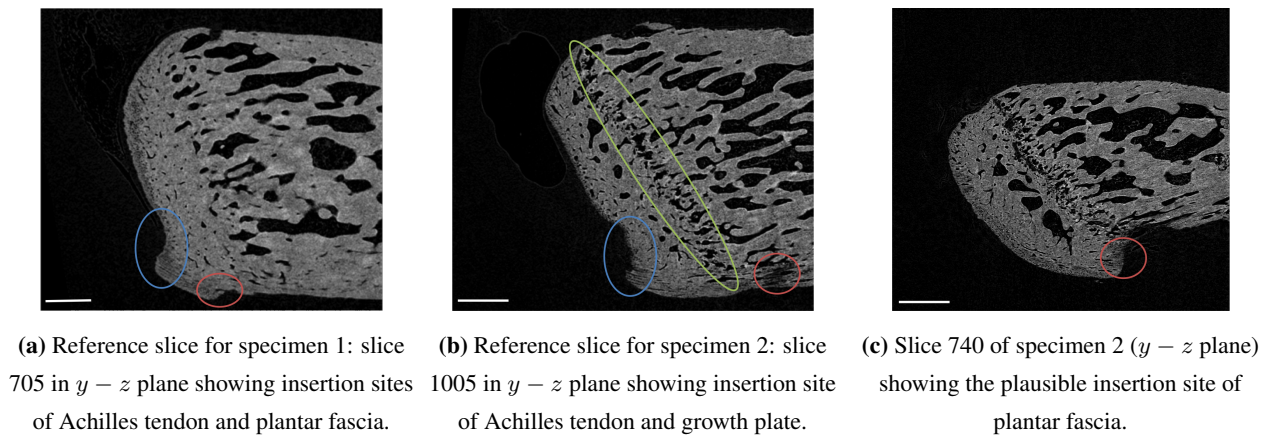


Figure 3.6: Noticeable features of $y - z$ plane slices for both specimens. Scale bar: 500 [μm].

Achilles tendon insertion site, Growth plate, Planter fascia insertion site.

adapt the following investigation towards 3D. However, the high resolution scans already enable us to catch interesting features and it has thus been decided to exploit, as first step, information available in 2D images. In order to insure consistency and avoid the observation of phenomena that could be slice-dependent, each analysis is conducted for a set of 10 $y - z$ slices through the bone. This set covers in both specimens a depth of 250 μm , when having 5 slices between each slice of interest in specimen 1 (resolution of 5 μm), and 10 in specimen 2 (resolution of 2.5 μm). The idea is illustrated in Figure 3.7 for specimen 1. The following subsections now describe the procedure applied for each of those slices individually, as well as the statistical testings conducted on the 10 slices in order to highlight significant behaviors.

3.3.1 Pre-processing

Before conducting any quantitative analysis of μCT images, it is of common practise to describe post-acquisition processing of the data. Those steps are of importance because they may affect the accuracy of the results. It is also critical to be accurate regarding the followed approaches in order to allow readers to interpret results and compare findings across different studies [16]. In our case, the processing of images contains three steps: filtration, thresholding and unconnected part removal. Papers investigating bone morphology sometimes segment cortical and trabecular bone. However, such a delineation is delicate in our case because the great majority of our region of interest consists in subchondral bone.

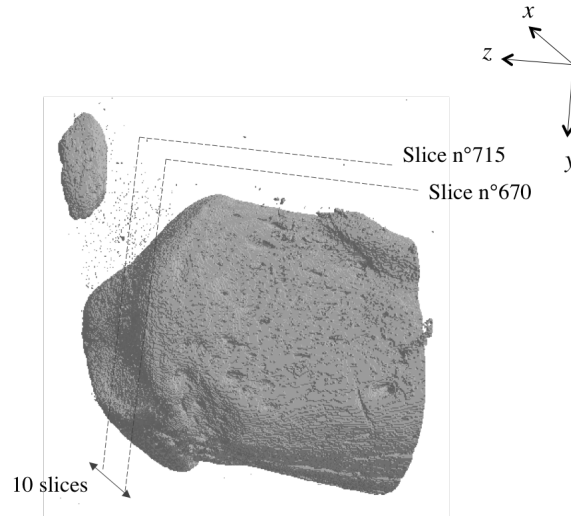


Figure 3.7: 3D volume based on μ CT images and illustration of the slices of interest for specimen 1.

► Filtration

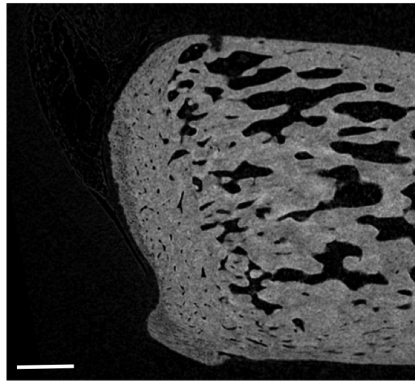
A filtration step is required because of the inherent signal noise coming along with any reconstructed μ CT data. The goal is, on one hand, to remove noise while, on the other hand, maintaining contrast between bone and marrow. Noise removal requires a low-pass filter (i.e. blurring) while high contrast involves high-pass filtering (i.e. edge enhancement). Balancing those conflicting goals is most commonly done using a Gaussian filter [16]. Because we want to keep as much bone architecture as possible, we apply a minimum amount of filtering. Therefore, we used the **Matlab** function `imgaussfilt` that uses a 2D Gaussian smoothing kernel with a standard deviation of 0.65 (0.5 to 2 is an acceptable range, [16]). The effect of Gaussian filtering is shown in Figure 3.8 .

► Thresholding

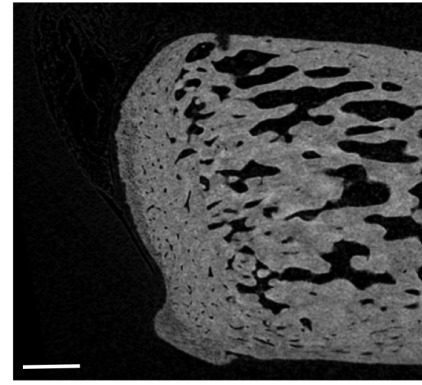
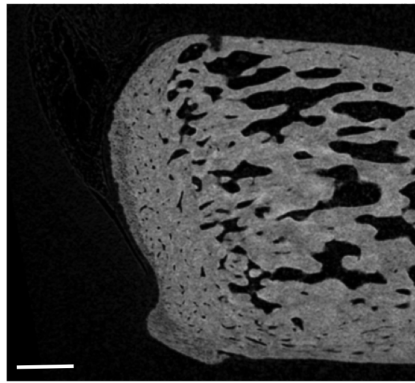
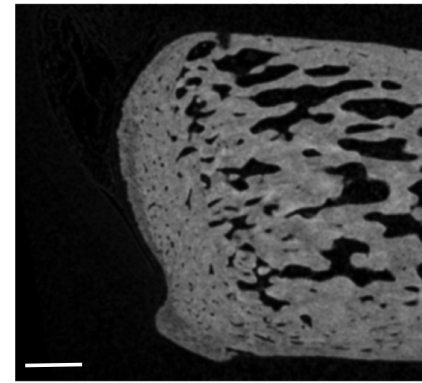
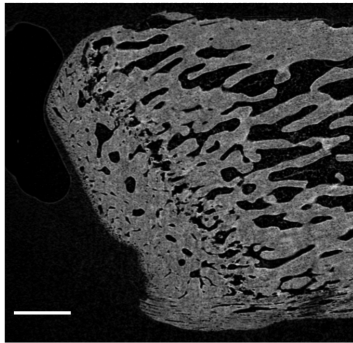
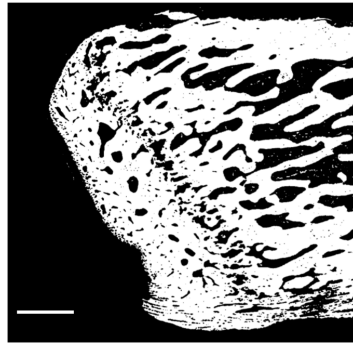
The second important step consists in thresholding. The aim is to segment the image into "bone" and "background" voxels. The function `graythresh` applied to images allows us to determine a global threshold that can further be used to convert our intensity image to a binary image with the function `im2bw`. The computed threshold is a percentage of the grayscale, which is then introduced into `im2bw`. The computed threshold for slice 1005 of specimen 2 is 24.31% and the result is a binary black and white image as shown in Figure 3.9b.

► Unconnected parts removal

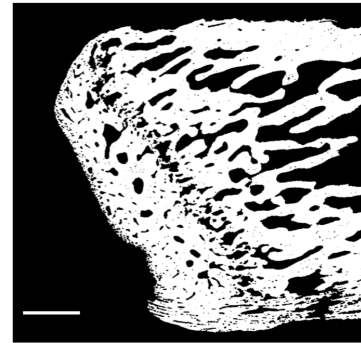
The last step of our pre-processing aims at getting rid of all the unconnected parts (mostly noise) that have been introduced in the images. The **Matlab** function `bwareafilt` extracts the biggest connected object of an image, enabling to remove all small parts. Illustration is shown in Figure 3.9c for slice 1005 of specimen 2. One can therefore see the drawback of it in that specific case: it is generating a hole at the bottom left of the image. However, the trabeculae in that region are so thin that in order to avoid this, it would require to lower the threshold down to a value that would introduce too much noise and unrealistic bone volume values. It has therefore been decided to not correct for this but keeping that issue in mind when drawing conclusions.



(a) Unfiltered initial image.

(b) Effect of a Gaussian filter with $\sigma = 0.65$.(c) Effect of a Gaussian filter with $\sigma = 1$.(d) Effect of a Gaussian filter with $\sigma = 2$.**Figure 3.8:** Effect of Gaussian filter on image clarity and contrast for slice n° 710 of specimen 1. Scale bar: 500 [μm].(a) Grayscale image with a Gaussian filter ($\sigma = 0.65$) applied.

(b) Black and white image obtained after thresholding.



(c) Resulting image after unconnected parts removal.

Figure 3.9: Illustration of all the pre-processing steps applied on the reference slice of specimen 2 (n° 1005). Scale bar: 500 [μm].

3.3.2 Porosity

Based on black and white images, porosity may easily be computed as one minus the area fraction, which is itself the number of "bone" voxels over an area of interest. The most delicate part regarding porosity is to be sure that the selected region of interest remains within the bone. Otherwise, inaccuracy would be introduced as this would artificially increase porosity. Therefore, we first explain the procedure followed for the delineation of the region of interest and then we go through the specific computations that were made in the context of porosity computation.

► Delineation of the regions of interest (ROIs)

As shown in Figures 3.11a and 3.11b, it has been chosen to define squared ROIs covering the surface of the bone and overlapping over half their length in both directions [121, 122]. Size of the ROIs have been chosen by trading off: the idea is to reduce noise of the calculated porosity (thus by increasing ROI size) while still allowing the evolution of bone architecture parameters to be represented. Moreover, one should keep in mind that it is advised that ROIs contain at least three to five intertrabecular length for the measurements to be accurate and representative [16]. After several trials, it has been decided to consider ROIs of $400\text{ }\mu\text{m}$ sides, resulting in 152 ROIs for specimen 1 and 96 for specimen 2. The difference originates from the size difference between the samples (specimen 1 is bigger).

► Parameters evaluation

Area fraction of each ROI is computed as the ratio of the "bone" voxel over the area of the ROI. Then porosity is simply obtained by subtracting this value to one. Each ROI is therefore characterized by a porosity, spatially assigned to the center of the square.

In order to characterize the variation of this parameter within the bone, a reference must be defined. For that purpose, two points have been defined: a first point considered as "insertion point" and another one regarded as "control point". Those points are represented in Figures 3.11a and 3.11b. While the first one is computed as the geometrical center of the manually defined insertion site¹, the second has been defined as the starting point of the first line of ROIs. Geometrical distance from those points to each ROI center is computed, as well as angle from insertion point. Angle measurement conventions are illustrated in Figure 3.10.

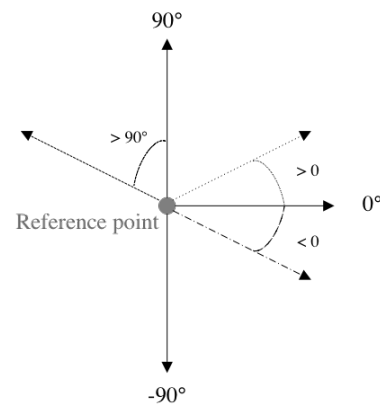


Figure 3.10: Illustration of the angle conventions considered for the porosity analysis. Reference point is either insertion or control point.

► Characterization of the outputs

The evolution of porosity with distance to insertion and control point will be plotted. In order to characterize it, the coefficient of determination, also known as R^2 , is measured in order to indicate how well one variable is replicated by the linear approximation of the other. Possible interpretation of this value will be given in Section 3.4.

Second, the evolution of porosity with horizontal distance (meaning along each line of the grid) is investigated. This evolution is characterized by the slope of the linear approximation and this value is confronted for two regions of the bone: the bottom and the top. Distinction between those regions is shown in Figure 3.11 (dashed lines). Finally, 3D evolution of porosity (meaning with distance and angle) will be studied for visualization purposes.

¹The delineation of the insertion region is based on observations detailed in Section 3.2.2 and is basically a rectangular version of the red circle shown in Figures 3.6a and 3.6b above.

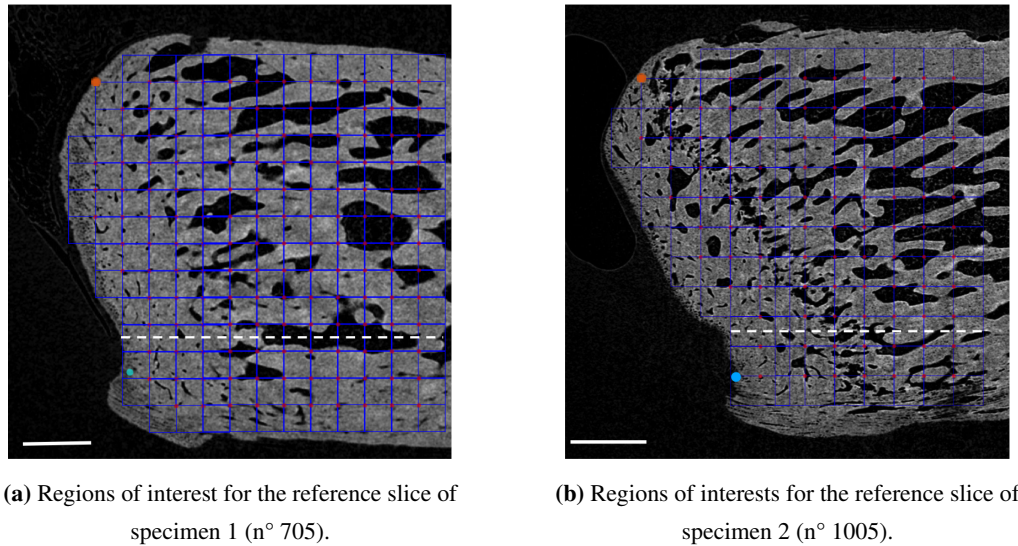


Figure 3.11: Illustration of the grid applied on both specimens for porosity evaluation.

●: Reference point when mentioning 'not insertion point' and ●: Reference point for insertion site
 Dashed line: separation between 'top' and 'bottom' regions. Scale bar: 500 [μm].

3.3.3 Orientation

The aim of this part of the structural analysis is to characterize bone anisotropy. Some authors have already qualitatively mentioned the orientation of the trabeculae beneath the insertion of the Achilles tendon [80, 11]. However, we develop in this subsection tools to quantitatively investigate microarchitecture orientation.

► Contour extraction

One first idea would be to exploit `Matlab` functions in order to compute orientation for each region of interest that has been defined hereabove. However, the issue with that method is that it leads to compensation mechanisms: indeed, a single ROI could include two pores oriented differently and therefore the mean of those orientations would just cancel the individual behavior of the holes.

The method developed consists in first extracting the contour of the bones, as well as its underlying holes and objects (with the function `bwboundaries`). This function implements Moore-Neighbor tracing algorithm modified by Jacob's stopping criteria [45]. It allows to extract the holes of any black and white image, as well as their size (defined as the number of boundary voxels). Holes are determined as regions containing zero value (black voxels), whereas objects will be surrounding non-zero value (white voxels). Holes and objects are illustrated for a specific slice in Figure 3.14a. In our case, identified holes corresponds well to real holes within the bone. This is therefore an indirect way of assessing trabeculae orientation. This method enables us to consider each pore and its orientation independently and then to sort them in ascending or descending order according to their size.

► Threshold evaluation

The following step consists in determining at which level we expect to notice bone orientation. Indeed, the high resolution scans allow us to observe microstructure of bone down to the scale of osteocytes and blood canals. Orientation of those small

holes may influence a lot the computed anisotropy while not being the result of any bone adaptation. Therefore, the aim is to determine a threshold on the size of the pores considered for our analysis that does not take small features into account.

Table 3.1 sums up values gathered in literature regarding osteocytes and blood canal diameters in bone of mouse and rat. Diameters may vary a lot from one study to another. Besides, no reference has been found regarding specific values for calcaneus bone. However, given the fact that the latest is a smaller bone than femur or tibia, it is consistent to assume that canals have a reduced size as well. Osteocytes being bone cells, they should keep the same size. Considering all of that, a threshold of $d = 10 \text{ } [\mu\text{m}]$ in diameter has been selected. In other words, only the holes exhibiting a perimeter of more than πd (rounded to $35 \text{ } [\mu\text{m}]$) will be studied for demonstrating bone mechanobiological adaptation.

Type of bone	OSTEOCYTE LACUNAE DIAMETER $[\mu\text{m}]$	BLOOD CANAL DIAMETER $[\mu\text{m}]$
Rat tibia [90]	$8.9 \pm 1.56 (**)$	15 ± 5
Rat tibia (metaphysis) [25]	$2.6 \pm 0.5 (*)$	$5.7 \pm 0.9 (*)$
Rat tibia [18]	/	15
Mouse fibula ² [50]	/	9.1

Table 3.1: Summary of values found in literature regarding osteocyte lacunae and blood canal diameters in rat and mouse.

Asterix indicates that mean and standard deviation have been computed with ImageJ based on images provided in the papers.

(*) source image may be found in Appendix D.

(**) has been computed based on image (a) of Figure 3.27.

► Orientation computation

In order to characterize the orientation of the holes, another function from Matlab image processing toolbox is exploited, called `regionprops`.

This function allows the measurement of various properties such as centroid or orientation. Orientation is computed by means of fitting to the region of interest an ellipse that has the same second area moments as the region. Afterwards, the angle between the horizontal axis and the major axis of the ellipse is returned. Figure 3.12 illustrates how the ellipse and its principal axis are fitted to the region under study. Output value is ranging from -90 to 90 degrees.



Figure 3.12: Illustration of the axes and orientation of the ellipse used to deduce orientation of a given region of interest [77].

This function is therefore applied to each hole of the bone. Figure 3.13 illustrates this procedure for three randomly chosen holes.

► Characterization of the outputs

Each hole is associated with an orientation, as well as a centroid, which is simply the center of mass of the region of inter-

²The fibula is a leg bone located on the lateral side of the tibia.

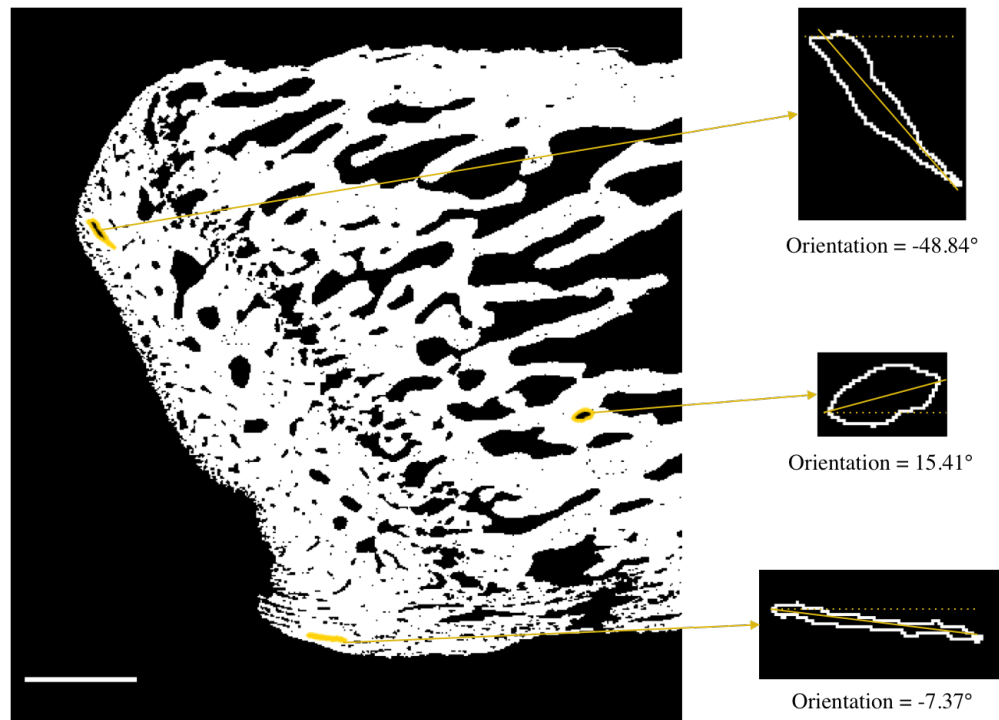


Figure 3.13: Illustration of orientation assessment for three (arbitrarily chosen) holes of the bone. Scale bar: 500 [μm].

est (computed with `regionprops` as well), as can be seen in Figure 3.14b.

In order to highlight interesting behaviors, the evolution of orientation is characterized for two distinct regions called "top" and "bottom". Bottom region contains the insertion site. Holes belonging to each region are coded with a different color in Figure 3.14c.

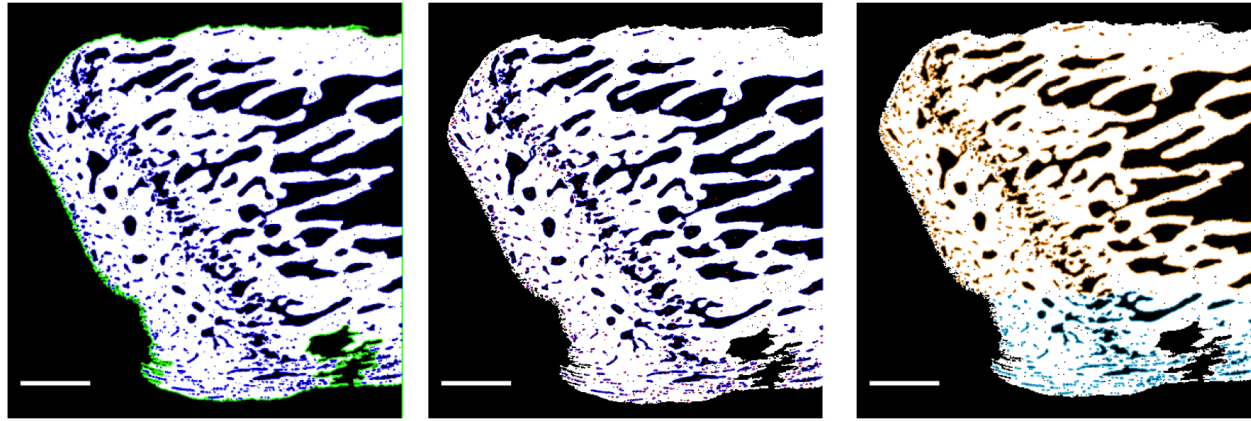
Finally, each region is described by the scattering of its holes orientation. The scattering itself is measured by means of the standard deviation of the set of angles. This measurement is assumed to represent the anisotropy of the zone, and both values will be statistically confronted to investigate adaptation within insertion area.

In order to check that the threshold level is indeed the one under which no mechanobiological adaptation can be found anymore, this analysis will be conducted for the holes of size below the threshold as well. The aim is to check whether the two regions exhibit a significant difference in the dispersion of the holes' orientation.

3.3.4 Roughness

The last parameter under study in our structural analysis is the roughness of bone surface. Because assessment of surface properties requires a high level of details, down to the micro-scale, this investigation will be conducted exclusively on our highest resolution scans, meaning specimen 2.

While the assessment of rugosity is well defined for metals or manufactured materials [96, 63], little attention has been brought to the definition of a procedure to characterize bone roughness. In this subsection, we go through the steps of the method adopted for such a study.



(a) Illustration of the distinct definitions of 'holes' and 'objects' obtained with `bwboundaries`. (b) Delineation of holes having a size bigger than the threshold and their centroids. (c) Demarcation of holes belonging to the top and bottom (aligned with insertion) region.

Figure 3.14: Illustration of the image processing steps for orientation analysis (on the reference slice of specimen 2). Scale bar: 500 [μm]

► Roughness parameters

In a roughness measurement protocol, it is of common practise to compute the following main parameters [63]:

- The arithmetic mean absolute deviation of the roughness profile:

$$P_a = \frac{1}{n} \sum_{i=1}^n |y_i| \quad (3.1)$$

- The root mean square deviation of the roughness profile from the mean line:

$$P_q = \sqrt{\frac{1}{n} \sum_{i=1}^n y_i^2} \quad (3.2)$$

- The total height of the roughness profile:

$$P_T = P_P - P_V \quad (3.3)$$

where n is the number of data points in the direction perpendicular to the mean plane, y is the surface height relative to the mean plane, P_P is the maximum profile peak height and P_V is the maximum profile valley depth.

Notice that some papers also mention skewness and kurtosis [96]. Those parameters are descriptors of the shape of a probability distribution. The interpretation of those values is delicate and we will thus focus on the three first (and more commonly used) parameters in our analysis in order to check whether interesting behavior may already be noticed from those features.

► Contour and mean plane definition

In order to apply Equations (3.1), (3.2) and (3.3) to bone surface, it is required to define two features: the profile line and the mean plane. The profile line may be defined as the contour voxels of the bone within the region under study. However, the definition of an objective mean plane requires more vigilance.

The most direct way would be to consider an horizontal mean plane, as it is often done with metals. Nevertheless, such a choice might be delicate in situations where the surface has waviness that should not be included in the roughness.

A second approach can be to apply a Gaussian filter with an high standard deviation (up to $\sigma = 5$) in order to smooth the contour of the bone and use that smoothed surface as a reference plane. However, in that case, the issue is that small holes situated beneath the border are likely to generate an artificial cavity that would influence our computation.

Finally, we chose to approximate the profile line with a 5th order polynomial. This ensures us to avoid the incorporation of waviness effects as well as cavities generated by holes under the surface. The order has been chosen so that the curve was nicely following the shape of the contour without including high rugosities. This fitting is illustrated for the reference slice of specimen 2 in Figures 3.15g, 3.15h and 3.15i.

Once those aspects are well defined, one last parameter has to be determined: the method to compute the so-called "distance" between the profile line and the mean plane. Indeed, we can either consider the vertical distance between each point of those curves, or evaluating the shortest distance between them. Both methods will be implemented in order to check whether our conclusions are robust against that choice. Minimum distance is computed thanks to a **Matlab** function called `dsearchn` based on the Quickhull algorithm (see more information in [8]).

It should also be noticed that all the above-mentioned calculations will be applied on several regions of interest. Therefore, it is crucial to ensure a fair comparison among them. However, both methods for distance assessment are rotation dependent: if the image is rotated of 5°, this leads to roughly 1 % of variation in the parameter computation. Thus, each ROI will be rotated so that its average orientation is horizontal, as illustrated in Figures 3.15a, 3.15b and 3.15c (yellow dashed lines).

Once all those settings are fixed, Equations (3.1), (3.2) and (3.3) may be applied.

► Characterization of the outputs

In order to highlight that roughness might be a parameter of adaption of bone structure at the tendinous attachment, several sites will be considered and compared in terms of the aforementioned parameters: the supposed insertion site (referred to as "bottom"), as well as the "middle" and the "top" regions. Each area will be associated with three roughness parameters and then confronted with each other (along 10 slices).

3.3.5 Statistical testings

The procedures described in the three previous subsections will be in each case applied to 10 slices independently in order to evaluate significant differences. Analyses of porosity and orientation will be conducted on both specimens, whereas roughness will be studied on specimen 2 exclusively.

The method for assessing statistical robustness is the following. Because our aim is to determine whether two sets of data are significantly different, the advised hypothesis test is a Student's *t*-test, specifically a two-sample *t*-test. This one is testing whether data from each group come from independent random samples of normal distributions with equal means and equal but unknown variances. The alternative is that data come from populations with unequal means.

However, this testing requires two conditions. First, the populations being compared should follow a normal distribution. This can be checked by applying a normality test such as a Kolmogorov–Smirnov test. Secondly, they should have the same variance. This second condition can be checked using a two-sample *F*-test. If one of those criteria is not met, the alternative testing is a Mann–Whitney *U*-test (also called the Wilcoxon rank-sum). In this case, the null hypothesis being tested is slightly different: one wants to know whether it is equally likely that a randomly selected value from one sample is less than or greater than a randomly selected value from a second sample. Whatever the test conducted, the final output tells us whether the two sets of data are significantly different or not.

Matlab toolbox of statistics and machine learning provides functions for statistical testings such as `kstest`, `vartest2`, `ttest2` and `ranksum` that respectively conduct a Kolmogorov–Smirnov test, a two-sample *F*-test, a two-sample *t*-test and Wilcoxon rank-sum test. The procedure is illustrated in Figure 3.16.

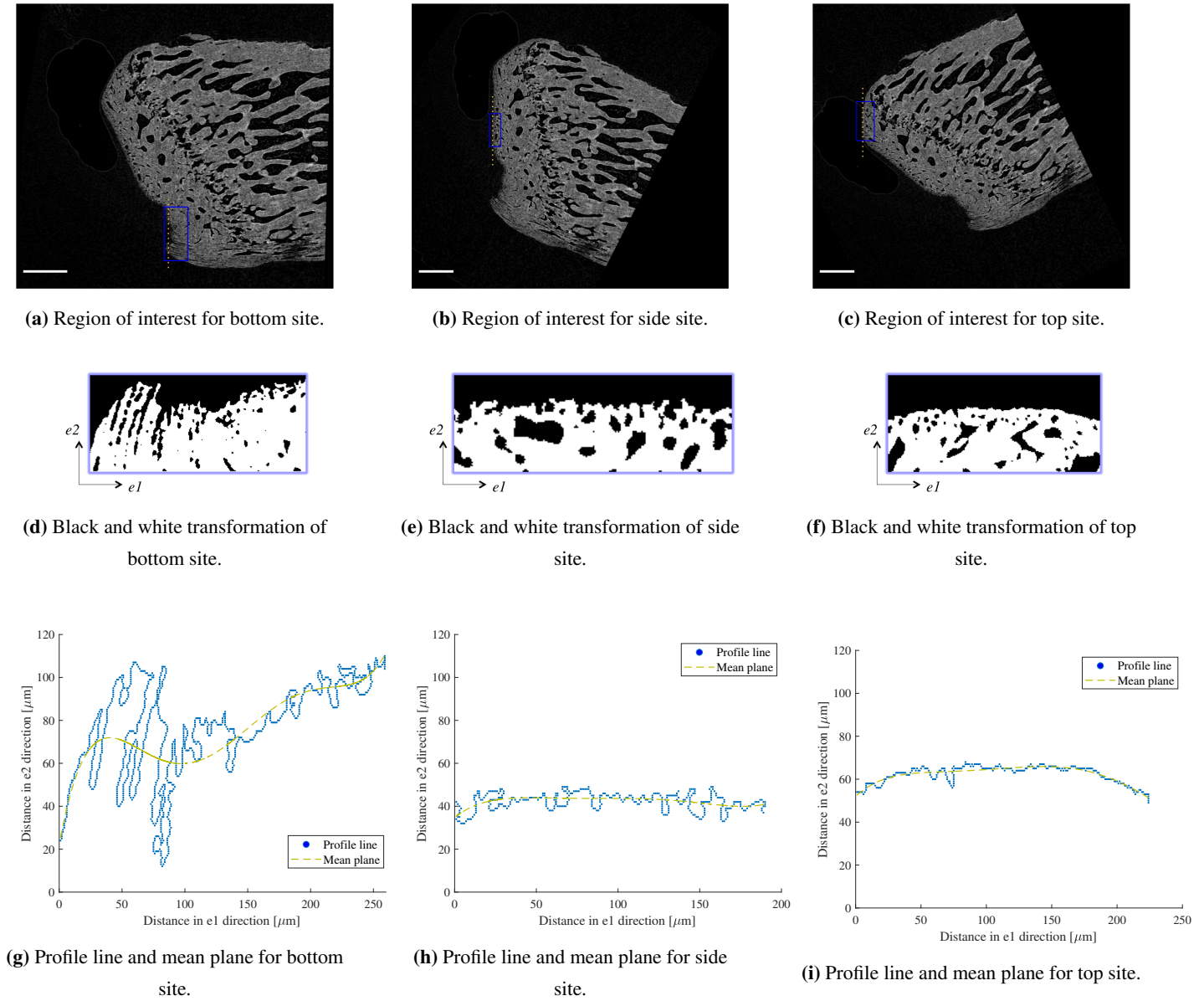


Figure 3.15: Illustration of the main steps followed in order to deduce roughness parameters of our three regions of interest: bottom (first column), side (second column) and top (third column) sites. First row represents the selection of the regions of interest on initial grayscale images. Yellow dashed lines illustrates the rotation of images to get the 'mean surface' aligned vertically. Second row shows the regions of interest after thresholding. Third row exhibits the deduced profile lines and mean planes for each region. Scale bar: 500 [μm].

All the tests have been conducted at the 0.1 % significance level. The informative box 1 provides additional explanations regarding hypothesis tests, null hypotheses and significance level.

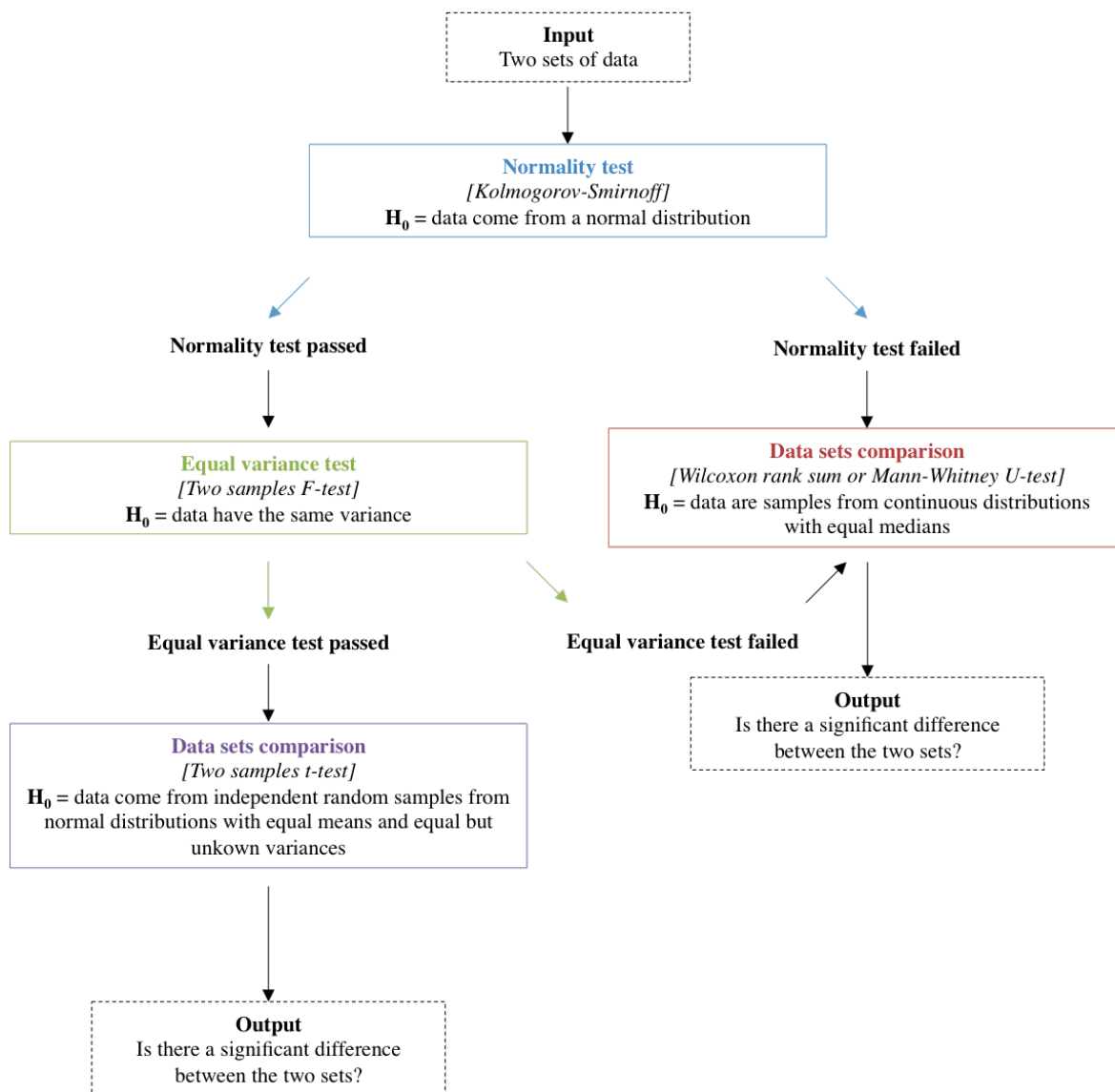


Figure 3.16: Scheme summarizing the procedure followed and the different tests conducted for statistical testings.

Box 1: HYPOTHESIS TESTINGS

In statistics, the main goal is to test a hypothesis. Hypothesis testings enable to evaluate the results of an experiment to see whether they are meaningful. To do so, we basically figure out the odds that those results have occurred by chance rather than because of a proposed explanation.

In order to conduct a hypothesis test, one needs to first state a research hypothesis. This one is called the null hypothesis (H_0), and its negation is called the alternative hypothesis (H_1).

Then, as we have seen in our own procedure, it is important to characterize the distribution of the samples in order to avoid erroneous conclusions.

The next step consists in calculating the P -value. This one is the probability of an observed result assuming that the null hypothesis is true.

Before drawing conclusions, one must decide the significance level (in our case, 0.001).

Finally, the null hypothesis is rejected (an the alternative hypothesis is accepted), if and only if the computed P -value is less than the significant level. This means that we consider it acceptable to have a 0.1 % probability of rejecting the null hypothesis when it was actually true. This error is called type I error or false positive. It is a "false hit".

However, another type of error can be made and is called type II or false negative. It consists in accepting the null hypothesis, and therefore rejecting the alternative hypothesis when it was actually true. It is a "miss".

There is a trade-off between those two: decreasing one increases the other. In our case, we took a low threshold, which means that we reduce type I error but increase type II error: we reinforce the power of the results considered as significant.

3.4 Results

In this section we describe the main results of the structural analysis, focusing on porosity, orientation and roughness.

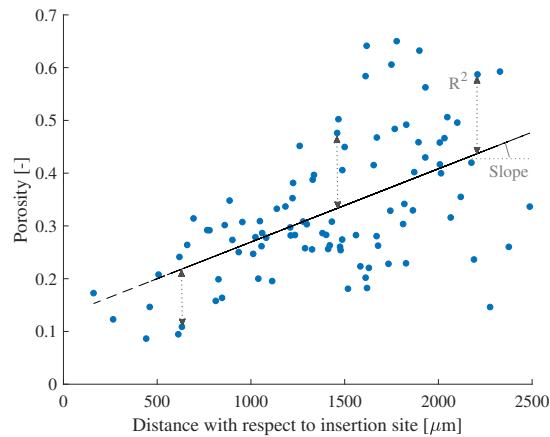
3.4.1 Porosity

In this subsection, the results of the porosity analysis are presented. Three aspects have been investigated in both specimens: the variation with distance from insertion, the evolution when going from the outer shell into bone as well as the spatial organization of porosity.

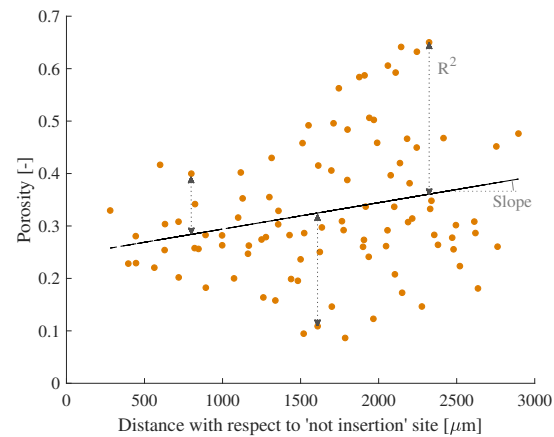
► Evolution of porosity with distance to insertion point

This first analysis consists in comparing the evolution of porosity when moving away from insertion point or from another location referred to as "control" point. Figures 3.17a and 3.17b shows the kind of plot obtained when computing such trend and illustrates the parameters characterizing it (slope and R^2 value).

Figures 3.18a and 3.18b show the systematic evaluation of those parameters for the slices of interest, respectively in specimen 1 and specimen 2.



(a) Porosity evolution when the reference point for distance computation is at the insertion site.



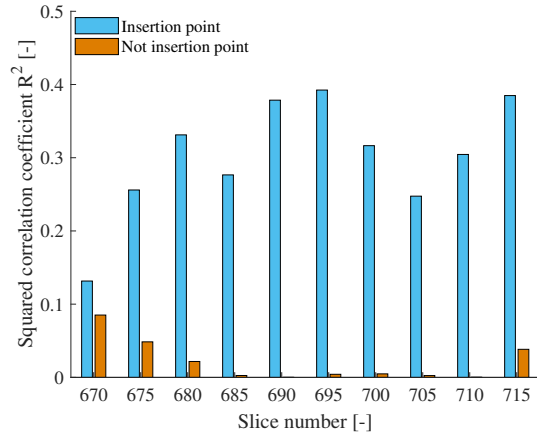
(b) Porosity evolution when the reference point for distance computation is not at the insertion site.

Figure 3.17: Evolution of porosity with distance for the reference slice of specimen 2 (n° 1005).

Even though those graphs already show an obvious difference between the two starting points, statistical confrontation of those results ensures that there is indeed a significant difference ($P < 0.001$) in the coefficient of determination when moving away from the insertion point or from another origin on the top of the bone.

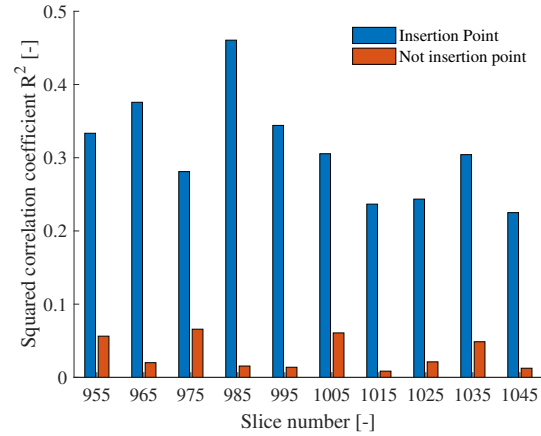
In terms of bone adaptation, this means that porosity exhibits a more controlled variation around the insertion region. Indeed, even though R^2 range is not very high (less than 0.5), there is still significantly less scattering around the linear approximation when the insertion is considered.

► Evolution of porosity with horizontal distance



(a) Comparison of the coefficient of determination of porosity evolution with distance, computed for insertion and not insertion site, over the 10 slices (specimen 1).

$P < 0.001$ (*).

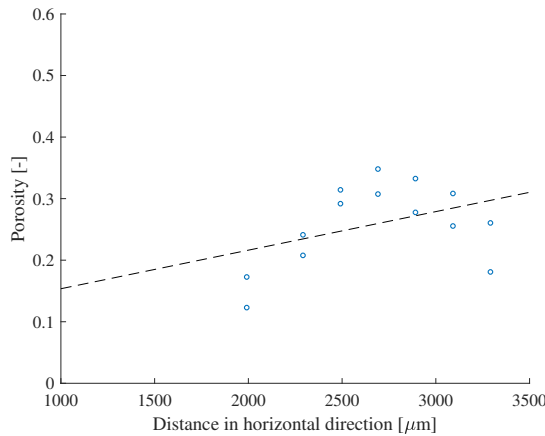


(b) Comparison of the coefficient of determination of porosity evolution with distance, computed for insertion and not insertion site, over the 10 slices (specimen 2).

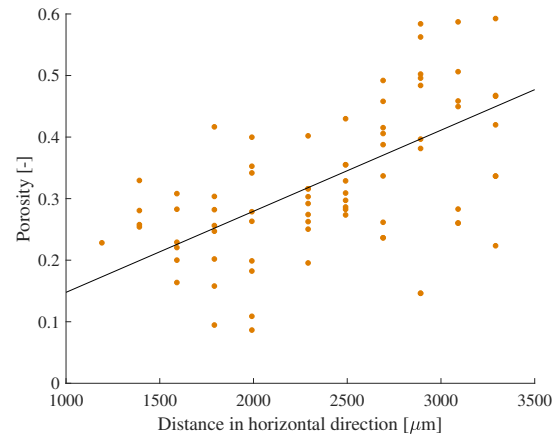
$P < 0.001$ (*).

Figure 3.18: Results of the porosity analysis (R^2 values) over the 10 slices of interest for both specimens.

In order to deepen information provided by the last analysis, we distinguish bottom (insertion) and top regions (see Figure 3.11) in terms of porosity. Evolution with horizontal distance (meaning progressing deeper in the bone structure) for both areas is shown in Figure 3.19 .



(a) Porosity evolution for the bottom region (aligned with insertion).

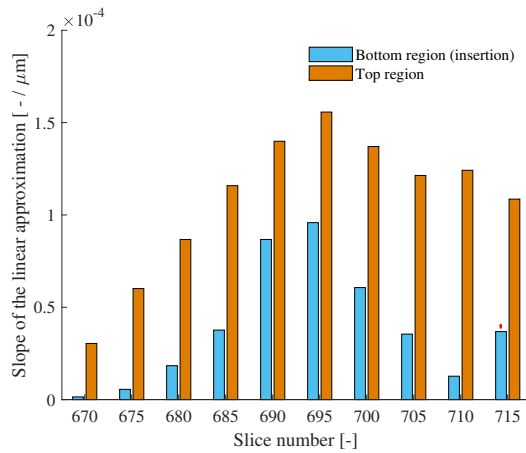


(b) Porosity evolution for top region.

Figure 3.19: Evolution of porosity along each row of the grid for the reference slice of specimen 2 (n° 1005).

Figures 3.20a and 3.20b show the results of the assessment of the slope represented here-above for all the slices of interest in both specimens.

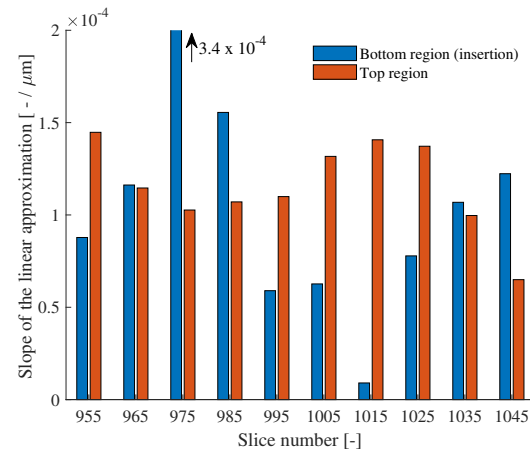
What can be learned from those plots is that the increase in porosity when entering the bone is steeper for top than bottom region. This result is significant for specimen 1 ($P < 0.001$). Although the trend is also observed in specimen 2, it does not reach significance ($P = 0.3447$). A plausible explanation could be the hole mentioned in the Pre-processing subsection (1.3.1).



(a) Comparison of slopes of the linear approximation of porosity evolution with distance in horizontal direction, computed for bottom and top region, over the 10 slices (specimen 1).

• : this value was initially negative but absolute value has been computed for representation purposes.

$$P < 0.001 (*)$$



(b) Comparison of slopes of the linear approximation of porosity evolution with distance in horizontal direction, computed for bottom and top region, over the 10 slices (specimen 2).

Arrow indicates the value for slice 975. Axes limits have been changed for better comparison with specimen 1.

$$P = 0.3447$$

Figure 3.20: Results of the porosity analysis (slope comparison between bottom and top region) over the 10 slices of interest for both specimens.

Indeed, this generates an artificial drop in the porosity that probably increases the slope of the approximation in some slices. It is for example the case for slice n° 975 where in addition, the removal of unconnected components generates another big hole in the bottom region, as can be seen in Figure 3.21. Those are increasing a lot the porosity far from insertion and this leads to an extreme value of the slope.

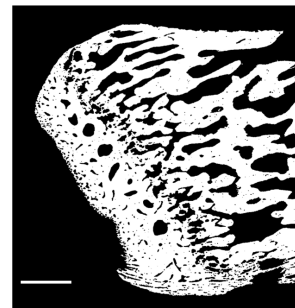


Figure 3.21: Slice n° 975 after processing. Scale bar: 500 [μm].

Together with the results extracted from the first analysis, this trend suggests that spatial variation of porosity is likely to be part of a strategy developed by bone in order to ensure a smooth transmission of the loading coming from the tendon.

► Evolution of porosity with distance and angle to insertion

3D spatial variation of porosity as a function of distance and angle from insertion has been extracted for each slice and then the average value over the 10 slices is considered for each ROI. The result is shown in Figure 3.22a and 3.22b. A few comments can be made. First, those plots show that the most porous region is located at around 40° and high distance from insertion for both specimens: this could also be observed in the pictures.

In addition, we have computed the global bone area of each specimen. Resulting value is 0.7761 for specimen 1 and 0.6763 for specimen 2. It can be clearly noticed on the 3D plots that specimen 2 is globally more porous than specimen 1. Interesting is that the high porosity of the central region remains approximately at the same level, whereas the loss in porosity is more located

on the contour of the bone.

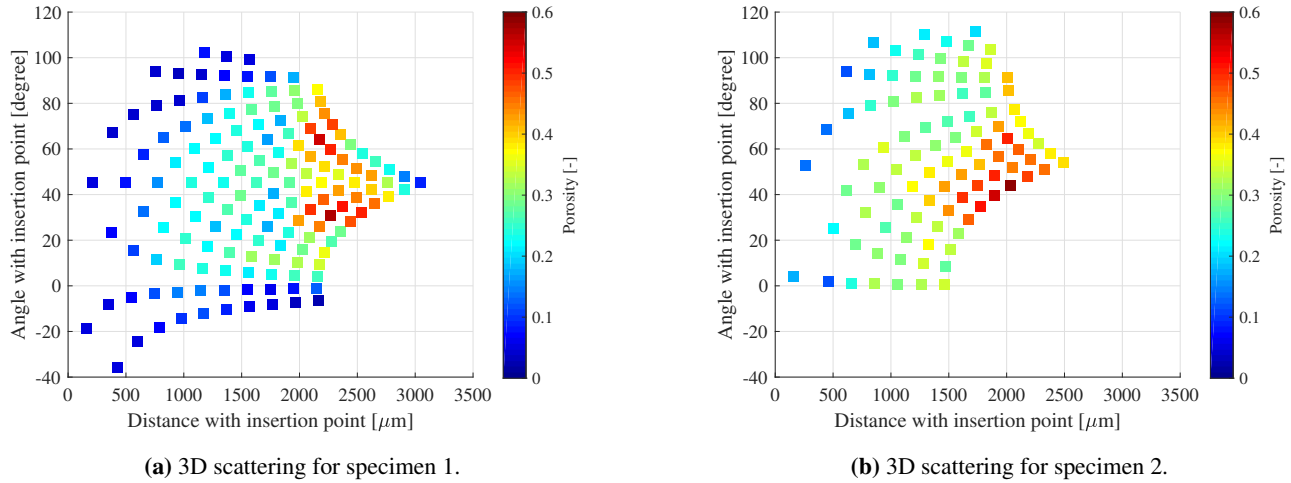


Figure 3.22: 3D evolution of porosity with distance and angle.

It can be noticed that specimen 1 has been investigated in a higher number of regions of interests (due to bigger size).

3.4.2 Orientation

In this subsection, results of the orientation analysis are described. Figure 3.23 illustrates, for the usual reference slice of specimen 2, the kind of histograms that can be extracted from each region. Those ones show the distribution of the orientations of the pores for top and bottom region. Only pores exhibiting a size bigger than the predefined threshold (35 [μm]) are considered on those plots. Histograms seem to indicate that in both regions, mean orientation of the pores is around zero degree (which means oriented horizontally). However, another feature is interesting: the distribution of the orientations around that mean. For visualization purposes, a Gaussian distribution is fitted (via a least square method) to the values of the histogram. This shows that the distribution of the top region is more scattered and the Gaussian approximation is quite broad. On the opposite, bottom region exhibits a reduced dispersion and the Gaussian looks much more narrow.

In order to quantify this observation, the standard deviation of the distribution of pores orientations is extracted for each region. Figures 3.25a and 3.25c represent the value of this parameter for all the slices of interest. There is a significant difference in the value of the standard deviation between top and bottom regions for holes of size above the threshold ($P < 0.001$). In addition, when considering very small size holes (below the threshold), no significance is reached anymore, neither for specimen 1 ($P = 0.3447$), nor specimen 2 ($P = 0.0376$). Histograms may be found in Figures 3.25b and 3.25d. The same procedure has been applied using a lower threshold (20 [μm] in perimeter). Results show no significance either ($P = 0.1733$ for specimen 1 and 0.064 for specimen 2). Resulting plots are found in Appendix E.

Those results demonstrate that the insertion region exhibits significantly more anisotropy, meaning that pores are adopting a preferred orientation, than the rest of the bone. In other words, bone seems to show another strategic adaptation in the orientation of its pores beneath the insertion of the tendon. As already mentioned, it is plausible that this orientation consists in a "line-of-force" transmitting loading from enthesis (of the Achilles) to another (of the plantar fascia). However, further investigation would be required to demonstrate that connection.

One can also notice that the issue of the artificial hole in the bone is affecting our results. However, as can be observed in Figure 3.24, that particular region is also including highly oriented trabeculae. Therefore, it is very likely that its inclusion into our computation would reinforce our conclusions.

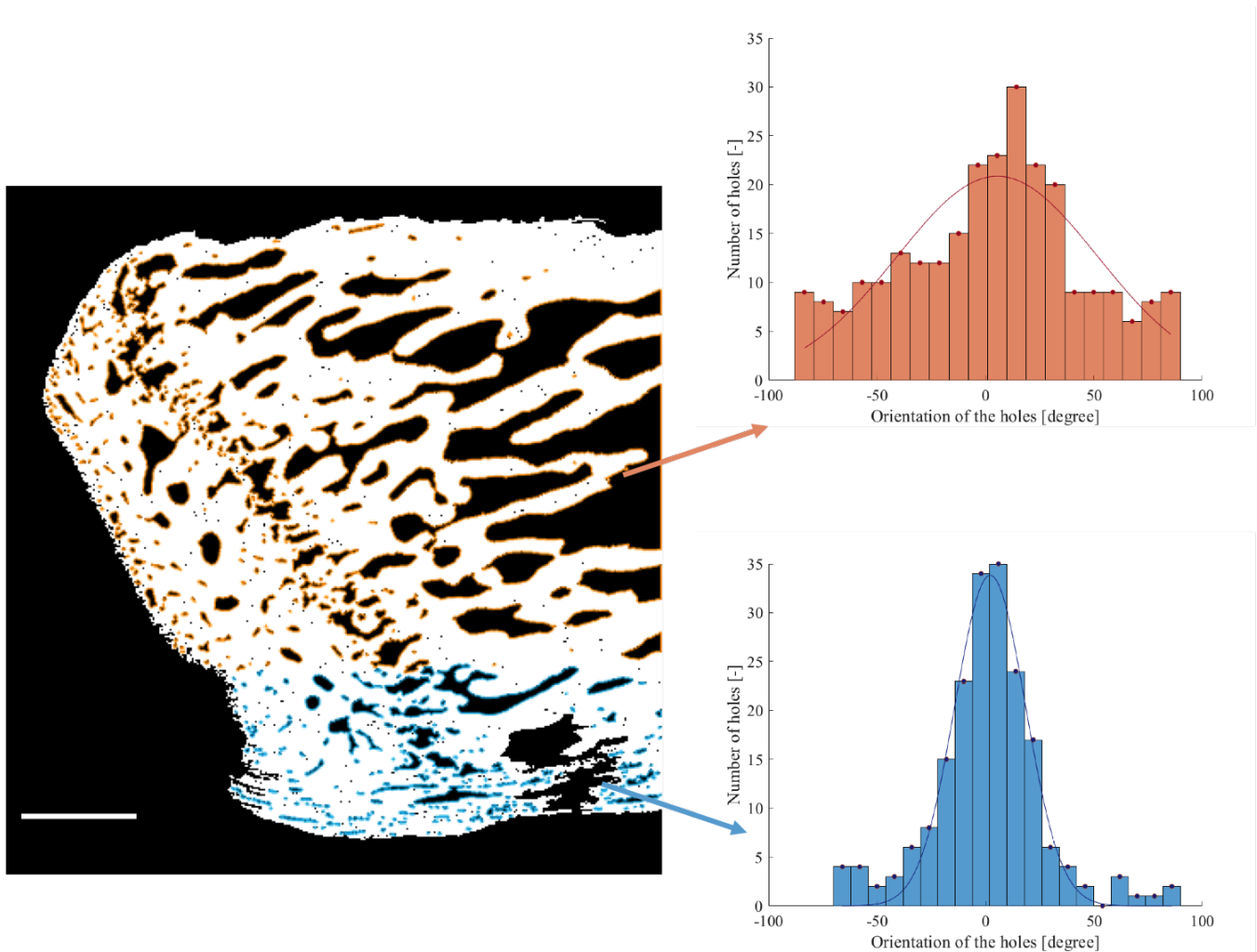


Figure 3.23: Example of histograms obtained when computing orientation of holes in **top** and **bottom** regions, for the reference slice of specimen 2 (n° 1005). Scale bar: 500 [μm].

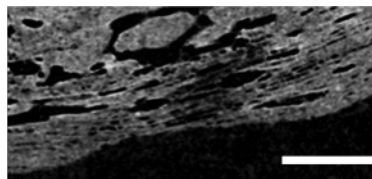
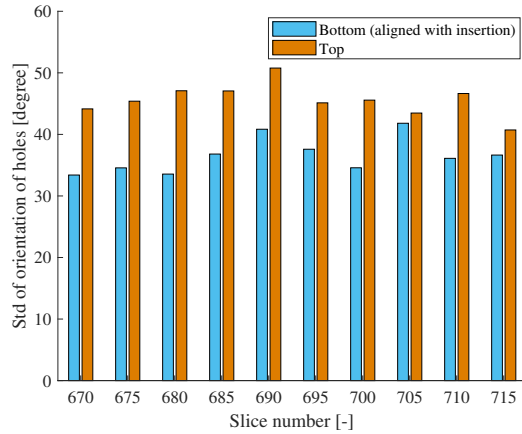
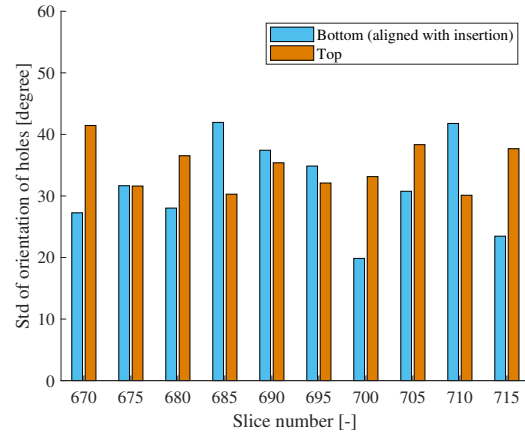


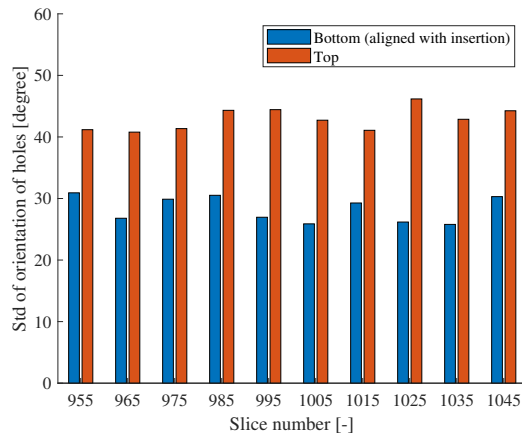
Figure 3.24: Zoomed image of the 'hole' generated by the thresholding: it can be noticed that the very thin trabeculae are aligned with the rest of the region as well. Scale bar: 250 [μm].



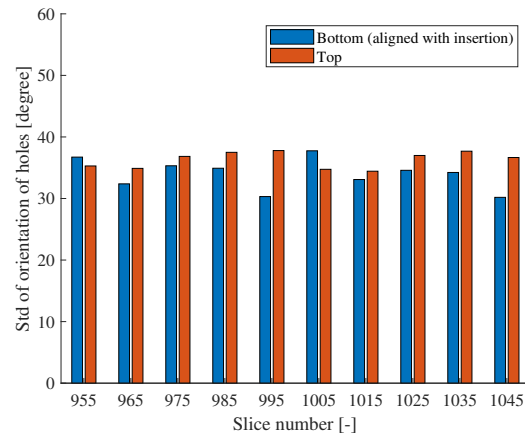
(a) Comparison of the standard deviations of the orientation of the pores in top and bottom regions, for holes bigger than the threshold (specimen 1).
 $P < 0.001$ (*).



(b) Comparison of the standard deviations of the orientation of the pores in top and bottom regions, for holes smaller than the threshold (specimen 1).
 $P = 0.3447$.



(c) Comparison of the standard deviations of the orientation of the pores in top and bottom regions, for holes bigger than the threshold (specimen 2).
 $P < 0.001$ (*).



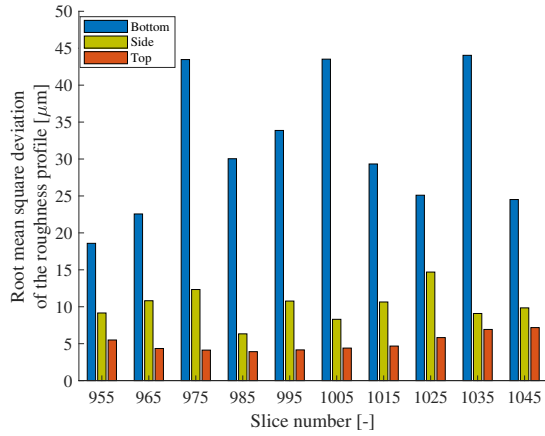
(d) Comparison of the standard deviations of the orientation of the pores in top and bottom regions, for holes smaller than the threshold (specimen 2).
 $P = 0.0376$.

Figure 3.25: Results of the orientation analysis (standard deviation of the holes angles) over the 10 slices of interest for both specimens.

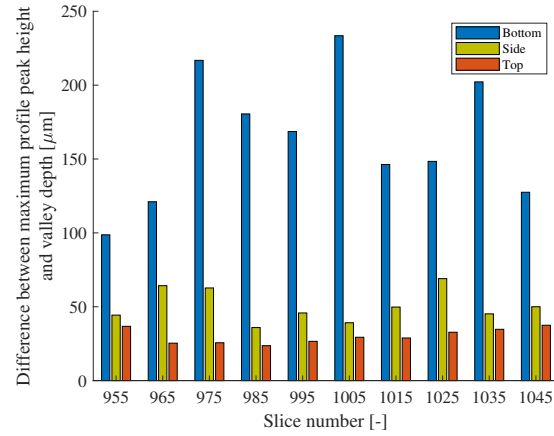
3.4.3 Roughness

The purpose of this subsection is to present results of roughness analysis. Figure 3.26 illustrates the output values over the 10 slices, and for two roughness parameters: P_q and P_T (see section 3.3.4). As P_a conveys the same message as P_q , therefore values will be represented in Appendix F. The method used to compute distance between the profile line and the mean plane does not affect the trend shown by those plots therefore only values computed with vertical distance are displayed here. Results when considering minimum distance can be found in Appendix F as well.

Measuring roughness at three different locations yields always to significant difference whatever the method used. Data is also presented in Table (see 3.2) showing the percentage decrease in each parameter from one region to another. It can be shown that,



(a) Comparison of P_q values for the three regions of interest (bottom, side and top), computed using vertical distance.
 $P < 0.001$ (*) between each subgroups.



(b) Comparison of P_T values for the three regions of interest (bottom, side and top), computed using vertical distance.
 $P < 0.001$ (*) between each subgroups.

Figure 3.26: Results of the roughness analysis (P_q and P_T parameters) over the 10 slices of interest for specimen 2.

for example, P_q is decreasing by 67% from bottom to middle region and by 83 % considering to the top region.

Those results highlight the fact that insertion region is characterized by a high roughness, when compared to other regions of the bone surface. Given what we know about enthesis structure, this roughness is probably originating from interdigitations of the bone into the tendon. In addition, it is interesting to notice that roughness on the middle region is significantly higher than on the top. This could be due to the fact that, as we have seen in Chapter 1, this area is covered by the periosteal fibrocartilage. Therefore, it could be that this roughness is due the anchoring of that fibrocartilage to bone.

	P_q [μm]	Δ [%]	P_q (min) [μm]	Δ [%]	P_T [μm]	Δ [%]	P_T (min) [μm]	Δ [%]
BOTTOM REGION	31.5	/	29.47	/	164.3	/	88.1	/
SIDE REGION	10.2	- 67.6%	10.1	- 65.7 %	50.6	- 69.2 %	28.7	- 67.4 %
TOP REGION	5.1	- 83.8%	4.9	- 83.4 %	30.1	- 81.7 %	17.9	- 79.7 %

Table 3.2: Mean values of each roughness parameter, illustrating the percentage of decrease in those parameters from bottom region to the side or top one.

3.5 Discussion and conclusions

The purpose of this section is to provide a critical review of the results of structural analysis, as well as to conclude this chapter with the most relevant findings.

Firstly, it is obvious that the main weakness of our study lies in the number of specimen investigated. Indeed, only two rats were available. However, in order to strengthen our results, a larger number of samples would be required. Considering reduced variability of rats of the same strain, three should be enough.

Secondly, porosity computation was influenced by the presence of holes generated by our pre-processing steps. In order to get rid of some of them, one could implement a local threshold in the region where the very thin trabeculae are located. However, even this method does not seem completely accurate because it leads to an "unfair" processing of the regions of the bone and that could be misleading, as it may introduce an artificially higher bone volume fraction there.

Regarding the other holes generated by the removal of unconnected components, it is obvious that the solution would be to extend the analysis to three dimensions. Indeed, the "unconnected" objects detected by **Matlab** are very likely to be connected in the third dimension.

Regarding our orientation analysis, one should remain critical regarding the evaluation of the threshold separating "big" and "small" features. Indeed, it has been shown that characterizing bone microarchitecture was highly influenced by resolution. Moreover, it has been determined that a μ CT resolution of 1-2 [μ m] was appropriate for measuring vascular porosity, whereas at least 1 [μ m] would be necessary when computing osteocyte lacunae¹ [90]. Because the resolution of our scans are respectively 2.5 and 5 [μ m], one must keep in mind that are measurements have limited accuracy for features of very small scale. Figure 3.27 shows the influence of scanning resolution on vascular canal diameter assessment.

The exact value of 10 [μ m] might be questionable given the resolution effect as well as the lack of specific literature regarding micro-architecture in calcaneus bone. However, the goal of such a threshold is more to reduce noise that could arise when considering very small holes in orientation computation. In addition, we have shown in the results section 3.4 that the chosen threshold is actually persistent when looking at the results in terms of adaptation (no adaptation for small features).

Moreover, a weak point of our orientation analysis is that our procedure to compute orientation of the pores is granting the same weight to each hole, whatever the size. Alternative approach could be to associate to each a hole a weight proportional to its size so that big holes have more influence of the final orientation analysis. However, in that case, we would loose some information at the interface, were pores are generally small.

Another aspect that can be discussed concerns the number of pores in the bottom and top region. Indeed, the bottom region covers a larger part of the bone and thus it comprises more pores. One could think that this would increase the probability of having more scattering in the distribution of the orientations of the pores. However, it turns out that the standard deviation of a set of data is decreasing with its size, as it gets closer to the mean value.

Finally, the method followed to compute roughness is limited by the lack of literature to compare with. Exploiting formulas originally defined for metals and manufactured material in the case of human tissue might be questionable. Indeed, bone rugosity is not like any man-made surface profile. For example, it comprises big cavities (especially at insertion site) that make our interpretation of distance to the mean plane delicate. Anyway, our goal was to make relative comparisons among different regions on the same sample and not to give absolute roughness value.

¹ A lacuna is a small space containing one single osteocyte, and connected to other lacunae through the canaliculi.

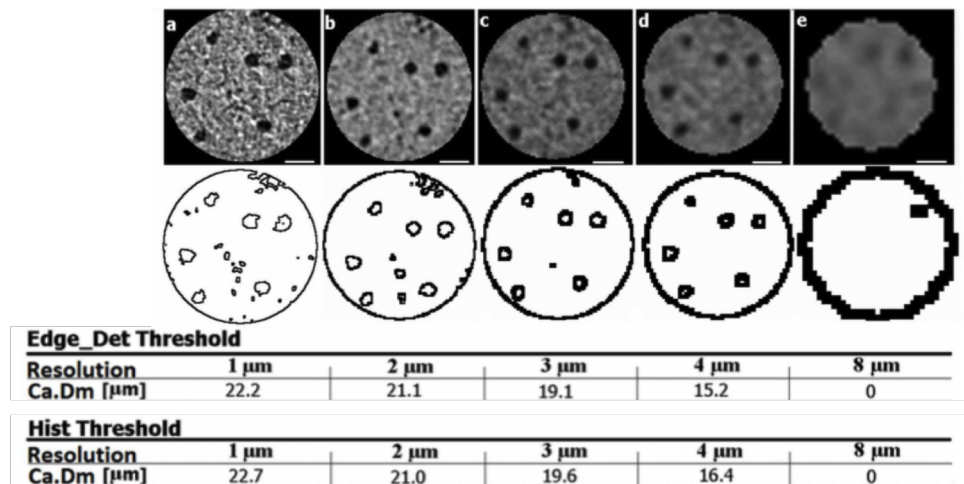


Figure 3.27: Illustration of the effect of scanning resolution on vascular canal diameter (Ca.Dm) measurement for two different methods (Edge_Det and Hist) [90].

That being said, our analysis has emphasized several interesting features of bone structure that should be kept in mind for further investigation:

- The porosity is gradually increasing from the insertion site to the interior of the bone. This gradual increase seems to be more controlled than when considering another location on the bone surface, far from the insertion point.
- The insertion region display significantly more anisotropy than the rest of the bone.
- The bone surface at the insertion show significantly more roughness than regions of interest located away from insertion. In addition, middle region is characterized by higher roughness than top region, which could be due to the anchoring of periosteal fibrocartilage.

We believe that those findings are part of a strategy developed by bone to deal with the high materials mismatch caused by the tendinous attachment as well as to ensure a smooth transmission of the loading generated by the tendon. In order to reinforce those results, the second part of this thesis will focus on biomechanical implications of our analysis.

Chapter 4

Biomechanical study

4.1 Introduction

The second part of this project has the purpose of investigating the biomechanical behavior of calcaneus bone subjected to loading from the Achilles tendon. The aim is to characterize how stresses are distributed in the bone, also in view of the main results of the structural analysis. To do so, we make use of a high resolution micro-finite element model.

This thesis is motivated by the Achilles tendon enthesis with a focus on bony side rather than tendinous part. Therefore, it has been decided to simplify the finite element model in regard to the tendon. The major role of this part of the model is therefore to allow us to apply loading conditions at a proper attachment and considering a realistic mismatch in elastic properties between tendon and bone. The Achilles tendon is simply manually built via **Matlab**. This actually allows us to fully exploit the strength of computer modelling. Indeed, in addition to the simulation of "natural" insertion of the tendon, located at the bottom region mentioned in previous chapter, we take advantage of our model to simulate a "wrong" insertion site at the top of the bone. This kind of "thought" experiment takes advantage of non-occurring situations in order to better understand the original arrangement. The aim here is to highlight interesting behaviors between the two sites and better understand the role of structural features in stresses propagation and distribution.

This chapter is divided into three parts. Our method consists in the development of a finite element model of the Achilles tendon and calcaneus bone. Therefore, we review the commonly addressed steps in the context of FE analysis: geometry, meshing, material definition, loading conditions as well as solver characteristics. Finally, the processing of the outputs prior to final analysis is explained.

The second part focuses on the simulations conducted with the developed model. Those simulations allow us to better understand the flow of stresses within the bone, the influence of the tendon length, the effect of the material mismatch as well as to conduct our "thought" experiment assessing robustness of bone towards change in force orientation at distinct locations.

Lastly, our results are discussed and contrasted with the limitations of our model and we will conclude by providing key messages regarding biomechanical behavior of bone beneath Achilles tendon insertion.

4.2 Methods

The subsequent biomechanical analysis is performed exclusively on one reference slice of specimen 2 (n° 1005). Sticking to a two dimensional model is the consistent continuation of our structural analysis and allows us to draw parallels between our findings. The choice of using specimen 2 instead of specimen 1 is based on the decision to build a high resolution FE model.

Notice that, for this part of the thesis, the $y - z$ plane previously defined will be referred to as $x - y$ plane.

Considering the interdisciplinary nature of this thesis, a short reminder on FE analysis is provided in the box 2 below.

Box 2: FINITE ELEMENT METHOD

The Finite Element Method (FEM) is a numerical technique that was born at the beginning of the 20th century. Basic principles have been developed by Ritz and Galerkin [111]. The goal is to avoid computing the analytical solution of a given system by reformulating the problem in a set of algebraic equations (instead of initial complex partial differential equations). The solution is restricted to a finite number of points over the domain. Therefore, finite element method is transforming a continuum problem, characterized by an infinite number of degrees of freedom, into a discretized problem, that has a finite number of degrees of freedom.

The basic principle is that the global displacement of the system is approximated by a combination of the displacement of a set of discrete points: the nodes. The displacement of the nodes is supposed to be linked with the external forces applied on the system through a matrix called the stiffness matrix. In order to compute that matrix for the whole system, this one is decomposed into smaller subsystems of simple geometry (such as a square or a triangle): the elements. The displacement of the nodes of each element are linked with the forces acting on the nodes of that specific element. This allows to compute element stiffness matrices that are then assembled to form the large and sparse matrix, with dimensions in the order of the number of nodes, characterizing the whole system.

The form of the element stiffness matrices depends on many factors, among which the type of element. This choice must therefore be done wisely because it has a huge influence on the results.

4.2.1 Geometry

Our model comprises two parts: the Achilles tendon and the calcaneus. The bony part is built directly on the μ CT data. Therefore, slice n° 1005 is imported and processed following the same steps as the ones described in subsection 3.3.1 : filtration, thresholding and removal of unconnected components. This last point is of major importance when pre-processing for FE analysis. Indeed, unconnected parts may be the source of numerical errors in the final model.

Regarding the modelling of the tendon, we had no experimental data. The tendon was built artificially with **Matlab**. Although the geometry is simplified, the goal of this procedure is too maintain high accuracy in the definition of the tendon-bone interface: in other words, we want the tendon to fit perfectly the roughness of the bone at the insertion site.

Therefore, the procedure illustrated in Figure 4.1 is applied. First, a simple rectangular shape is drawn. Then, the sides are curved using circles superposition. The obtained geometry is rotated and translated in order to superimpose with a "filled" version of the black and white image of bone. The latest is obtained by extracting the contour of the bone and then filling it using `imfilled` function of **Matlab**. The sites where bone and tendon overlap are deduced thanks to the following principle: as the tendon matrix is filled with "3" values, and the black and white image exhibits "1" voxels where there is bone, one only needs to subtract those two matrices. A value of "2" in the newly built matrix means there was bone, whereas if the value is still "3", there was no bone at that location. This idea is illustrated in Figure 4.2 . The last step consists in cutting the top part of the tendon to make it flat. This step allows us to control the arc length of the tendon and, as we will see in subsection ??, this parameter has actually a crucial effect on the simulations.

This procedure actually allows us to have a lot of freedom in the building of the tendon. Indeed, many parameters are tunable: the cross-section of the tendon, its arc-length, its orientation, as well as the position of insertion in the bone. The cross-section of

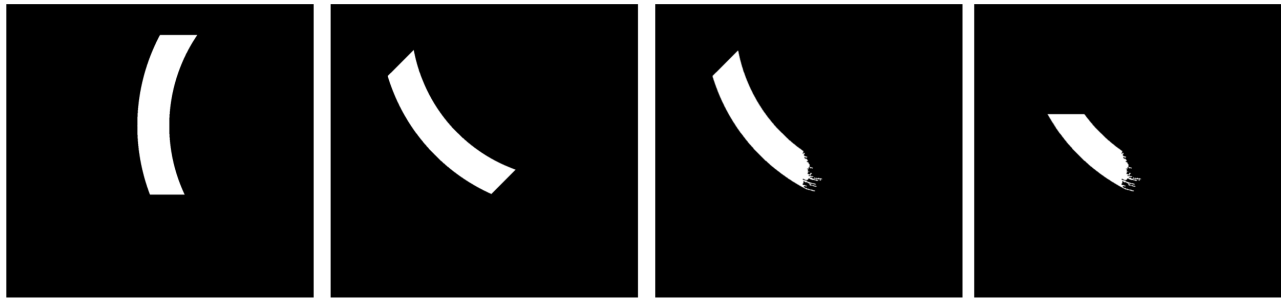


Figure 4.1: Representation of the steps followed in order to build a tendon with a highly accurate interfacial roughness (rotation, superposition, and recut at a specific arc length).

the tendon has been fixed to $375 \text{ } [\mu\text{m}]$ for all the simulations. However, the influence of the other parameters are investigated in the result section . It means that several additional tendons have been built in order to investigate resulting stress patterns when playing on those features. We implemented the following parameters investigations. First of all, arc length of the tendon has been increased and decreased by 25 %. Those two tendons are shown in Figure 4.3a.

Secondly, while keeping the arc length constant, the influence of the orientation will be studied and this implies two others configurations, with an increased orientation of 10 and 20 %. Resulting tendons are depicted in Figure 4.3b.

Finally, this easily tunable geometry allows us to consider another tendon insertion location at the top of the bone in order to conduct our "thought" experiment. This one is represented in Figure 4.4b.

Once geometries are built, binary images are exported and `.stl` files are generated using CTAn. As this pseudo-volume generation requires more than one slice, each geometry is replicated once in order to generate a 2D model with a virtual depth of $5 \text{ } [\mu\text{m}]$ (2 voxels).

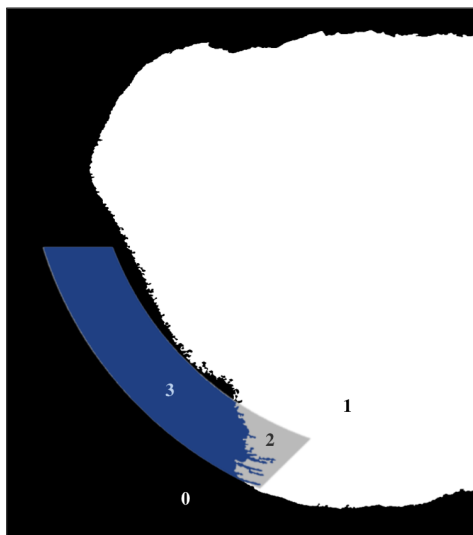
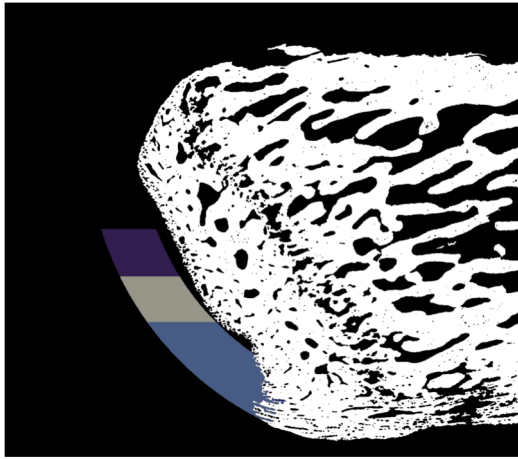
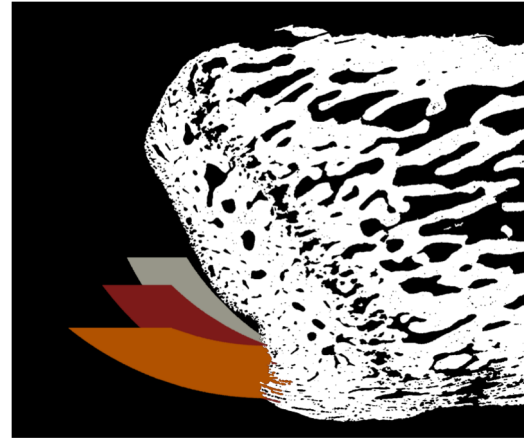


Figure 4.2: Illustration of the superposition of the tendon and the bone: while the tendon is assigned values of "3", bone is "1" and therefore areas where the subtraction gives "2" are deleted of the tendon geometry.

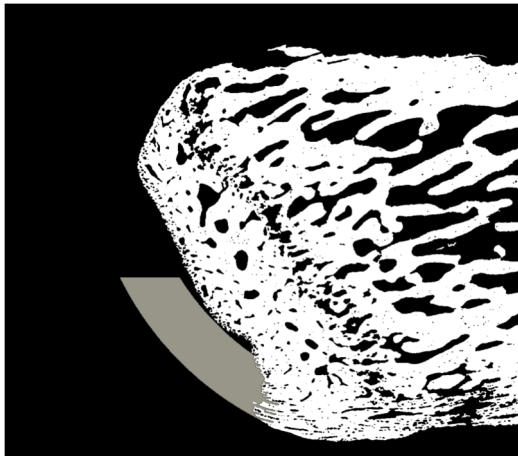


(a) Initial arc length, increased arc length of 25% and decrease arc length of 25%.

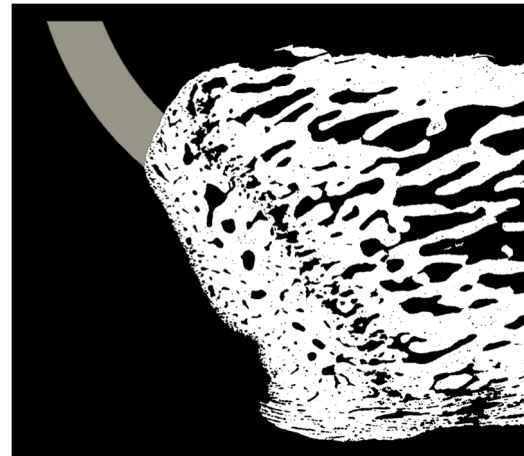


(b) Initial orientation, increased orientation of 10%, increased orientation of 20%.

Figure 4.3: Illustration of the tendon geometries built in order to study the influence of arc length and orientation on the output stresses.



(a) Tendon inserting at the "bottom", referred to as "biological" or insertion site.



(b) Tendon inserting at the "top", referred to as "control" or "wrong" insertion site.

Figure 4.4: Illustration of the tendon geometries and their location of insertion into bone.

4.2.2 Meshing

Once geometries have been built and extracted, they need to be meshed. For that purpose, the HyperMesh software is used. Specifically, the tight shrink wrap algorithm is exploited. Once geometries are imported (as a solver deck), this option enables to generate a tight-fitting mesh adhering closely to the underlying model [55, 5]. The resulting mesh comprises hexahedral elements. This kind of element, also known as a "brick" element, is a good compromise between accuracy and computing time for complex geometries.

Two parameters are tunable and allow to control the quality of the resulting mesh: the element size and the minimum Jacobian. The Jacobian, which is the abbreviated version of Jacobian matrix determinate, is a measure of mesh quality. Basically, it measures the distortion of a cubic element from a perfect cube (for which the Jacobian is 1). Figure 4.5 illustrates the shape of elements having a Jacobian lower than 1. Usually, there is a trade-off because decreasing the Jacobian enables the mesh to be closer to the original features, but it decreases element quality. This is why a threshold might be defined in order to mitigate those effects.

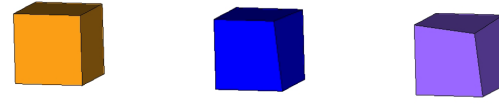


Figure 4.5: Illustration of the effect of the Jacobian on cubic elements: the orange cubic has a Jacobian of 1, the blue one of 0.942 and the purple one of 0.883. [58].

In our case, in order to ensure the fitting of the roughness of tendon and bone at the interface, we have imposed the minimum Jacobian to be equal to 1: this means that all the elements are perfect cubes. In addition, an element size of $2.5 [\mu\text{m}]$ is used so that each voxel is perfectly represented.

Characteristic features (number of nodes, elements, and type) of the resulting meshes of bone and reference tendons are shown in Table 4.1.

	Total number of nodes	Total number of elements	Type of element
BONE	2,154,519	1,124,430	C3D8
REFERENCE TENDON FOR BOTTOM INSERTION	210,456	137,724	C3D8
TENDON FOR TOP INSERTION	184,842	121,698	C3D8

Table 4.1: Total number of nodes and elements for the geometries meshes generated with Hypermesh (C3D8 elements are linear hexahedral elements in Abaqus).

4.2.3 Material definition

Once the meshes have been built, they can be imported as input files in Abaqus. Because tendon and bone have been built and meshed independently, they are imported as separate parts and therefore we can easily assign them distinct material properties.

► Bone material properties

Bone is assumed to behave as an isotropic, linear elastic material. Assuming small deformations, the second description is acceptable. However, bone is far from being uniform in all orientations, so the isotropy assumption is more limiting. Indeed, cortical bone is known to exhibit distinct Young's Modulus when subjected to loads parallel or normal to the long axis the bone: that is, it can be modelled as transversely isotropic material. On the other hand, trabecular bone is anisotropic as well: as we have seen, trabeculae network may be oriented in a specific direction, reflecting partly the predominant loading.

That being said, this limitation should be kept in mind. Nevertheless, for the simplified material considered, two parameters have to be fixed: the Young's modulus and the Poisson's ratio. While Poisson's ratio is commonly set to $\nu = 0.33$ [84], mechanical properties of bone are subjected to a higher variety among scientific papers. However, our model containing already structural elements of bone (meaning the trabeculae), we are looking for tissue level and not apparent level properties (therefore not con-

taining architectural behavior). Tissue level properties of rat bone may be assessed using nano-indentation. Values reported in literature [68, 47, 51] range from 5 to 25 [GPa]. Therefore, it has been decided to prescribe an intermediate value of $E = 15$ [GPa] to bone material.

► Tendon material properties

Computational models of tendons and specifically of Achilles tendons have triggered a lot of research in order to better understand material behavior. Those models are based on the definition of strain energy density functions that take into account the main components of tendons: the ground matrix and the collagen fibers. Most commonly, tendon is thus modelled as a transversely isotropic hyperelastic material including a Neo-Hookean behavior for the matrix. Behavior of the fibers may be described by different laws (such as a piece-wise function describing behavior in different steps, or a viscoelastic model) [105, 97, 7, 65]. However, as we have chosen to simplify our model regarding the tendon, we will describe it as a linear elastic material as well. Studies have reported global values of Young's modulus for rat Achilles tendon which shows variability depending on many factors such as the testing method, the age of the rat or its physical activity [6, 33, 49, 41, 64, 30, 29]. Given the fact that little is known about the state of the rats employed for our study, we have decided to fix the Young's Modulus to $E = 200$ [MPa], which is in the range of the values found in literature, with a Poisson's ratio $\nu = 0.45$.

4.2.4 Boundary conditions

The next important step in the development of a finite element model is to define the boundary conditions. First, one needs to define the contact conditions between the tendon and the bone. Secondly, because we restrict our study to a 2D model, we have to impose stresses to be restricted to a 2D plane. Then we have to decide where to fix the bone. Finally, the loading of the tendon has to be established. Figure 4.6 illustrates the boundary conditions applied.

► Contact conditions

Bone and tendon surfaces are connected through a tie constraint. This means that those surfaces are constrained to stay attached during the simulations. This condition is straightforward to apply because there is no need for sliding modelling.

► Plane stress

This condition has to be imposed in order to ensure that stresses are evolving only into the $x - y$ plane. Practically, this is enforced by applying a symmetry along the third direction (the z -axis): no displacement along this one, nor rotation around the x and y -axes are permitted (as they involve the third direction as well).

► Bone fixation

In order to avoid any singularity in the model arising from rigid body motion, one needs to fix the bone at some location. It has been chosen to encastre the lateral side of the bone for several reasons. Indeed, our region of interest will be mainly focused around the insertion. Therefore, the lateral side of the bone is the farthest region from it and we can assume boundary effects will have minimal impact on our results.

► Tendon loading

Finally, loading is applied on the tendon, by two different means: either through a displacement boundary condition, or through a force. The influence of this parameter will be studied in the next section. In both cases, the idea is to stretch the tendon, and the value was chosen so that small strains are generated and so that stresses reached in the bone remain critical stress. Literature is not unanimous once again. Ultimate compressive stresses for trabecular bone are recorded around 20 [MPa] [52]. Cortical bone displays failure values in the range of 200 [MPa] [60]. In order to stay below those values, we have decided to consider that bone stresses in the range of 10 [MPa] were acceptable.

First, a displacement of 250 [μm] has been applied at the extremity of the tendon. It can also be checked that this displacement is generating stresses in the tendon far any peak stress. Indeed, no higher stresses than 10 [MPa] are generated, whereas failure stress of Achilles tendon has been reported around 50 [MPa] [76].

A similar reasoning has lead us to consider a total applied force of 0.6 [mN]. Given the area over which loading is distributed, the force applied is equivalent to 0.3 [MPa], which is again far from any risk of damage area regarding the tendon properties.

In any case, the `NLGEOM` option of **Abaqus** has been turned off. This means that the softwares is ignoring large-deflection effects. That is, a small-deflection analysis is specified which is indeed what is required for our analysis.

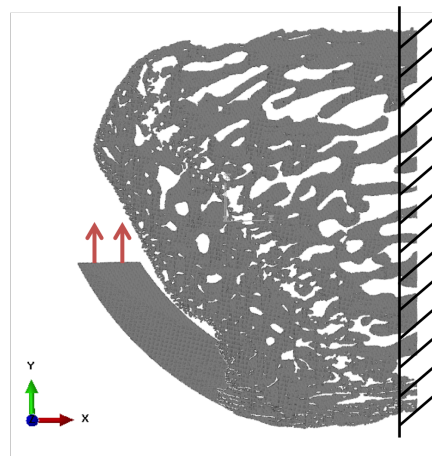


Figure 4.6: Illustration of the boundary conditions (loading of the tendon and fixation of the bone).

4.2.5 Solver features

The FE model with the listed above features is reaching a number of elements of 1,250,000 on average (bone and tendon meshes combined). It has been solved with **Abaqus** solver on a computer of the Auckland Bioengineering Institute (Auckland, New Zealand), in various situations that are described . Computer has an Intel® Core™ i7-6700 processor (4 cores) with 32 [GB] of installed RAM. Maximum number of increments per step is fixed to 100, with an increment size of 1 initially (10^{-5} minimum and 1 maximum). Monitoring of the job files teaches us that the model is usually solved using 1 step and 1 increment. Total CPU time required reaches 383.8211 [s] (5.5 [min]) when averaging for all the simulations (with a standard deviation of 45.4317 [s] among the simulations). Typical size of the output (`odb`) file is 2 [GB].

4.2.6 Outputs exportation

Once simulations are completed, qualitative observations can be done using visualization tools of **Abaqus**. Interestingly, stresses pattern and flow may be analyzed. Afterwards, those ones are exported in **Matlab** for further quantitative analysis. Notice that given our simplifications regarding tendon's behavior and geometry, this study will focus on stress propagation in the bone.

In order to understand the influence of some considered parameters, frequency distributions of stresses are confronted. Histogram values are extracted while imposing the same bin width, and later normalized in order to ensure fair comparison for cases comparing stresses from different region of interest (and therefore with distinct number of elements). Normalization has been implemented so that area under the curve is fixed to 1.

Moreover, **Abaqus** allows the investigation of many different outputs. It has been decided to focus on Von Mises stresses, as well as maximum and minimum principal stresses. Indeed, while the first type might be associated with shear, maximum and minimum principal stresses may inform us about tension and compression regions in the bone so those three outputs provide complementary information.

Details about the definition of those stresses may be found in the informative box 3.

Box 3: VON MISES AND PRINCIPAL STRESSES

This informative box aims at reminding the basics of principal stresses.

Given our plane stress approximation, the stresses acting on each element may be represented as shown in Figure 4.7.

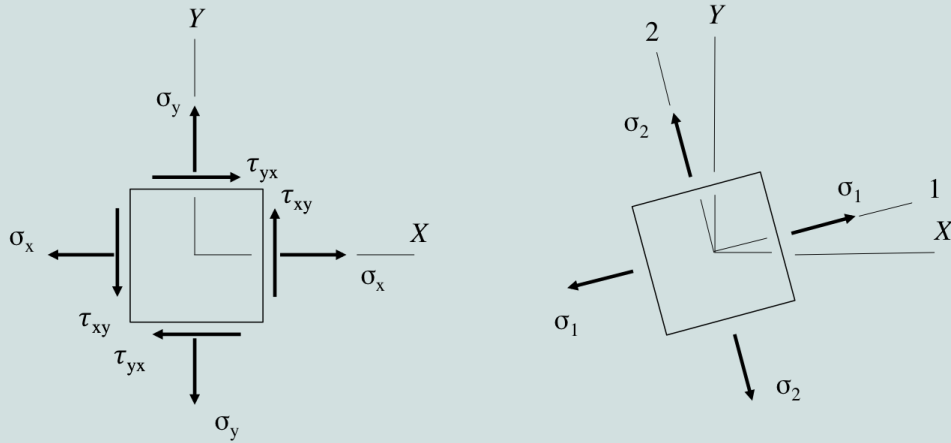


Figure 4.7: Illustration of the stresses acting in plane stress conditions: original stresses (left) and principal stresses (right).

Normal and shear stresses acting on an element vary depending on the coordinate set considered. There exists an angle where the shear stress becomes zero. This angle defines the principal direction where the only stresses remaining are the normal stresses: they are called principal stresses:

$$\sigma_{1,2} = \frac{\sigma_x + \sigma_y}{2} \pm \sqrt{\left(\frac{\sigma_x - \sigma_y}{2}\right)^2 + \tau_{xy}^2} \quad (4.1)$$

On another hand, Von Mises equation for a general plane stress write:

$$\sigma_{VM} = \sqrt{\sigma_x^2 - \sigma_x\sigma_y + \sigma_y^2 + 3\tau_{xy}^2} \quad (4.2)$$

Therefore, Von Mises stresses convey additional information about shearing, whereas principal stresses can teach us about tension and compression.

4.3 Results

In this section, results of the simulations conducted on our model are presented. First, we give a first insight of how the bone is reacting to the attachment of this highly dissimilar material that is the tendon (flow of stresses in the bone and location of peak stresses). Afterwards, the idea is to play with the parameters of our model in order to better understand its behavior. Therefore, after defining our region of interest for stresses extraction, we investigate how the length of the tendon is influencing the pattern. We study the effect of the material mismatch by increasing the stiffness of the tendon. That being done, we conduct our "thought" experiment in order to highlight whether the position of insertion, when compared to a wrong insertion site, is showing any advantage for stress propagation.

4.3.1 Preliminary observations

This subsection aims at giving a first overview of the consequences of the tendon's loading regarding stresses in the bone. Figures 4.8a, 4.8b and 4.8c illustrate respectively Von Mises stresses, maximum principal stresses (positive values) as well as minimum principal stresses (negative values). In this case, boundary condition applied was a force, and the geometry used is the reference one for the position of insertion.

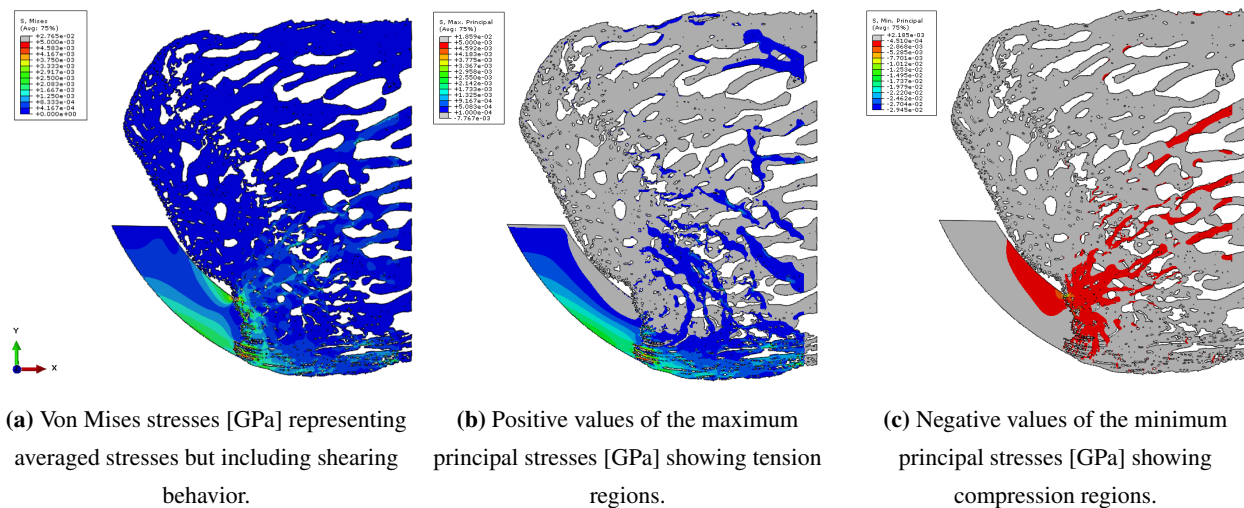


Figure 4.8: Output stresses for the reference arc length and orientation at bottom insertion, and a force boundary condition applied.

Distinction of tension and compression regions allow to observe a non-trivial stress flow within the bone. Indeed, stress pattern in tendon is exhibiting understandable compression and tension region resulting from the bending caused by the loading. Bone structure, however, is redirecting stress propagation in a way differing from what we could have expected with a simple cantilever beam analogy. Interestingly, it can be noticed that tension region is, on one hand, aligned with the oriented trabeculae of the insertion region. This could corroborate again the assumption of a "line-of-force" between Achilles tendon and plantar fascia insertions. On another hand, part of the tension stresses are directed upward, and perpendicular to the growth plate and to the general orientation of the microstructure (until far from insertion site). On the contrary, compression pattern seem to align with the trabeculae within the growth plate. Combined with the observation that trabeculae are very thin, this could indicate that the region is acting as a shock absorber, allowing high deformation and preventing stresses from propagating in the bone. This assumption could be investigated in future works (see Chapter 5).

In addition, one can notice the highly dissimilar materials induce peak stresses located at the interface. This is investigated in subsection 4.3.3.

4.3.2 Region of interest

We chose to analyze stresses in the whole bone as well as in a region of interest closer to the insertion site, as shown in Figure 4.9. Figures 4.10a and 4.10b represent distribution of stresses when considering elements in the whole bone or restricted to the region of interest. Whether the boundary condition applied is a force or a displacement, one can notice that the insertion region is containing most of the high-stressed elements. This can clearly be noticed in the means and standard deviations reported in the captions of the corresponding figures. Therefore, and for an easier manipulation of data, our subsequent distributions will comprise only the elements of the regions of interest mentioned here above.

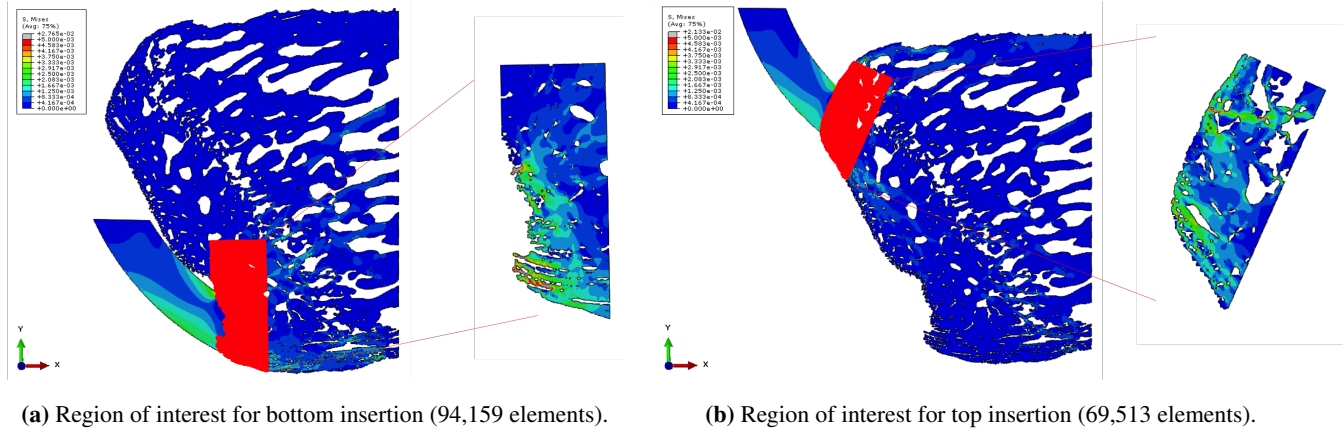


Figure 4.9: Illustration of the regions of interest from which stresses will be extracted.

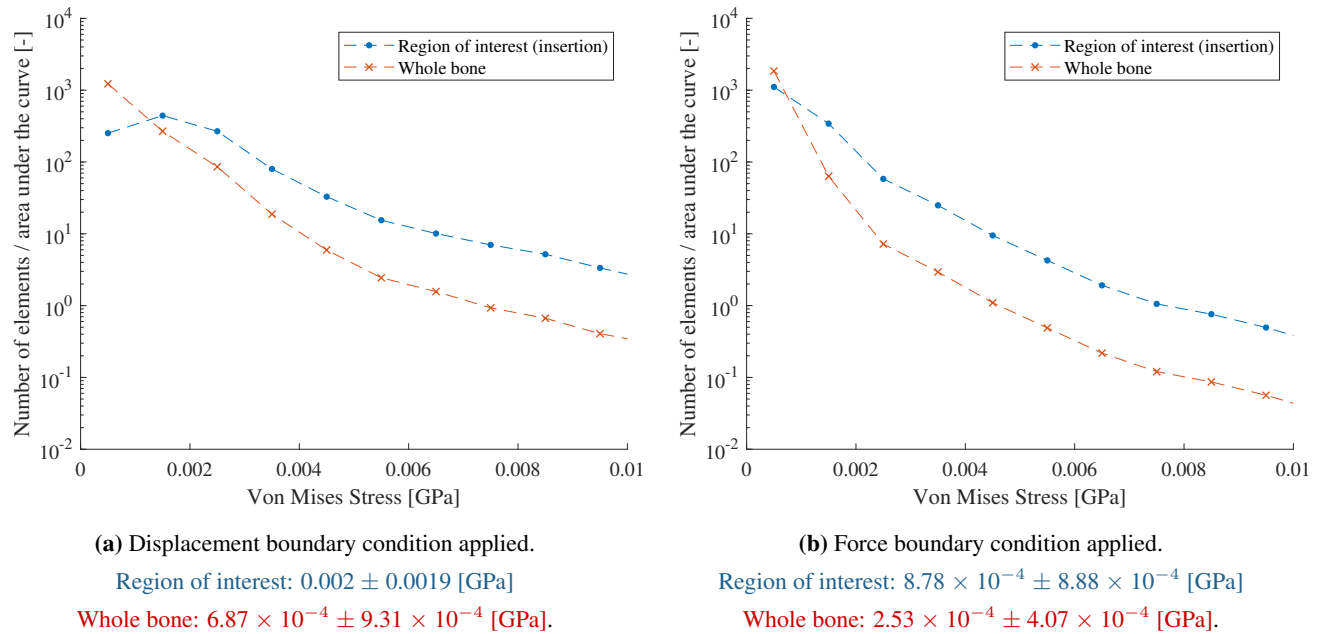


Figure 4.10: Comparison of Von Mises stresses distributions, as well as means and standard deviations (see caption) when those ones are extracted from the region of interest or from the whole bone, for the two types of boundary conditions.

4.3.3 Effect of material mismatch

Before going any further in our analysis, it is of interest to study one of the main feature of the insertion region: the material mismatch. Taking advantage of the possibilities brought by computer modeling, we can tune material parameters of the tendon to make it as rigid as bone: resulting stresses are illustrated in Figure 4.11b (with force boundary condition).

With a rigid tendon, one can notice that stresses evolve more smoothly from one part to the other. Indeed, peak stresses are extensively reduced at the insertion. This interestingly suggests that those high values were due to the materials mismatch more than to the interdigitations. Reduced stresses are noticeable in stresses distribution shown in Figure 4.12.

When the tendon is more rigid, stresses spread over a wider region of the bone and over a deeper area. This can be observed in the stress patterns from Abaqus. Moreover, this can be deduced from the means and standard deviations reported in the caption of Figure 4.12. Indeed, even though the "soft" tendon exhibits a higher mean, the difference with the mean of the "rigid" one is quite small (14 % decrease). It is also interesting to notice that a rigid tendon is leading to a reduced standard deviation of the stresses: this can be understood as an "homogenization" process due to the reduction of the peak stresses of the interface. Anyway, those observations may indicate that interdigitations are somehow adapted to the material mismatch by concentrating stresses at the interface and protecting therefore the rest of the bone.

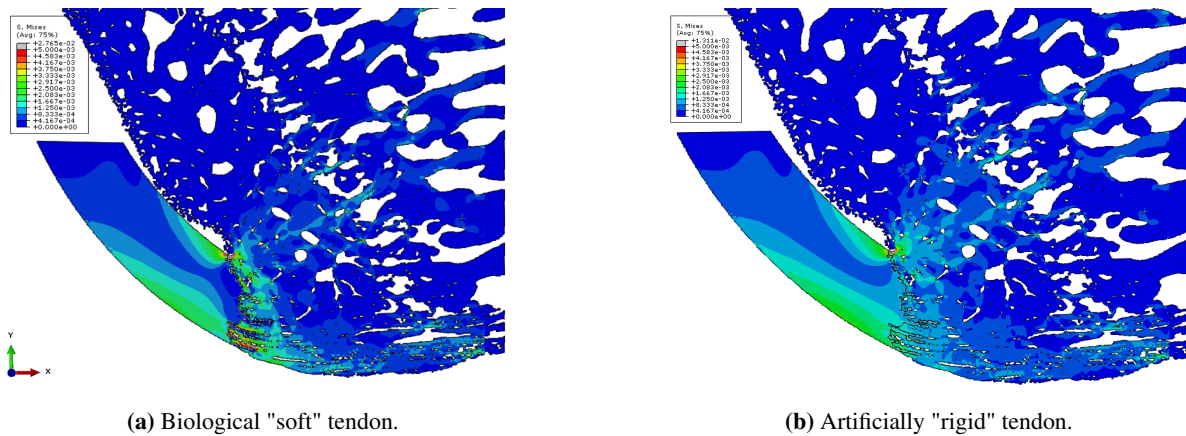


Figure 4.11: Zoom on the insertion region showing Von Mises stresses transmission from tendon to bone.

4.3.4 Influence of tendon length

??

In this subsection, we study the robustness of the model to variation of loading parameters. First, we investigate the effect of the tendon's length. This leads us to investigate how its orientation is affecting stresses as well. Stress patterns remain similar to the one observed earlier, therefore Abaqus figures may be found in Appendix G and only stresses distributions are depicted here.

► Arc length

First of all, tendons of varying length have been built (as been shown in Figure 4.3a in previous section). Stresses distributions are shown in Figure 4.14a and 4.14b, respectively considering a displacement and force boundary conditions. One can observe that behavior is the opposite in those two scenarios. How can we understand this?

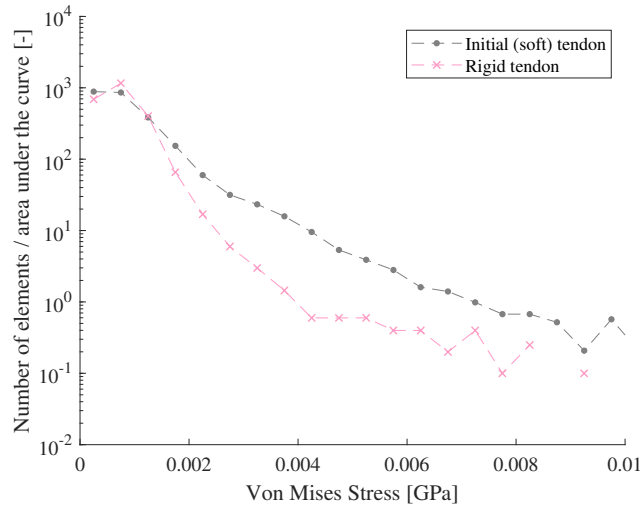


Figure 4.12: Comparison of Von Mises stresses distributions, as well as means and standard deviation (see) when the tendon is modelled as a rigid part or as a biologically soft one, force boundary condition applied.

Initial tendon: $8.78 \times 10^{-4} \pm 8.88 \times 10^{-4}$ [GPa]

Rigid tendon: $7.56 \times 10^{-4} \pm 4.53 \times 10^{-4}$ [GPa].

First of all, when applying a constant displacement over varying tendon length, it is plausible that we modify the apparent stiffness of the tendon. Indeed, stiffness is defined as the resistance provided by a system to deformation and is simply defined as:

$$F = k\Delta x, \quad (4.3)$$

with k related to the elastic modulus E through cross-sectional area A and length of the element L (as illustrated in Figure 4.13):

$$k = \frac{EA}{L} \quad (4.4)$$

Therefore decreasing the length of the tendon is indeed increasing its apparent stiffness, which in turns increases the force applied, as the displacement imposed is constant.

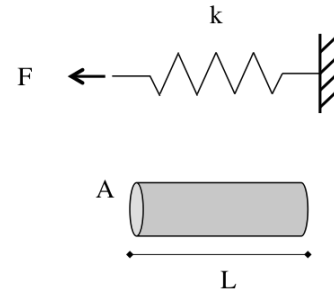


Figure 4.13: Spring analogy and representative parameters of an element.

This explains why stresses increase with the shortening of the tendon, and this is reflected by the means of the stresses (see caption of the corresponding figures).

On another hand, loading our model with a force reveals another mechanism: the effect of the lever arm. Indeed, decreasing the length of the tendon is directly decreasing the lever arm of the torque effectively applied at the insertion. Figure 4.14b shows the decrease of stresses with arc length in this case, and the mean values follow the same trend.

Those simulations allow us to observe that both displacement and force boundary conditions are sensitive to the length of the tendon. In order to investigate further the lever arm effect, we keep the arc length constant and run new simulations for varying orientations of the tendon.

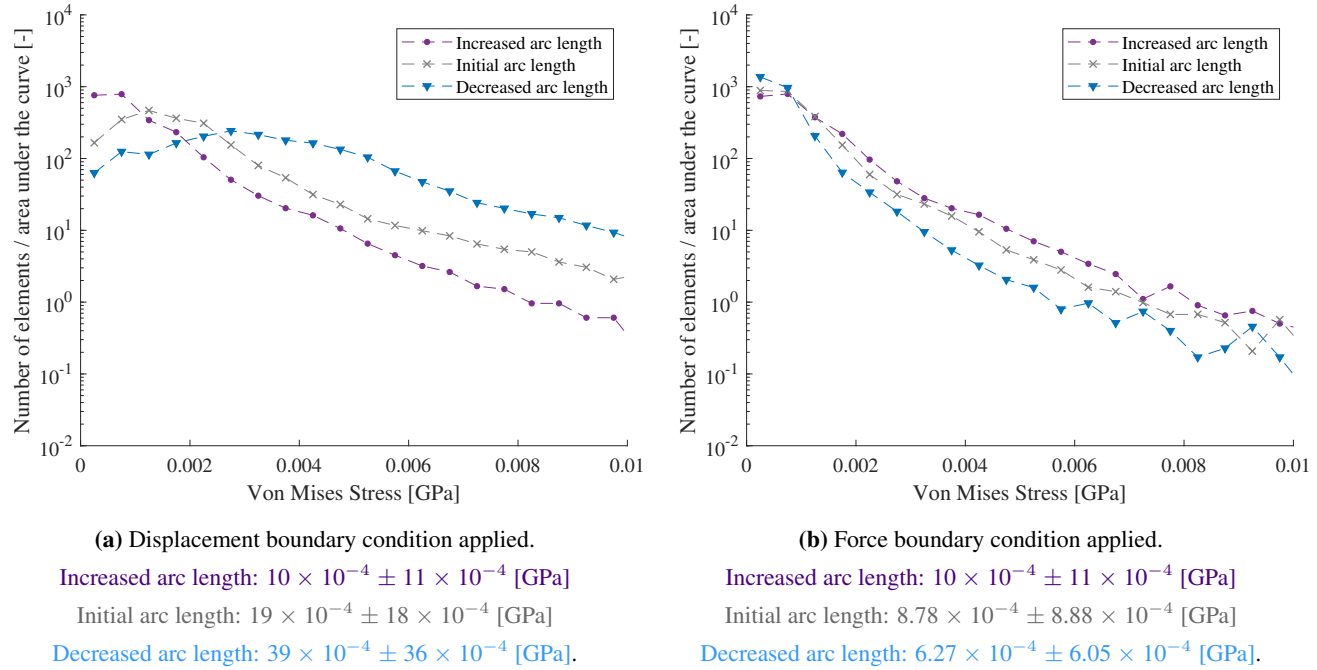


Figure 4.14: Comparison of Von Mises stresses distributions, as well as means and standard deviations (see caption) when arc length is varying, for the two types of boundary conditions.

► Orientation

We now study the robustness of the model towards changes in the orientation of the attached tendon. Applied load and displacement are still along the vertical axis. Geometries under investigation have been shown in Figure 4.3b. Stresses distributions, as well as means and standard deviations, are reported in Figures 4.15a and 4.15b.

It can be noticed that the effect is less clear than for arc length modification. However, one can see that the change in orientation (and therefore in lever arm) affects less the results when a displacement boundary condition is applied. This does make sense compared to what we have observed above: the displacement BC is influenced a lot by the arc length for apparent rigidity reasons. Here, the arc length being similar, differences are small. That being said, when a force is applied, we can observe increasing stresses when the orientation is increased, which also correspond to an augmentation of the lever arm.

In conclusion, considering a force applied to the tendon, one should be careful about lever arm effects because our model is exhibiting a high sensitivity with respect to that parameter.

4.3.5 Insertion location and robustness to force orientation

This subsection is presenting results of the "thought" experiment introduced at the beginning of this chapter. The idea is to simulate a wrong insertion and compare this one with the biological insertion site in terms of robustness to variations of force orientation. Absolute comparison between the two insertions should be avoided, for reasons similar to those mentioned in the previous section.

Figure 4.16 is illustrating Abaqus outputs for all the simulations under consideration. Orientation of the force is schematized by colored arrows and is basically rotated clockwise and anti-clockwise by an amount of 20° (keeping magnitude constant). Resulting Von Mises stresses are depicted in Figures 4.18a to 4.16f for each configuration.

First of all, it can be noticed that in both configurations, an anti-clockwise rotation of the force orientation is resulting in a global decrease of the stresses, and a clockwise rotation is resulting in opposite behavior. This can be understood by reasoning on an

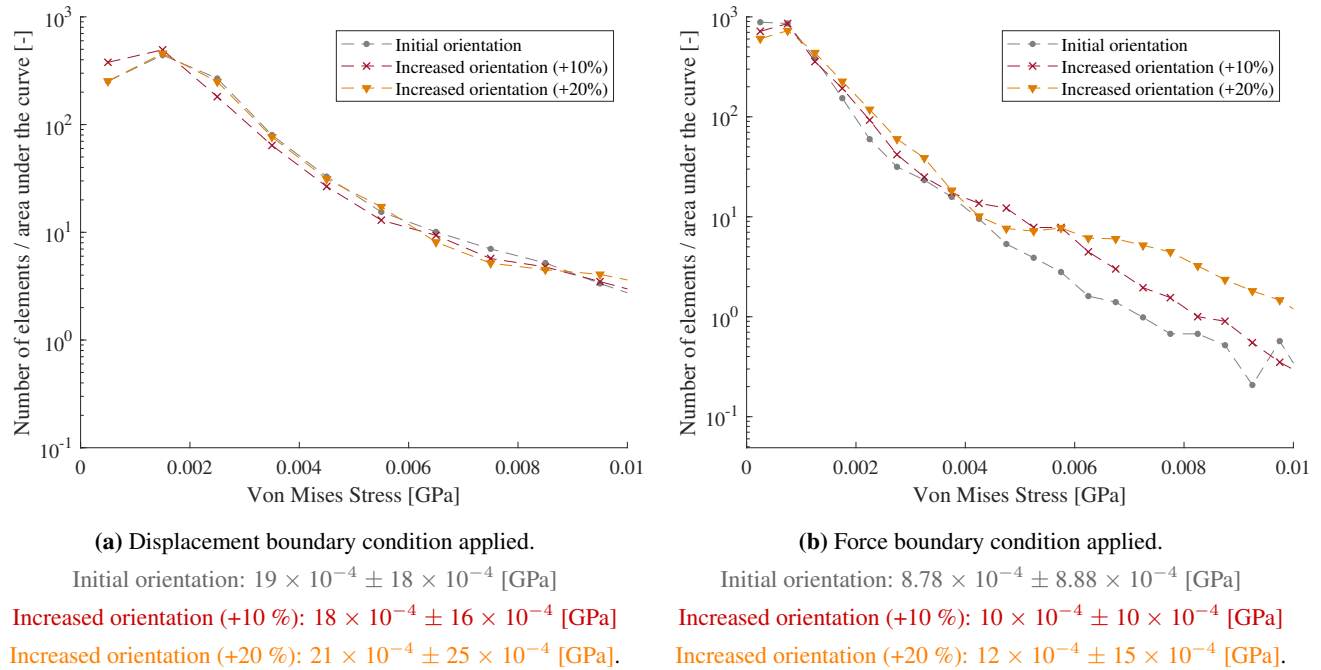


Figure 4.15: Comparison of Von Mises stresses distributions, as well as means and standard deviations (see caption) when orientation is varying, for the two types of boundary conditions.

simple model, as illustrated in Figure 4.17. Reference situation (Figure 4.17b) is generating tension and compression regions discussed in section 4.3.1. When the force is rotated anti-clockwise (Figure 4.17a), projections of the force in both directions is decreasing the net torque acting on the bone. The reverse situation is occurring for clockwise rotation of the force (the net torque is increased).

In addition, those results exhibit an interesting trend: whether considering Von Mises or principal stresses, the biological position of insertion is showing more robustness to changes in force orientation: that is, stresses evolution is less affected. This is confirmed by comparing means and standard deviations of stresses for each configuration, as illustrated in Table 4.2 for Von Mises stresses.

		Von Mises stresses [GPa]		
		Anti-clockwise rotation (+20°)	Initial orientation	Clockwise rotation (-20°)
BIOLOGICAL INSERTION	Mean stress and std	$5.87 \times 10^{-4} \pm 5.82 \times 10^{-4}$	$8.78 \times 10^{-4} \pm 8.88 \times 10^{-4}$	$11 \times 10^{-4} \pm 11 \times 10^{-4}$
	% of mean variation	- 33%	/	+ 25%
WRONG INSERTION	Mean stress and std	$4.53 \times 10^{-4} \pm 3.66 \times 10^{-4}$	$9.64 \times 10^{-4} \pm 7.46 \times 10^{-4}$	$14 \times 10^{-4} \pm 10 \times 10^{-4}$
	% of mean variation	-53%	/	+45%

Table 4.2: Evolution of mean and standard deviation of Von Mises stresses with the site of insertion and the force orientation.

We believe that this increased robustness at insertion site tends to exhibit an optimization mechanism of the bone structure.

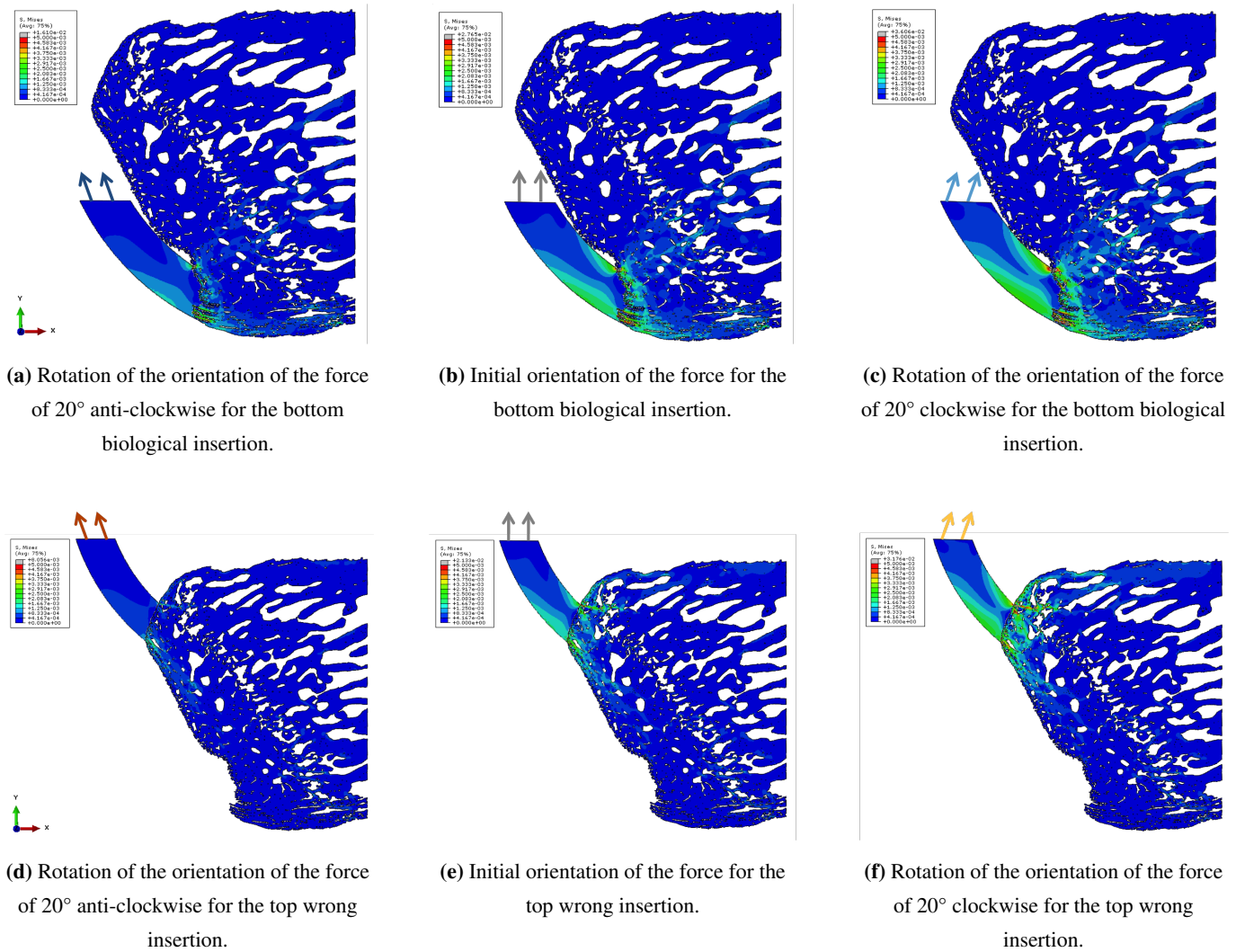


Figure 4.16: Output Von Mises stresses for a varying orientation of the force applied at the tendon extremity, for both insertion sites.

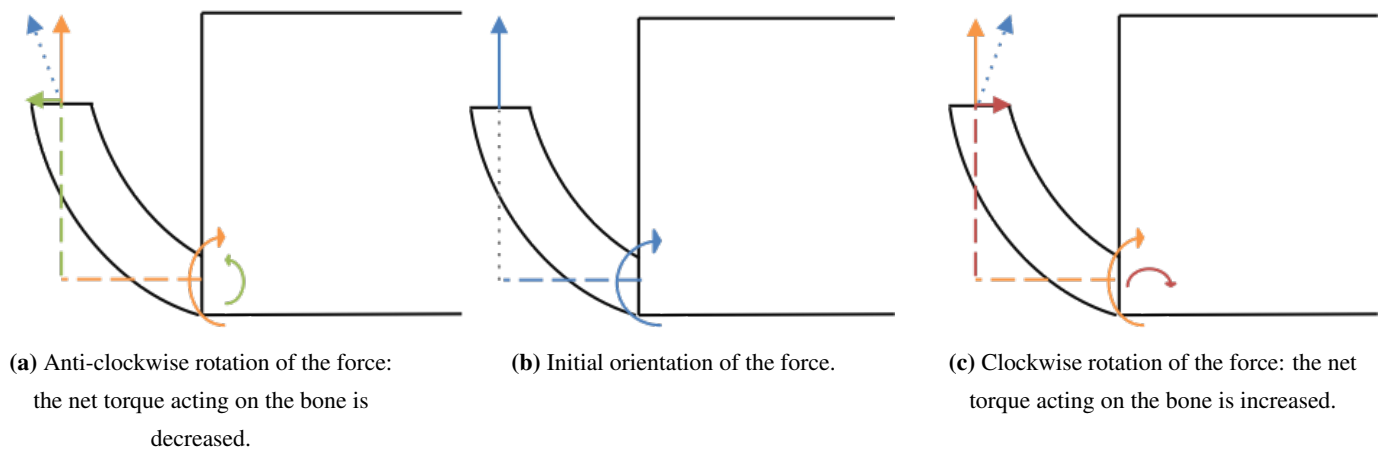


Figure 4.17: Oversimplified model illustrating the net torque acting on the bone at the insertion site as a function of the orientation of the loading applied.

Indeed, a change in the orientation of the loading sustained by the Achilles tendon is physiologically relevant considering the range of motion. Therefore, our results seem to indicate that bone morphology has been adapted in order to tolerate those changes, whereas a wrong insertion is not able to do so. This robustness may arise from bone roughness, as well as from global bone architecture beneath insertion. Increased anisotropy at the insertion do not enable us to expect such a behavior. Indeed, isotropic structures are better at dealing with a high variation in loading orientation. This suggests that other mechanisms provide this robustness. Our results from structural analysis taught us that porosity was evolving in a more controlled manner from the insertion point than from another point that was exactly at the position of the wrong insertion considered here. It could be that this evolution of porosity is directing the propagation of stresses. It could also be that the interdigitations reported at the insertion are part of a global adaptation strategy including resistance to loading changes.

4.4 Discussion and conclusions

In this section, we put the results of our biomechanical analysis into perspective and draw the main conclusions of this part of the thesis.

First of all, this study has been conducted on only one slice. More than being specimen-dependent, our results could therefore be slice-dependent. However, our assumption is that biomechanical behavior of bone is dependent on its morphology, and specifically on the parameters investigated in the first part of this thesis. Therefore, as those parameters have shown significantly similar tendencies from one slice to another, we can expect our findings to be consistent over different slices.

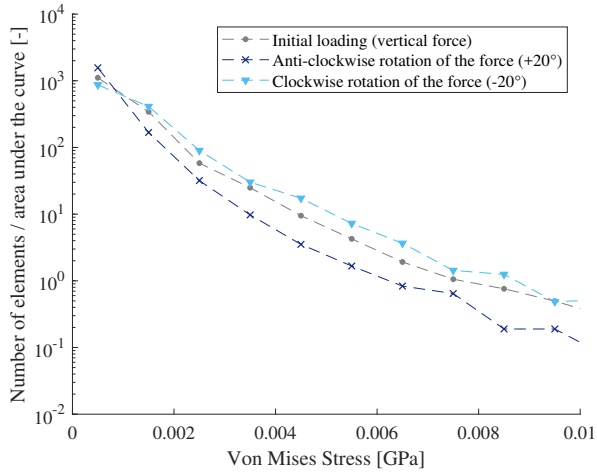
Regarding the geometry, one can of course discuss the biological realism of the tendon. First, geometry has been simplified. In addition, the insertion has been limited to a small region. Indeed, the modelling of the complete enthesis organ would require to represent the periosteum fibrocartilage. However, a tie constraint between tendon and cartilage would not be consistent in that case because this cartilaginous region is specifically supposed to allow the sliding of the tendon.

Our model can also be questioned in terms of material definitions. Indeed, both tendon and bone have been simplified a lot. However, none of our results consist in looking at the absolute value of output stresses. Rather, comparisons highlighting interesting behaviors are drawn.

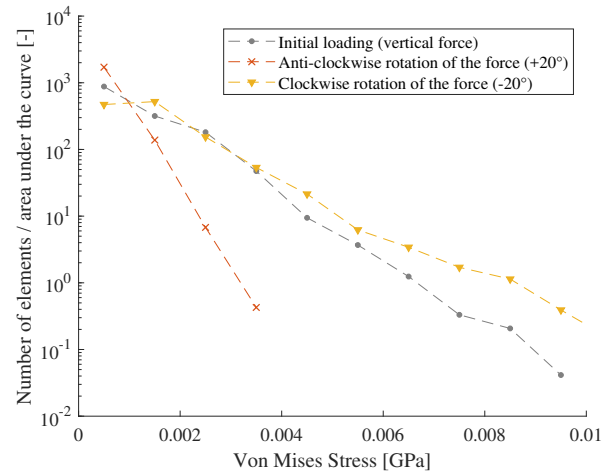
In addition to the accuracy of materials' definition in themselves, the spatial variation of Young's Modulus can be questioned. Indeed, as introduced in subsection 1.2.4, the interface region has been shown to exhibit an evolution in the properties from tendon to bone [41] that has not been modeled. However, our model provides a general framework that could be exploited to introduce such heterogeneity.

Keeping those limitations in mind, our model allow us to draw the following conclusions:

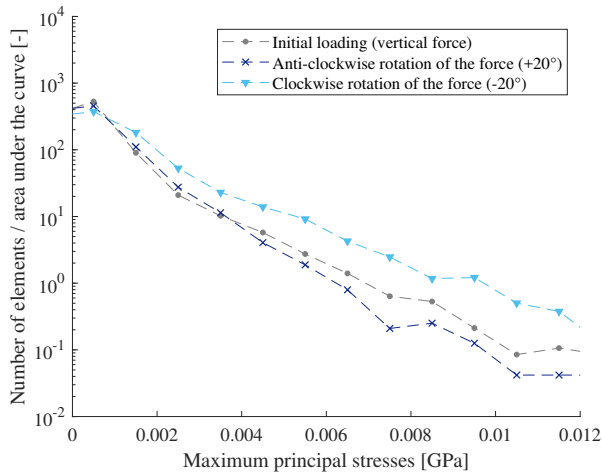
- Transmission of stresses from the Achilles tendon to the calcaneus results in a non-trivial pattern, generating compression regions aligned with growth plate's trabeculae and tension regions perpendicular to those ones.
- The material mismatch between parts of our model is generating high stresses at the interface, but more concentrated on that region, than it is the case when no mismatch is assumed.
- The biological insertion region shows more robustness towards modification of the loading's orientation of the tendon, than another wrong insertion region at the top of the bone.



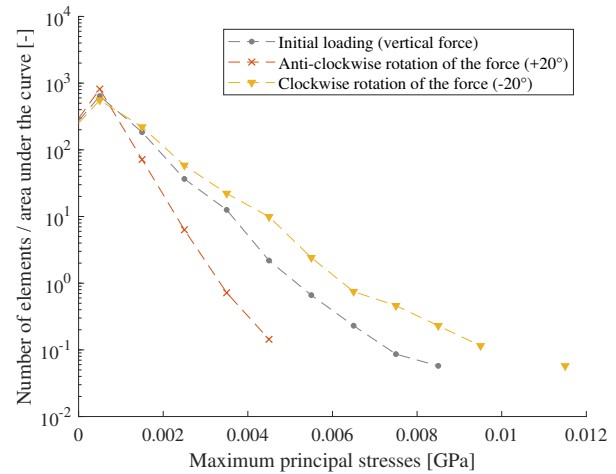
(a) Von Mises stresses distributions for the bottom biological insertion.



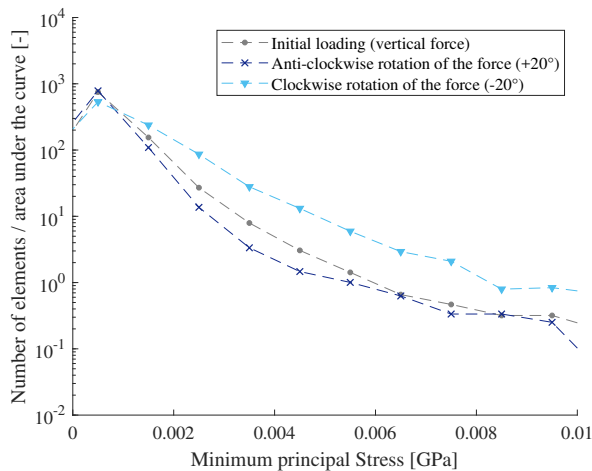
(b) Von Mises stresses distributions for the top wrong insertion.



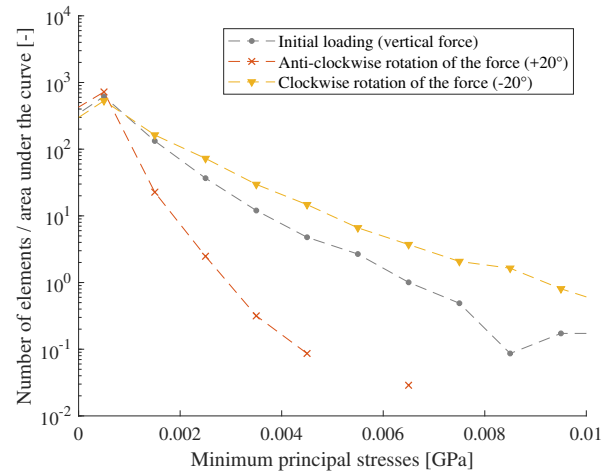
(c) Maximum principal stresses distributions for the bottom biological insertion.



(d) Maximum principal stresses distributions for the top wrong insertion.



(e) Minimum principal stresses distributions for the bottom biological insertion.



(f) Minimum principal stresses distributions for the top wrong insertion.

Figure 4.18: Comparison of stresses distributions when orientation of the force applied is varying, for both regions of insertion.

Chapter 5

Perspectives

This concluding chapter aims at summarizing the main limitations of our work, and, based on this, at proposing perspectives for future work.

5.1 Limitations

To start with, one can argue that a weak point of our analysis is the use of animal samples instead of human ones. However, as already said, bony architecture of rats is very similar to that of humans and rats have been proven to be appropriate for the study of tendons pathologies. That being said, it must be kept in mind that our findings are only indicative for rats and ideally our analysis should be extended to human data or at least to bigger animals.

Probably the main limitation of our study lies in the reduced number of specimens investigated. Indeed, we are well aware that findings based on two samples do not show enough reproducibility to be considered as general truth. However, regarding structural analysis, the repeatability of our conclusions on several slices and on two specimens is already promising. Conclusions from our biomechanical analysis are obviously less powerful, as they have been drawn from one slice of one specimen. However, the hypothesis that biomechanical behavior is dictated by architecture enables us to assume that our findings should be consistent from one slice to another.

Two dimensions models are generally promoted for their reduced computational cost and easier handling. In our case, this choice has allowed us to develop a high accuracy micro-finite element model with an element size equal to the voxel size, using commercial solvers and standard workstations. It is obvious that reaching such a precision with a 3D model would have required dedicated parallel solvers as well as supercomputers. Despite that fact, 3D model are of course more biologically realistic. That being said, as we have shown in section 1.1.4, the most used ankle motions are dorsiflexion and plantarflexion. Those ones consist in the rotation around the ankle joint in the sagittal plane, which is the reason why this plane has been investigated. Moreover, whenever investigating an uncovered area as it was the case in this thesis, it appears appropriate to start with an examination of 2D behavior. Considering our results, extension to 3D model would be highly instructive.

Another debatable point of our approach refers to the lack of control over the status of the rats. Indeed, no information (such as gender, health or age) was available. Knowing how those factors (and specifically age and health) can affect bone morphology, it would have been more appropriate to be able to put our results in perspective with the rat status.

Regarding the methods followed, specific limitations of our investigations have already been discussed in details in sections 3.5 and 4.4.

5.2 Future work

As it covers a research area that has not been explored before, this project is clearly opening the way towards further investigations. In this section, we present the future steps that should be followed to enhance the impact of our conclusions, as well as possible extensions inspired from our findings.

5.2.1 Improvements of the current model

Our model could be exploited in order to further explore other research questions raised during this work.

First of all, the potential shock absorption role of the growth plate could be examined. To do so, we should first delineate a new region of interest focusing only on the growth plate, as shown in Figure 5.1. Afterwards, we could assess the amount of compressive deformation absorbed. In order to highlight a potential damping in that region, we could also artificially fill the pores of the bone in order to check whether this leads to a reduced deformation but increase strains in the surrounding regions. This would suggest that the growth plate is somehow protecting bone by preventing it from undergoing excessive strains.

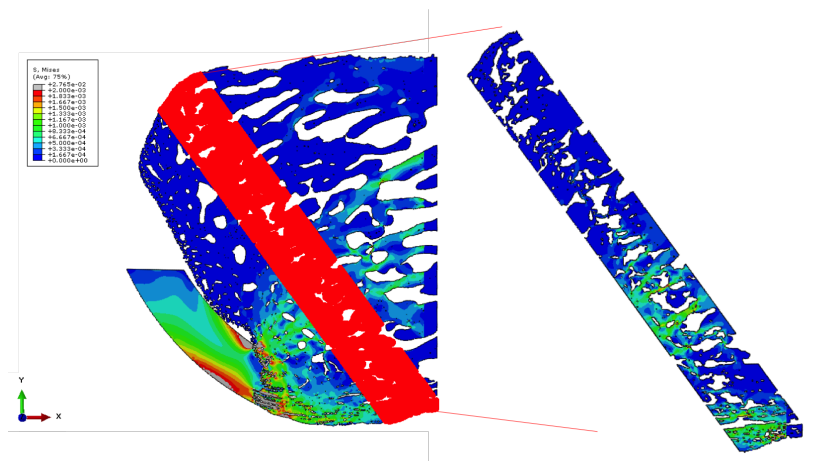


Figure 5.1: Illustration of the delineation of new region of interest focusing on the growth plate.

Secondly, roughness analysis has taught us that the region of the bone where periosteal fibrocartilage is anchoring was exhibiting significantly more rugosity than a non-loaded region of the bone. It would therefore be interesting to model this region, as well as to be able to represent the sliding of the tendon on the cartilage.

In addition, our analysis has shown the feasibility of a "line-of-force" between the insertion of the Achilles tendon and the plantar fascia. It would therefore be interesting and appropriate to add a boundary condition at that location that would represent the potential loading of the fascia. However, as we have seen with specimen 2 (see Appendix C), the two insertions might not lie in the exact same plane. This improvement would therefore be more suitable in a 3D model.

Finally, an interesting extension would be to better understand which one of the impacting parameter is more likely to provide the robustness observed at the biological insertion site. This could be done by first artificially smoothen the surface of the bone at the insertion, in order to see the impact of bone structure alone, without the roughness acting as a confounding factor. Besides, in order to evaluate the roughness effect, one could manually fill in the bone pores while keeping the roughness intact. Those two analyses should hopefully permit us to deduce which factor has the highest influence on the stress pattern and the robustness to force orientation variation.

5.2.2 Extensions of the current model

In this subsection, we finally describe the novel analyses (that would require a whole new procedure in terms of experimental data collection and model development) triggered by our findings.

First of all, one of the first ideas that aroused from our preliminary observations of the μ CT images was related to the potential imaging of the Achilles tendon. That being said, obtaining soft tissue contrast in μ CT images is not straightforward.

A first option would be to apply iodine staining on the tendon prior to the scanning process. Another possibility is to inject a contrast agent [91]. This would allow to see more precisely the insertion region of the tendon.

However, both of the techniques mentioned above add cost and complexity to the process. It would be preferable to use phase contrast μ CT, which allows to achieve soft tissue contrast based on intrinsic contrast rather than external agents. This type of scanner would allow us to reach high contrast between bone and tendon and therefore to locate precisely the insertion site, as well as, hopefully, interesting features of the tendinous side of the insertion.

Moreover, all the steps covered in this thesis could be replicated for a three dimensions analysis, if new tools enabling to adapt our procedures are developed. For example, the step of delineation of the volumes of interest should be conducted carefully to be sure to contain only bone. It is obviously more delicate to ensure that condition on a volume than on a section. In order to characterize volume behavior, one could also exploit the functions of the `BoneJ` toolbox of `ImageJ` [31]. Those ones allow to characterize, among others, anisotropy, connectivity or trabeculae thickness. However, the negative side of those "automated" computations is that they provide less control over the outputs.

Upgrading our `Abaqus` model to the third dimension would require a huge number of elements if element size is kept at 2.5 [μ m]. It should therefore be considered to increase it globally or, preferentially, to apply a gradient in the element size from the insertion to the central part of the bone. Indeed, only the insertion requires a high accuracy in order to reproduce the roughness of the bone surface. Another option would be to use dedicated large-scale solvers.

In conclusion, it would be feasible, but definitely more delicate, to raise this thesis to the third dimension.

An instructive approach would also consists in the application of our characterization procedure to a diseased enthesis. Indeed, this would allow us to compare between diseased and healthy cases in order to highlight the features lost in the diseased condition. However, this would require not only the extraction of new specimens, but also the induction of the degeneration of the enthesis in those ones using irradiation or overusage. This new project would allow us to give a new and informative insight into entheses disease progression that might be useful for therapeutic options.

Finally, the ultimate objective of any kind of animal-based model such as ours is to be able to export the findings up to the human scale. Although the collection of experimental data would be obviously more delicate, if our conclusions are confirmed by a 3D analysis, and if this model allow us to draw informative comparison between diseased and healthy rats entheses, it would be definitely interesting to find a way to apply our methods to human samples.

Conclusion

The aim of this master thesis was to better understand of mechanisms allowing interfacial regions, connecting soft tissue to bone, to reach their efficiency. A novel approach has been proposed, consisting in investigating enthesis behavior through the analysis of the structure and biomechanics of bone beneath the insertion. Our objective was to demonstrate that this region plays a pivotal role for facilitating the force transmission from tendon to bone.

First, we have been indeed able to highlight evidence of bone adaptation at different length scale. Our findings reveal the following:

- First, porosity is gradually increasing from the insertion site to the inner region of the bone. The investigation of the coefficient of determination characterizing the evolution of porosity with distance has shown that this gradual increase seems to be more controlled than when considering another location on the bone surface far from the insertion point.
- Second, the computation of bone micro-architecture orientation taught us that the insertion region shows significantly more anisotropy than the rest of the bone. This alignment is supposed to assist the transmission of the loading coming from the tendon.
- Finally, comparison of roughness parameters at several locations of the bone surface has revealed that the insertion is characterized by a significantly higher roughness. A higher surface roughness is known to increase the toughness of bimaterial interfaces.

Second, we have reinforced those results by studying biomechanical implications of our analysis, using a microstructural finite element model of the Achilles tendon and bone. This has allowed us to draw the subsequent conclusions:

- First, the loading of the tendon tied to the bone at the interface results in a the transmission of the stresses exhibiting a non-trivial pattern within the bone. Indeed, it generates compression regions aligned with the trabeculae of the growth plate, and tension regions perpendicular to those ones. Tension regions are also found to be aligned with the micro-architecture located directly beneath the insertion, corroborating assumptions of a "line-of-force" between Achilles tendon insertion and the insertion of the plantar fascia at the bottom of the foot.
- Second, the artificial stiffening of the tendon has enabled us to conclude that the original material mismatch generates high, but localized, stresses at the interface.
- Third, a "though" experiment has been conducted and consisted in comparing the behavior at the biological insertion with a "wrong" insertion located at the top of the bone. To do so, the orientation of the force has been rotated clockwise and anti-clockwise. We have shown that the biological insertion is robust towards changes in the orientation of the force that may occur during the physiological range of motion.

This project proposes a consistent framework for studying bone adaptation towards the insertion of the tendon and the limitations of the study have been clearly specified. Based on our work, we proposed some improvements to increase the impact of our findings. The results of our analysis trigger new research questions and perspectives for future work in order to fully understand where the efficiency of one of the greatest interfacial mismatches found in nature arises from.

Appendices

Appendix A: Technical details about SkyScan-1272

Specifications

X-ray source	20-100 [kV],10 [W],<5 [μm] spot size @ 4 [W]
X-ray detector	16 [Mp] or 11 [Mp], 14-bit cooled CCD fiber-optically coupled to scintillator
Maximum object size	75 [mm] in diameter using offset scan (27 [mm] in fast single scan)
Detail detectability	0.35 [μm] (16 [Mp]) or 0.45 [um] (11 [Mp]) at highest magnification
Reconstruction	single PC or cluster multithreaded CPU/GPU 3D reconstruction
Optional stages	cooling, heating, compression / tension
Radiation safety	<1 [μSv/h] at 10 [cm] from the instrument surface<1 [μSv/h] at 10 [cm] from the instrument surface

Table 5.1: Technical data sheet of SkyScan-1272 [19].

System dimensions

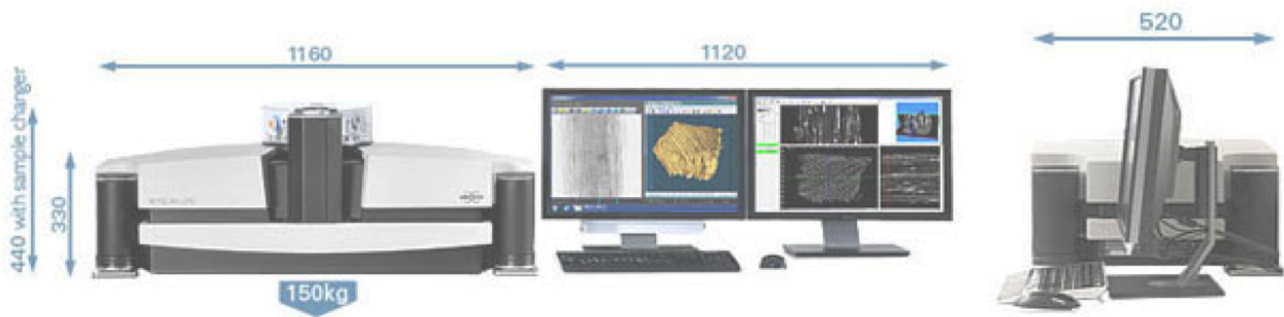


Figure 5.2: Pictures and dimensions of the SkyScan-1272 complete system.

Appendix B: Complete data of the image acquisition

Acquisition		Reconstruction	
<i>Parameter</i>	<i>Value</i>	<i>Parameter</i>	<i>Value</i>
Filename Index Length	8	Reconstruction Program	NRecon
Number Of Files	633	Program Version	Version: 1.7.0.4
Number Of Rows	1344	Reconstruction engine	InstaRecon
Number Of Columns	2016	Engine version	Version: 2.0.3.7
Partial Width	OFF	Reconstruction from batch	Yes
Image crop origin X	0	Postalignment	-1
Image crop origin Y	0	Reconstruction servers	SCAN1272_099
Camera binning	2x2	Time and Date	Dec14,2017 16:43:13
Image Rotation	0.074	First Section	54
Optical Axis (line)	672	Last Section	1112
Camera to Source (mm)	221.87562	Reconstruction duration per slice (s)	0.062323
Object to Source (mm)	61.63150	Total reconstruction time (s)	66
Source Voltage (kV)	80	Section to Section Step	1
Source Current (uA)	124	Section Count	1059
Image voxel Size (um)	4.99995	Result File Type	JPG
Scaled Image voxel Size (um)	4.99995	Result File Header Length (bytes)	Compressed JPG format(100%)
Image Format	TIFF	Result Image With (voxels)	2016
Depth (bits)	16	Result Image Height (voxels)	2016
Reference Intensity	57000	voxel Size (um)	4.99995
Exposure (ms)	1700	Reconstruction Angular Range (deg)	189.9
Rotation Step (deg)	0.3	Use 180+	Off

Acquisition		Reconstruction	
<i>Parameter</i>	<i>Value</i>	<i>Parameter</i>	<i>Value</i>
Use 360 Rotation	NO	Angular Step (deg)	0.3
Scanning position (mm)	5.385	Smoothing	1
Frame Averaging	ON (4)	Smoothing kernel	2 (Gaussian)
Random Movement	OFF (30)	Ring Artifact Correction	18
Flat Field Correction	ON	Draw Scales	OFF
FF updating interval	211	Object Bigger than FOV	OFF
Geometrical Correction	ON	Reconstruction from ROI	OFF
Filter	Al 0.5 mm	Filter cutoff relative to Nyquist freq	100
Gantry direction	CC	Filter type	0
Rotation Direction	CC	Filter type description	Hamming (Alpha=0.54)
Type of Detector Motion	STEP AND SHOOT	Undersampling factor	1
Scanning Trajectory	ROUND	Threshold for detect voxel mask (%)	0
Number of hor. Offset Positions	1	Beam Hardening Correction (%)	80
Study Date and Time	14 Dec 2017 16h35	CS Static Rotation (deg)	0
Scan duration	1h:23m:34s	Minimum for CS to Image Conversion	0.004084
Maximum vertical TS	5	Maximum for CS to Image Conversion	0.097986
		HU Calibration	OFF
		BMP LUT	0
		Cone-beam Angle Horiz.(deg)	9.349983
		Cone-beam Angle Vert.(deg)	6.241014
		Pseudo-parallel projection calculated	1

Table 5.2: Key parameters of the μ CT scan acquisition for specimen 1

Acquisition		Reconstruction	
<i>Parameter</i>	<i>Value</i>	<i>Parameter</i>	<i>Value</i>
Filename Index Length	8	Reconstruction Program	NRecon
Number Of Files	949	Program Version	Version: 1.7.0.4
Number Of Rows	2688	Reconstruction engine	InstaRecon
Number Of Columns	4032	Engine version	Version: 2.0.3.7
Partial Width	OFF	Reconstruction from batch	Yes
Image crop origin X	0	Postalignment	0
Image crop origin Y	0	Reconstruction servers	SCAN1272_099
Camera binning	1x1	Time and Date	Dec15,2017 11:20:07
Image Rotation	0.074	First Section	109
Optical Axis (line)	1344	Last Section	2578
Camera to Source (mm)	221.87562	Reconstruction duration per slice (seconds)	0.257490
Object to Source (mm)	61.63150	Total reconstruction time(s)	636
Source Voltage (kV)	80	Section to Section Step	1
Source Current (uA)	124	Section Count	2470
Image voxel Size (um)	2.499975	Result File Type	JPG
Scaled Image voxel Size (um)	2.499975	Result File Header Length (bytes)	Compressed JPG format(100%)
Image Format	TIFF	Result Image With (voxels)	4032
Depth (bits)	16	Result Image Height (voxels)	4032
Reference Intensity	57000	voxel Size (um)	2.49997
Exposure (ms)	3000	Reconstruction Angular Range (deg)	189.9
Rotation Step (deg)	0.2	Use 180+	Off

Acquisition		Reconstruction	
<i>Parameter</i>	<i>Value</i>	<i>Parameter</i>	<i>Value</i>
Use 360 Rotation	NO	Angular Step (deg)	0.2
Scanning position (mm)	8.049	Smoothing	1
Frame Averaging	ON (4)	Smoothing kernel	2 (Gaussian)
Random Movement	OFF (30)	Ring Artifact Correction	9
Flat Field Correction	ON	Draw Scales	OFF
FF updating interval	158	Object Bigger than FOV	OFF
Geometrical Correction	ON	Reconstruction from ROI	OFF
Filter	Al 0.5 mm	Filter cutoff relative to Nyquist frequency	100
Gantry direction	CC	Filter type	0
Rotation Direction	CC	Filter type description	Hamming (Alpha=0.54)
Type of Detector Motion	STEP AND SHOOT	Undersampling factor	1
Scanning Trajectory	ROUND	Treshold for detect voxel mask (%)	0
Number of hor. Offset Positions	1	Beam Hardening Correction (%)	80
Study Date and Time	14 Dec 2017 20h39	CS Static Rotation (deg)	0
Scan duration	3h:37m:14s	Minimum for CS to Image Conversion	0.003898
Maximum vertical TS	5	Maximum for CS to Image Conversion	0.104563
		HU Calibration	OFF
		BMP LUT	0
		Cone-beam Angle Horiz.(deg)	9.349983
		Cone-beam Angle Vert.(deg)	6.241014

Table 5.3: Key parameters of the μ CT scan acquisition for specimen 2

Appendix C: Plantar fascia insertion site in specimen 2

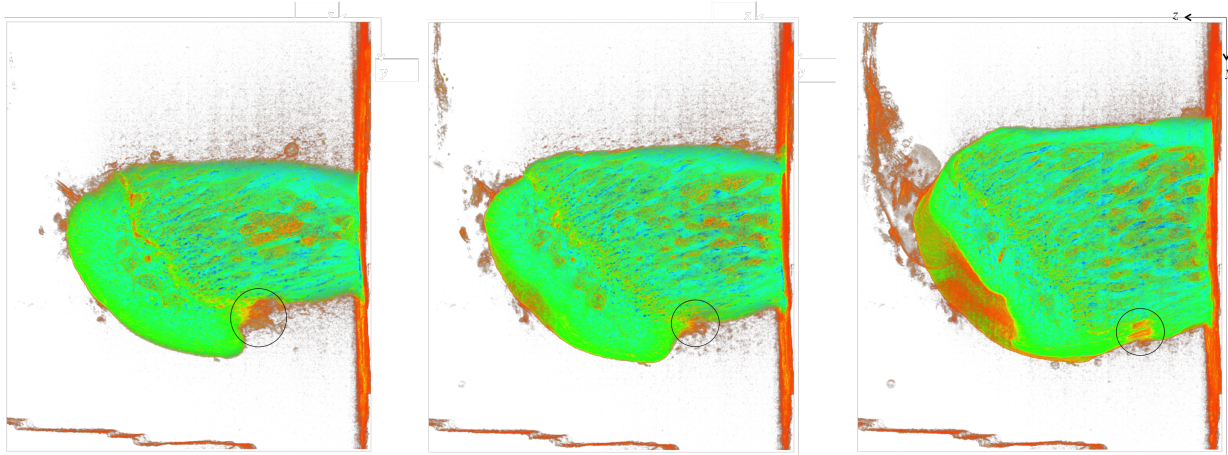


Figure 5.3: Additional spectral LUT $y - z$ slices of specimen 2 investigating the location of the plantar fascia insertion site (circled in black) at several depths along the x -axis.

Appendix D: Source image for the computation of osteocyte lacunae and vascular porosity

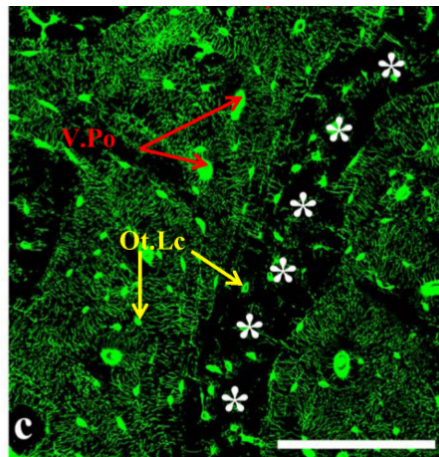
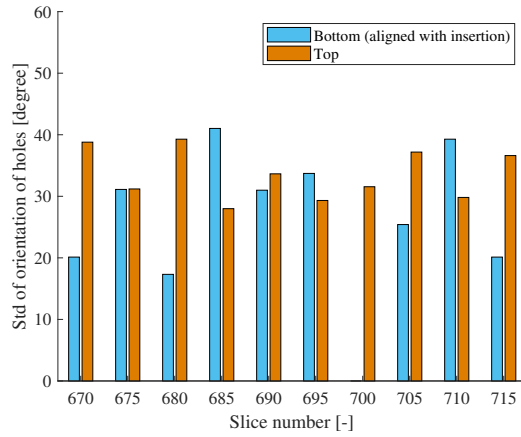
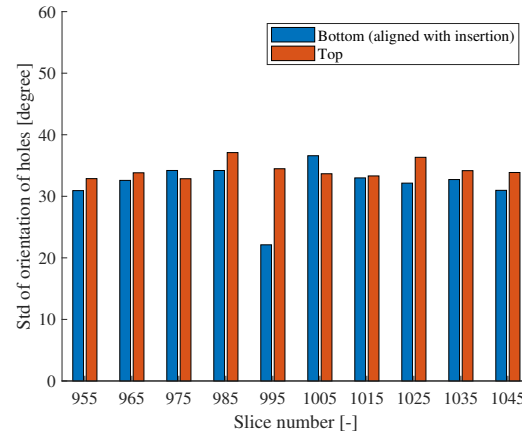


Figure 5.4: Reconstructed section from the metaphysis of the rat tibia stained with FITC (fluorescein isothiocyanate) [25]. ImageJ measurements of osteocyte lacunae and vascular porosity diameter give respectively 2.6 ± 0.5 and 5.7 ± 0.9 [μm]

Appendix E: Additional figures related to orientation analysis



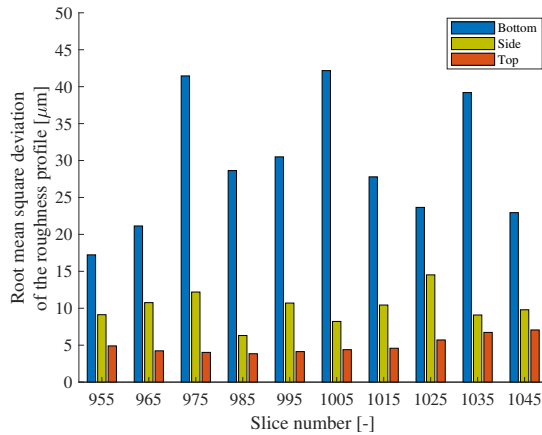
(a) Comparison of the standard deviations of the orientation of the pores in top and bottom regions (specimen 1). $P = 0.1733$



(b) Comparison of the standard deviations of the orientation of the pores in top and bottom regions (specimen 2). $P = 0.064$

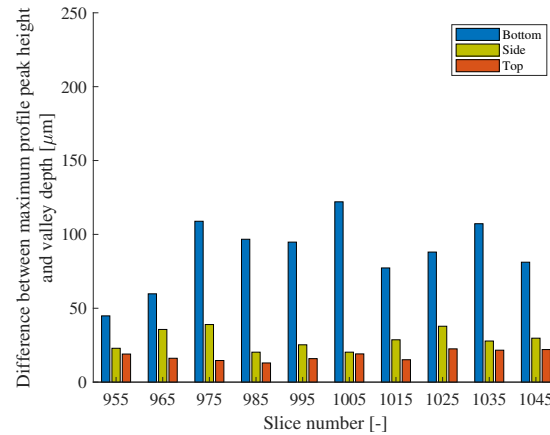
Figure 5.5: Additional results of the orientation analysis (standard deviation of the holes angles) over the 10 slices of interest for both specimens, for pores smaller than 20 μm

Appendix F: Additional figures related to roughness analysis



(a) Comparison of P_q values for the three regions of interest (bottom, side and top).

$P < 0.001$ (*) between each subgroups.

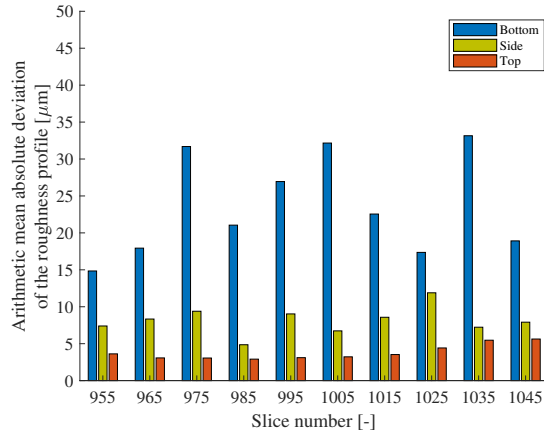


(b) Comparison of P_T values for the three regions of interest (bottom, side and top).

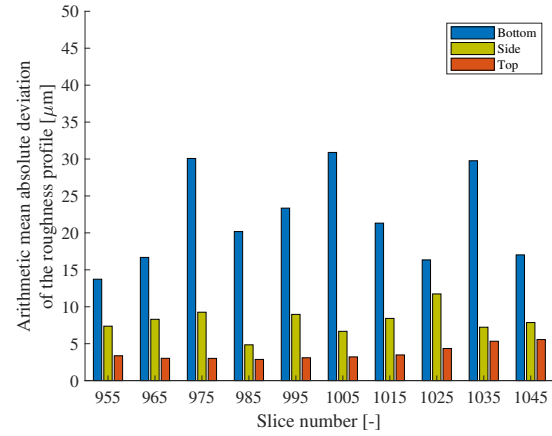
$P < 0.001$ (*) between each subgroups.

Figure 5.6: Results of the roughness analysis (P_q and P_T parameters) over the 10 slices of interest for specimen 2, computed using minimum distance instead of vertical distance.

The calculation of P_q is almost not affected. P_T values are much smaller has only positive values are computed. Indeed, the valley depth P_V is not a negative value but simply the smallest computed distance: P_T is thus almost equal to P_P .



(a) Comparison of P_a values for the three regions of interest (bottom, side and top), computed using vertical distance.
 $P < 0.001$ (*) between each subgroups.



(b) Comparison of P_a values for the three regions of interest (bottom, side and top), computed using minimum distance.
 $P < 0.001$ (*) between each subgroups.

Figure 5.7: Results of the roughness analysis for both method of distance's computation, over the 10 slices of interest. The values of P_a are almost not affected.

Appendix G: Additional figures related to the tendon length sensitivity analysis

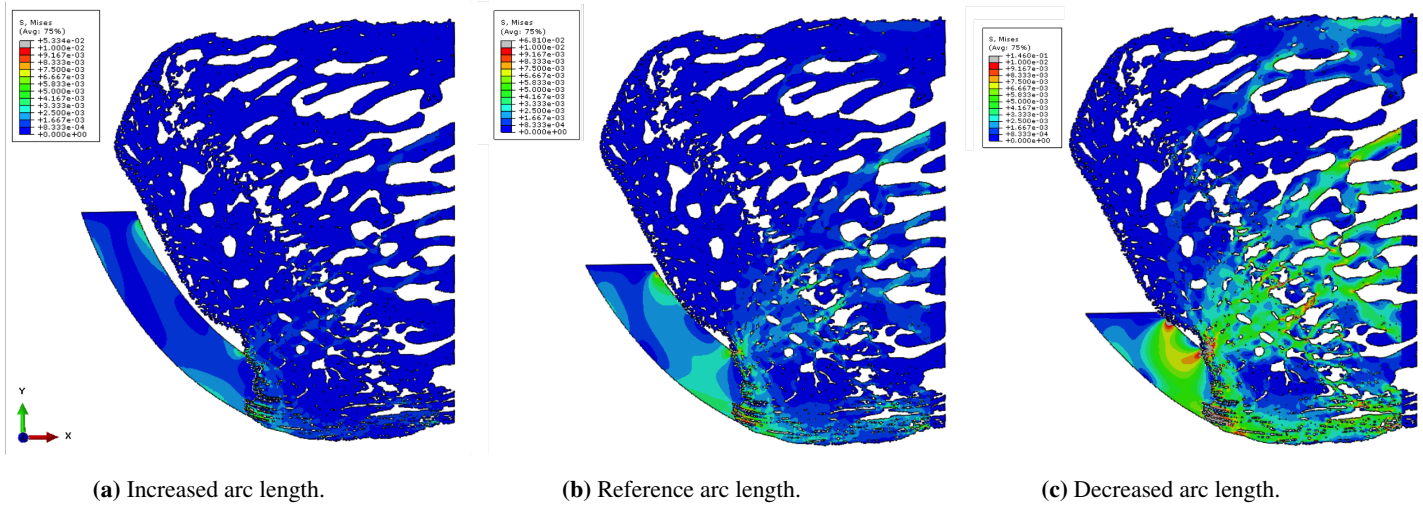


Figure 5.8: Output Von Mises stresses when changing the arc length of the tendon (displacement boundary condition).

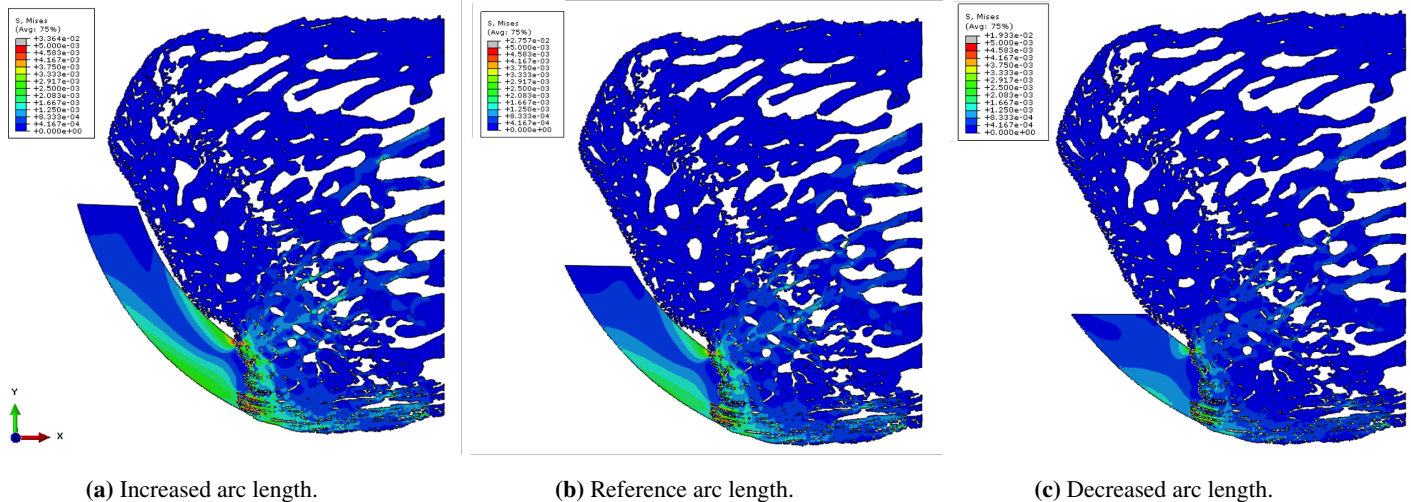


Figure 5.9: Output Von Mises stresses when changing the arc length of the tendon (force boundary condition).

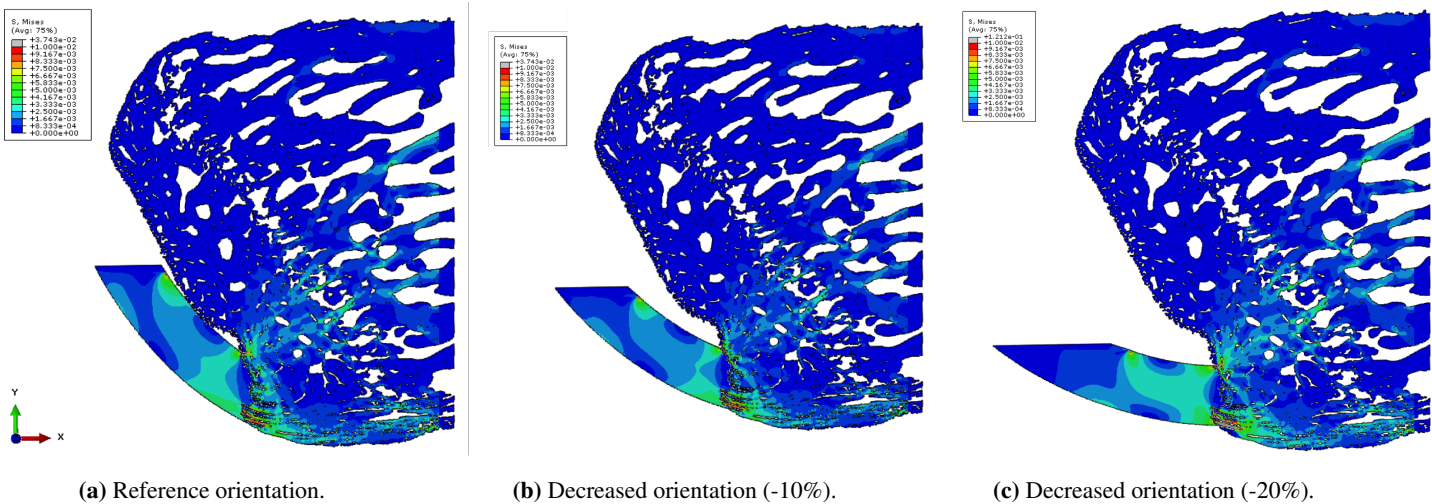


Figure 5.10: Output Von Mises stresses when changing the orientation of the tendon (displacement boundary condition).

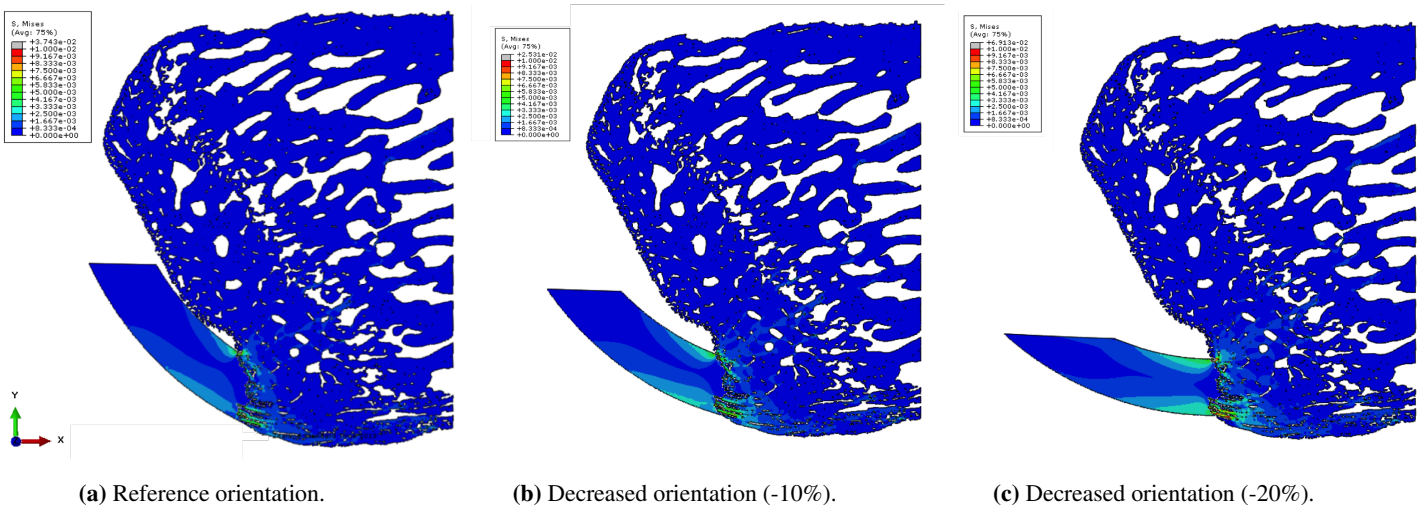


Figure 5.11: Output Von Mises stresses when changing the orientation of the tendon (force boundary condition).

Bibliography

- [1] H. ABDELBAKI, *Anterior cruciate ligament injury*, <http://hip-knee.com/en/knee/knee-injuries/anterior-cruciate-ligament-injury>, (Last access on 2018-05-23).
- [2] A. C. ABRAHAM AND T. L. H. DONAHUE, *From meniscus to bone: A quantitative evaluation of structure and function of the human meniscal attachments*, *Acta Biomaterialia*, 9 (2013), pp. 6322–6329.
- [3] M. AKHTER, J. LAPPE, K. DAVIES, AND R. RECKER, *Transmenopausal changes in the trabecular bone structure*, *Bone*, 41 (2007), pp. 111–116.
- [4] J. M. ALEXANDER, I. BAB, S. FISH, R. MÜLLER, T. UCHIYAMA, G. GRONOWICZ, M. NAHOUNOU, Q. ZHAO, D. W. WHITE, M. CHOREV, D. GAZIT, AND M. ROSENBLATT, *Human parathyroid hormone 1-34 reverses bone loss in ovariectomized mice*, *Journal of Bone and Mineral Research*, 16 (2001), pp. 1665–1673.
- [5] ALTAIR, *Shrink wrap mesh*, https://connect.altair.com/CP/SA/training/self_paced/aero_v13/content/chapter6/shrinkwrap.htm, (Last access on 2018-06-09).
- [6] S. L. ANSORGE HL, *Mechanical properties of the developing rat achilles tendon*, 55th Annual Meeting of the Orthopaedic Research Society, (2009).
- [7] M. N. BAJURI, H. ISAKSSON, P. ELIASSON, AND M. S. THOMPSON, *A hyperelastic fibre-reinforced continuum model of healing tendons with distributed collagen fibre orientations*, *Biomechanics and Modeling in Mechanobiology*, 15 (2016), pp. 1457–1466.
- [8] C. B. BARBER, D. P. DOBKIN, AND H. HUHDANPAA, *The quickhull algorithm for convex hulls*, *ACM Transactions on Mathematical Software*, 22 (1996), pp. 469–483.
- [9] A. BARBIER, C. MARTEL, M. C. DE VERNEJOU, F. TIRODE, M. NYS, G. MOCAER, C. MORIEUX, H. MURAKAMI, AND F. LACHERETZ, *The visualization and evaluation of bone architecture in the rat using three-dimensional x-ray microcomputed tomography*, *Journal of Bone and Mineral Metabolism*, 17 (1999), pp. 37–44.
- [10] D. A. BENDER, *Metabolism on-line : the virtual tutorial room*, <https://www.david-bender.co.uk/metabonline/central/musclefuels/fuels13.html>, (Last access on 2018-05-02).
- [11] M. BENJAMIN, P. THEOBALD, D. SUZUKI, AND H. TOUMI, *The anatomy of the achilles tendon*, <http://eknygos.lsmuni.lt/springer/503/5-16.pdf>, (Last access on 2018-05-22).
- [12] A. BIEWENER, *Tendons and ligaments: Structure, mechanical behavior and biological function*, in *Collagen*, Springer US, pp. 269–284.
- [13] BODYTOMY, *Cartilage function*, <https://bodytomy.com/cartilage-function>, (Last access on 2018-05-28).
- [14] BONE&SPINE, *Haglund deformity – symptoms and treatment*, <http://boneandspine.com/haglund-deformity-symptoms-and-treatment/>, (Last access on 2018-05-24).

- [15] N. BONNET, N. LAROCHE, L. VICO, E. DOLLEANS, D. COURTEIX, AND C. L. BENHAMOU, *Assessment of trabecular bone microarchitecture by two different x-ray microcomputed tomographs: A comparative study of the rat distal tibia using skyscan and scanco devices*, Medical Physics, 36 (2009), pp. 1286–1297.
- [16] M. L. BOUXSEIN, S. K. BOYD, B. A. CHRISTIANSEN, R. E. GULDBERG, K. J. JEPSEN, AND R. MÜLLER, *Guidelines for assessment of bone microstructure in rodents using micro-computed tomography*, Journal of Bone and Mineral Research, 25 (2010), pp. 1468–1486.
- [17] S. K. BOYD AND R. MÜLLER, *Smooth surface meshing for automated finite element model generation from 3d image data*, Journal of Biomechanics, 39 (2006), pp. 1287–1295.
- [18] H. M. BRITZ, J. JOKIHAARA, O. V. LEPPÄNEN, T. L. N. JÄRVINEN, AND D. M. L. COOPER, *The effects of immobilization on vascular canal orientation in rat cortical bone*, Journal of Anatomy, 220 (2011), pp. 67–76.
- [19] BRUKER, *Micro ct for sample scanning: Skyscan-1272*, <https://www.bruker.com/products/microtomography/micro-ct-for-sample-scanning/skyscan-1272/overview.html>, (Last access on 2018-05-02).
- [20] D. B. BURR, *Anatomy and physiology of the mineralized tissues: Role in the pathogenesis of osteoarthritis*, Osteoarthritis and Cartilage, 12 (2004), pp. 20–30.
- [21] S. CASTAÑEDA, J. A. ROMAN-BLAS, R. LARGO, AND G. HERRERO-BEAUMONT, *Subchondral bone as a key target for osteoarthritis treatment*, Biochemical Pharmacology, 83 (2012), pp. 315–323.
- [22] D. CHAPPARD, N. RETAILLEAU-GABORIT, E. LEGRAND, M. F. BASLÉ, AND M. AUDRAN, *Comparison insight bone measurements by histomorphometry and CT*, Journal of Bone and Mineral Research, 20 (2005), pp. 1177–1184.
- [23] B. C. Y. CHENG, H. YU, H. GUO, T. SU, X.-Q. FU, T. LI, H.-H. CAO, A. K.-W. TSE, Z.-Z. WU, H.-Y. KWAN, AND Z.-L. YU, *A herbal formula comprising rosae multiflorae fructus and lonicerae japonicae flos, attenuates collagen-induced arthritis and inhibits TLR4 signalling in rats*, Scientific Reports, 6 (2016).
- [24] D. CHRISTIANO, *What's the difference between ligaments and tendons?*, <https://www.healthline.com/health/ligament-vs-tendon>, (Last access on 2018-05-23).
- [25] C. CIANI, S. B. DOTY, AND S. P. FRITTON, *An effective histological staining process to visualize bone interstitial fluid space using confocal microscopy*, Bone, 44 (2009), pp. 1015–1017.
- [26] T. O. CLANTON, *Iffas symposium3: Haglund deformity and insertional achilles tendon disease*, <https://www.aofas.org/PRC/meeting/Documents/iffassymposium3saturday1105clanton.pdf>, (2014).
- [27] B. CLARKE, *Normal bone anatomy and physiology*, Clinical Journal of the American Society of Nephrology, 3 (2008), pp. S131–S139.
- [28] I. CORRY, J. WEBB, A. CLINGELEFFER, AND L. PINCZEWSKI, *Arthroscopic reconstruction of the anteriorcruciate ligament. a comparison of patellar tendon autograft and four-strand hamstring tendon autograft.*, Am. J. Sports Med, (1999).
- [29] K. A. DANELSON, *The effect of strain and age on the mechanical properties of rat achilles tendons*, Muscles, Ligaments and Tendons Journal, 7 (2017), p. 548.

- [30] R. R. DE OLIVEIRA, K. D. S. DE LIRA, P. V. DE CASTRO SILVEIRA, M. P. G. COUTINHO, M. N. MEDEIROS, M. F. H. B. I. TEIXEIRA, AND S. R. A. DE MORAES, *Mechanical properties of achilles tendon in rats induced to experimental diabetes*, Annals of Biomedical Engineering, 39 (2011), pp. 1528–1534.
- [31] M. DOUBE, M. M. KŁOSOWSKI, I. ARGANDA-CARRERAS, F. P. CORDELIÈRES, R. P. DOUGHERTY, J. S. JACKSON, B. SCHMID, J. R. HUTCHINSON, AND S. J. SHEFELBINE, *BoneJ: Free and extensible bone image analysis in ImageJ*, Bone, 47 (2010), pp. 1076–1079.
- [32] R. L. DUNCAN AND C. H. TURNER, *Mechanotransduction and the functional response of bone to mechanical strain*, Calcified Tissue International, 57 (1995), pp. 344–358.
- [33] P. ELIASSON, T. ANDERSSON, AND P. ASPENBERG, *Rat achilles tendon healing: mechanical loading and gene expression*, Journal of Applied Physiology, 107 (2009), pp. 399–407.
- [34] D. ERROI, *Conservative treatment for insertional achilles tendinopathy: platelet-rich plasma and focused shock waves. a retrospective study*, Muscle, Ligaments and Tendons Journal, 7 (2017), p. 98.
- [35] Z. FAN, J. G. SWADENER, J. Y. RHO, M. E. ROY, AND G. M. PHARR, *Anisotropic properties of human tibial cortical bone as measured by nanoindentation*, Journal of Orthopaedic Research, 20 (2002), pp. 806–810.
- [36] M. I. FANUSCU AND T.-L. CHANG, *Three-dimensional morphometric analysis of human cadaver bone: microstructural data from maxilla and mandible*, Clinical Oral Implants Research, 15 (2004), pp. 213–218.
- [37] K. FICEK, J. FILIPEK, J. FICEK, M. MUZALEWSKA, AND F. HUMPA, *Calcaneal CT is a useful tool for identifying achilles tendon disorders: a pilot study*, Journal of Orthopaedic Surgery and Research, 12 (2017).
- [38] P. FRATZL AND R. WEINKAMER, *Nature's hierarchical materials*, Progress in Materials Science, 52 (2007), pp. 1263–1334.
- [39] M. FRIEDMAN, O. SHERMAN, J. FOX, W. D. PIZZO, S. SNYDER, AND R. FERKEL, *Autogeneic anteriorcruciate ligament (acl) anterior reconstruction of the knee. a review.*, Clin Orthop Relat Res., (1985).
- [40] L. M. GALATZ, C. M. BALL, S. A. TEEFEY, W. D. MIDDLETON, AND K. YAMAGUCHI, *The outcome and repair integrity of completely arthroscopically repaired large and massive rotator cuff tears*, The Journal of Bone & Joint Surgery, 86 (2004), pp. 219–224.
- [41] G. M. GENIN, A. KENT, V. BIRMAN, B. WOPENKA, J. D. PASTERIS, P. J. MARQUEZ, AND S. THOMOPOULOS, *Functional grading of mineral and collagen in the attachment of tendon to bone*, Biophysical Journal, 97 (2009), pp. 976–985.
- [42] J. A. GIMBEL, *Long durations of immobilization in the rat result in enhanced mechanical properties of the healing supraspinatus tendon insertion site*, Journal of Biomechanical Engineering, 129 (2006), p. 400.
- [43] J. A. GIMBEL, S. MEHTA, J. P. V. KLEUNEN, G. R. WILLIAMS, AND L. J. SOSLOWSKY, *The tension required at repair to reappose the supraspinatus tendon to bone rapidly increases after injury*, Clinical Orthopaedics and Related Research, 426 (2004), pp. 258–265.
- [44] M. B. GOLDRING AND S. R. GOLDRING, *Articular cartilage and subchondral bone in the pathogenesis of osteoarthritis*, Annals of the New York Academy of Sciences, 1192 (2010), pp. 230–237.
- [45] R. E. W. GONZALEZ, R. C. AND S. L. EDDINS, *Digital image processing using matlab*, New Jersey, Pearson Prentice Hall, (2004).

- [46] GROWINGUP, *Child bone growth*, <http://www.growingup.net/worried-about-your-childs-growth/about-growth>, (Last access on 2018-05-23).
- [47] X. E. GUO AND S. A. GOLDSTEIN, *Vertebral trabecular bone microscopic tissue elastic modulus and hardness do not change in ovariectomized rats*, *Journal of Orthopaedic Research*, 18 (2000), pp. 333–336.
- [48] HEALTHJADE, *Muscle anatomy*, <https://healthjade.com/muscle/>, (Last access on 2018-05-23).
- [49] K. M. HEINEMEIER, D. SKOVGAARD, M. L. BAYER, K. QVORTRUP, A. KJAER, M. KJAER, S. P. MAGNUSSON, AND M. KONGSGAARD, *Uphill running improves rat achilles tendon tissue mechanical properties and alters gene expression without inducing pathological changes*, *Journal of Applied Physiology*, 113 (2012), pp. 827–836.
- [50] H. HEMMATIAN, M. R. LAURENT, S. GHAZANFARI, D. VANDERSCHUEREN, A. D. BAKKER, J. KLEIN-NULEND, AND G. H. VAN LENTHE, *Accuracy and reproducibility of mouse cortical bone microporosity as quantified by desktop microcomputed tomography*, *PLOS ONE*, 12 (2017), p. e0182996.
- [51] S. HENGESBERGER, P. AMMANN, B. LEGROS, R. RIZZOLI, AND P. ZYSSET, *Intrinsic bone tissue properties in adult rat vertebrae: modulation by dietary protein*, *Bone*, 36 (2005), pp. 134–141.
- [52] H. A. HOGAN, S. P. RUHMANN, AND H. W. SAMPSON, *The mechanical properties of cancellous bone in the proximal tibia of ovariectomized rats*, *Journal of Bone and Mineral Research*, 15 (2010), pp. 284–292.
- [53] HOWTORELIEF, *Ankle joint: Anatomy, movement & muscle involvement*, <http://howtorelief.com/ankle-joint-anatomy-overview/>, (Last access on 2018-05-23).
- [54] Y. HU, V. BIRMAN, A. DEYMER-BLACK, A. G. SCHWARTZ, S. THOMOPOULOS, AND G. M. GENIN, *Stochastic interdigitation as a toughening mechanism at the interface between tendon and bone*, *Biophysical Journal*, 108 (2015), pp. 431–437.
- [55] HYPERWORKS, *Hypermesh 10.0 release notes, shrink wrap*, https://connect.altair.com/CP/SA/training/self_paced/aero_v13/content/chapter6/shrinkwrap.htm, (Last access on 2018-06-09).
- [56] IOF, *Introduction to bone biology: all about our bones*, International Osteoporosis Foundation, <https://www.iofbonehealth.org/introduction-bone-biology-all-about-our-bones>, (Last access on 2018-05-23).
- [57] IPFH, *Haglund's deformity*, <https://www.ipfh.org/foot-conditions/foot-conditions-a-z/haglunds-deformity>, (Last access on 2018-05-24).
- [58] I. JANZEN, *The jacobian: finite element mesh quality*, <http://www.isaiahjanzen.com/2012/08/the-jacobian-finite-element-mesh-quality.html>, (Last access on 2018-06-09).
- [59] K. J. J. JOHANSSON, J. J. SARIMO, L. L. LEMPAINEN, T. LAITALA-LEINONEN, AND S. Y. ORAVA, *Calcific spurs at the insertion of the achilles tendon: a clinical and histological study*, *Muscles, Ligaments and Tendons Journal*, (2012).
- [60] P. JØRGENSEN, B. BAK, AND T. ANDREASSEN, *Mechanical properties and biochemical composition of rat cortical femur and tibia after long-term treatment with biosynthetic human growth hormone*, *Bone*, 12 (1991), pp. 353–359.
- [61] P. KAH, R. SUORANTA, J. MARTIKAINEN, AND C. MAGNUS, *Techniques for joining dissimilar materials: metals and polymers*, *Rev. Adv. Mater.*, (2013).
- [62] S. KANG, D. B. THORDARSON, AND T. P. CHARLTON, *Insertional achilles tendinitis and haglund's deformity*, *Foot & Ankle International*, 33 (2012), pp. 487–491.

- [63] G. KERCKHOFS, G. PYKA, M. MOESEN, S. V. BAE, J. SCHROOTEN, AND M. WEVERS, *High-resolution microfocus x-ray computed tomography for 3d surface roughness measurements of additive manufactured porous materials*, *Advanced Engineering Materials*, 15 (2012), pp. 153–158.
- [64] H. KHAYYERI, P. BLOMGRAN, M. HAMMERMAN, M. J. TURUNEN, A. LÖWGREN, M. GUIZAR-SICAÍROS, P. ASPENBERG, AND H. ISAKSSON, *Achilles tendon compositional and structural properties are altered after unloading by botox*, *Scientific Reports*, 7 (2017).
- [65] H. KHAYYERI, A. GUSTAFSSON, A. HEUIJERJANS, M. K. MATIKAINEN, P. JULKUNEN, P. ELIASSON, P. ASPENBERG, AND H. ISAKSSON, *A fibre-reinforced poroviscoelastic model accurately describes the biomechanical behaviour of the rat achilles tendon*, *PLOS ONE*, 10 (2015).
- [66] J. L. KUHN, S. A. GOLDSTEIN, L. A. FELDKAMP, R. W. GOULET, AND G. JESION, *Evaluation of a microcomputed tomography system to study trabecular bone structure*, *Journal of Orthopaedic Research*, 8 (1990), pp. 833–842.
- [67] G. LI, J. YIN, J. GAO, T. S. CHENG, N. J. PAVLOS, C. ZHANG, AND M. H. ZHENG, *Subchondral bone in osteoarthritis: insight into risk factors and microstructural changes*, *Arthritis Research & Therapy*, 15 (2013), p. 223.
- [68] M. A. LIEBSCHNER, *Biomechanical considerations of animal models used in tissue engineering of bone*, *Biomaterials*, 25 (2004), pp. 1697–1714.
- [69] Y. LIU, V. BIRMAN, C. CHEN, S. THOMOPOULOS, AND G. M. GENIN, *Mechanisms of bimaternal attachment at the interface of tendon to bone*, *Journal of Engineering Materials and Technology*, 133 (2011), p. 011006.
- [70] Y. LIU, S. THOMOPOULOS, V. BIRMAN, J.-S. LI, AND G. GENIN, *Bi-material attachment through a compliant interfacial system at the tendon-to-bone insertion site*, *Mechanics of Materials*, 44 (2012), pp. 83–92.
- [71] R. C. LOCKE, A. C. ABRAHAM, AND M. L. KILLIAN, *Orthopedic interface repair strategies based on native structural and mechanical features of the multiscale enthesis*, *ACS Biomaterials Science & Engineering*, 3 (2016), pp. 2633–2643.
- [72] H. H. LU AND S. THOMOPOULOS, *Functional attachment of soft tissues to bone: Development, healing, and tissue engineering*, *Annual Review of Biomedical Engineering*, 15 (2013), pp. 201–226.
- [73] J. LYSHOLM AND J. WIKLANDER, *Injuries in runners*, *The American Journal of Sports Medicine*, 15 (1987), pp. 168–171.
- [74] H. MADRY, C. N. VAN DIJK, AND M. MUELLER-GERBL, *The basic science of the subchondral bone*, *Knee Surgery, Sports Traumatology, Arthroscopy*, 18 (2010), pp. 419–433.
- [75] F. MALEKIPOUR, C. WHITTON, D. OETOMO, AND P. V. S. LEE, *Shock absorbing ability of articular cartilage and subchondral bone under impact compression*, *Journal of the Mechanical Behavior of Biomedical Materials*, 26 (2013), pp. 127–135.
- [76] J. MAQUIRRIAIN, *Achilles tendon rupture: Avoiding tendon lengthening during surgical repair and rehabilitation*, *Yale Journal of Biology and Medicine*, (2011).
- [77] MATHWORKS, *Regionprops function documentation*, <https://au.mathworks.com/help/images/ref/regionprops.html>, (Last access on 2018-06-05).
- [78] M. R. MBChB, M. O. E. D’ALTON MBChB, (PRET), M. N. R.G. GOLELE, AND F. O. S. MF GP (SA), MMED (ORTH), *Avulsion fracture of the calcaneal tuberosity: A soft tissue complication from delayed treatment*, *The Foot and Ankle Online Journal*, (2010).

- [79] S. J. MELLON AND K. E. TANNER, *Bone and its adaptation to mechanical loading: a review*, International Materials Reviews, 57 (2012), pp. 235–255.
- [80] S. MILZ, A. RUFAT, A. BUETTNER, R. PUTZ, J. R. RALPHS, AND M. BENJAMIN, *Three-dimensional reconstructions of the achilles tendon insertion in man*, Journal of Anatomy, 200 (2002), pp. 145–152.
- [81] K. L. MOFFAT, W.-H. S. SUN, P. E. PENA, N. O. CHAHINE, S. B. DOTY, G. A. ATESHIAN, C. T. HUNG, AND H. H. LU, *Characterization of the structure-function relationship at the ligament-to-bone interface*, Proceedings of the National Academy of Sciences, 105 (2008), pp. 7947–7952.
- [82] MUSCULOSKELETALKEY, *Structure and function of the ankle and foot*, <https://musculoskeletalkey.com/structure-and-function-of-the-ankle-and-foot/>, (Last access on 2018-05-23).
- [83] R. MÜLLER, H. V. CAMPENHOUT, B. V. DAMME, G. V. DER PERRE, J. DEQUEKER, T. HILDEBRAND, AND P. RÜEGSEGG, *Morphometric analysis of human bone biopsies: A quantitative structural comparison of histological sections and micro-computed tomography*, Bone, 23 (1998), pp. 59–66.
- [84] R. MÜLLER, M. KAMPSCHULTE, T. E. KHASSAWNA, G. SCHLEWITZ, B. HÜRTER, W. BÖCKER, M. BOBETH, A. C. LANGHEINRICH, C. HEISS, A. DEUTSCH, AND G. CUNIBERTI, *Change of mechanical vertebrae properties due to progressive osteoporosis: combined biomechanical and finite-element analysis within a rat model*, Medical & Biological Engineering & Computing, 52 (2014), pp. 405–414.
- [85] NEWSMEDICAL, *What is cartilage*, <https://www.news-medical.net/health/What-is-Cartilage.aspx>, (Last access on 2018-05-28).
- [86] G. NOURISSAT, A. DIOP, N. MAUREL, C. SALVAT, S. DUMONT, A. PIGENET, M. GOSSET, X. HOUARD, AND F. BERENBAUM, *Mesenchymal stem cell therapy regenerates the native bone-tendon junction after surgical repair in a degenerative rat model*, PLoS ONE, 5 (2010), p. e12248.
- [87] R. OFTADEH, V. ENTEZARI, G. SPORRI, J. C. VILLA-CAMACHO, H. KRIGBAUM, E. STRAWICH, L. GRAHAM, C. REY, H. CHIU, R. MULLER, H. N. HASHEMI, A. VAZIRI, AND A. NAZARIAN, *Hierarchical analysis and multi-scale modelling of rat cortical and trabecular bone*, Journal of The Royal Society Interface, 12 (2015), pp. 20150070–20150070.
- [88] H. OGUMA, G. MURAKAMI, H. TAKAHASHI-IWANAGA, M. AOKI, AND S. ISHII, *Early anchoring collagen fibers at the bone-tendon interface are conducted by woven bone formation: light microscope and scanning electron microscope observation using a canine model*, Journal of Orthopaedic Research, 19 (2001).
- [89] Y. OSHRI, E. PALMANOVICH, Y. S. BRIN, R. KARP, S. MASSARWE, B. KISH, AND M. NYSKA, *Chronic insertional achilles tendinopathy: surgical outcomes*, Muscles, Ligaments and Tendons Journal, 2.
- [90] P. E. PALACIO-MANCHENO, A. I. LARRIERA, S. B. DOTY, L. CARDOSO, AND S. P. FRITTON, *3d assessment of cortical bone porosity and tissue mineral density using high-resolution μ CT: Effects of resolution and threshold method*, Journal of Bone and Mineral Research, 29 (2013), pp. 142–150.
- [91] PERKINELMER, *Phase contrast micro-computed tomography imaging of murine soft tissue using an edge illumination approach*, World Molecular Imaging Congress (WMIC), (2017).
- [92] PHYSIOPEDIA, *Foot and ankle structure and function*, https://www.physio-pedia.com/Foot_and_Ankle_Structure_and_Function#Metatarsophalangeal_.28MTP.29_Joints_and_Interphalangeal_.28IP.29_Joints, (Last access on 2018-05-23).

- [93] ———, *Tendon anatomy*, https://www.physio-pedia.com/Tendon_Anatomy, (Last access on 2018-05-23).
- [94] PROCARE, *Heel pain perth*, <https://www.procarepodiatry.com.au/heel-pain-perth/>, (Last access on 2018-05-23).
- [95] RADIOPAEDIA, *From the case: Normal foot x-rays*, <https://radiopaedia.org/images/12509481>, (Last access on 2018-05-23).
- [96] M. RAJCAKOWSKA, D. STEFANIUK, AND M. SOBÓTKA, *Roughness analysis of the “invisible” surface by means of x-ray micro-ct*.
- [97] S. D. RAWSON, L. MARGETTS, J. K. F. WONG, AND S. H. CARTMELL, *Sutured tendon repair a multi-scale finite element model*, *Biomechanics and Modeling in Mechanobiology*, 14 (2014), pp. 123–133.
- [98] D. ROBERSTON, D. DANIEL, AND E. BIDEN, *Soft tissue fixation to bone*, *Am. J. Sports Med.*
- [99] L. ROSSETTI, L. A. KUNTZ, E. KUNOLD, J. SCHOCK, K. W. MÜLLER, H. GRABMAYR, J. STOLBERG-STOLBERG, F. PFEIFFER, S. A. SIEBER, R. BURKART, AND A. R. BAUSCH, *The microstructure and micromechanics of the tendon–bone insertion*, *Nature Materials*, 16 (2017), pp. 664–670.
- [100] W. ROUX, *Gesammelte abhandlungen*, *Monatshefte für Mathematik und Physik*, 25 (1914), pp. A30–A31.
- [101] D. RUFFONI, *Biomechanics (slides)*, University of Liege, (2016).
- [102] P. SAPARIN, H. SCHERF, J.-J. HUBLIN, P. FRATZL, AND R. WEINKAMER, *Structural adaptation of trabecular bone revealed by position resolved analysis of proximal femora of different primates*, *The Anatomical Record: Advances in Integrative Anatomy and Evolutionary Biology*, 294 (2010), pp. 55–67.
- [103] P. SAPARIN, J. S. THOMSEN, J. KURTHS, G. BELLER, AND W. GOWIN, *Segmentation of bone CT images and assessment of bone structure using measures of complexity*, *Medical Physics*, 33 (2006), pp. 3857–3873.
- [104] N. SHANKS, R. GREEK, AND J. GREEK, *Are animal models predictive for humans?*, *Philosophy, Ethics, and Humanities in Medicine*, 4 (2009), p. 2.
- [105] T. SHEARER, *A new strain energy function for the hyperelastic modelling of ligaments and tendons based on fascicle microstructure*, *Journal of Biomechanics*, 48 (2015), pp. 290–297.
- [106] V. B. SHIM, J. W. FERNANDEZ, P. B. GAMAGE, C. REGNERY, D. W. SMITH, B. S. GARDINER, D. G. LLOYD, AND T. F. BESIÉ, *Subject-specific finite element analysis to characterize the influence of geometry and material properties in achilles tendon rupture*, *Journal of Biomechanics*, 47 (2014), pp. 3598–3604.
- [107] SINEW THERAPEUTICS, *Achilles tendon bursitis*, <https://sinewtherapeutics.com/achilles-tendon-bursitis-information.html>, (Last access on 2018-05-24).
- [108] A. SOCIETY, *Insertional achilles tendinitis*, <http://www.aofas.org/footcaremd/conditions/ailments-of-the-ankle/Pages/Insertional-Achilles-Tendinitis.aspx>, (Last access on 2018-05-22).
- [109] L. J. SOSLOWSKY, J. E. CARPENTER, C. M. DEBANO, I. BANERJI, AND M. R. MOALLI, *Development and use of an animal model for investigations on rotator cuff disease*, *Journal of Shoulder and Elbow Surgery*, 5 (1996), pp. 383–392.
- [110] J. P. SPALAZZI, A. L. BOSKEY, N. PLESHKO, AND H. H. LU, *Quantitative mapping of matrix content and distribution across the ligament-to-bone insertion*, *PLoS ONE*, 8 (2013), p. e74349.

- [111] R. TAYLOR, RITZ, AND GALERKIN, *The road to the finite element method*, IACM Expressions (12), (2002).
- [112] S. THOMOPOULOS, *Tendon to bone healing: Differences in biomechanical, structural, and compositional properties due to a range of activity levels*, Journal of Biomechanical Engineering, 125 (2003), p. 106.
- [113] S. THOMOPOULOS, V. BIRMAN, AND G. M. GENIN, *The challenge of attaching dissimilar materials*, in Structural Interfaces and Attachments in Biology, Springer New York, aug 2012, pp. 3–17.
- [114] —, eds., *Structural Interfaces and Attachments in Biology*, Springer New York, 2013.
- [115] S. THOMOPOULOS, J. P. MARQUEZ, B. WEINBERGER, V. BIRMAN, AND G. M. GENIN, *Collagen fiber orientation at the tendon to bone insertion and its influence on stress concentrations*, Journal of Biomechanics, 39 (2006), pp. 1842–1851.
- [116] S. THOMOPOULOS, G. R. WILLIAMS, J. A. GIMBEL, M. FAVATA, AND L. J. SOSLOWSKY, *Variation of biomechanical, structural, and compositional properties along the tendon to bone insertion site*, Journal of Orthopaedic Research, 21 (2003), pp. 413–419.
- [117] C. TURNER, *Three rules for bone adaptation to mechanical stimuli*, Bone, 23 (1998), pp. 399–407.
- [118] P. B. VOLETI, M. R. BUCKLEY, AND L. J. SOSLOWSKY, *Tendon healing: Repair and regeneration*, Annual Review of Biomedical Engineering, 14 (2012), pp. 47–71.
- [119] M. C. VULPIANI, M. GUZZINI, AND A. FERRETTI, *Operative treatment of chronic achilles tendinopathy*, International Orthopaedics, 27 (2003), pp. 307–310.
- [120] J. H. WAARSING, J. S. DAY, AND H. WEINANS, *An improved segmentation method for in vivo CT imaging*, Journal of Bone and Mineral Research, 19 (2004), pp. 1640–1650.
- [121] D. WEBSTER, E. WASSERMAN, M. EHRBAR, F. WEBER, I. BAB, AND R. MÜLLER, *Mechanical loading of mouse caudal vertebrae increases trabecular and cortical bone mass-dependence on dose and genotype*, Biomechanics and Modeling in Mechanobiology, 9 (2010), pp. 737–747.
- [122] D. WEBSTER, A. WIRTH, G. H. VAN LENTHE, AND R. MÜLLER, *Experimental and finite element analysis of the mouse caudal vertebrae loading model: prediction of cortical and trabecular bone adaptation*, Biomechanics and Modeling in Mechanobiology, 11 (2011), pp. 221–230.
- [123] WIKIPEDIA, *Cartilage*, <https://fr.wikipedia.org/wiki/Cartilage>.
- [124] —, *Epoxy*, <https://en.wikipedia.org/wiki/Epoxy>, (Last access on 2018-05-02).
- [125] —, *Fixation (histology)*, [https://en.wikipedia.org/wiki/Fixation_\(histology\)](https://en.wikipedia.org/wiki/Fixation_(histology)), (Last access on 2018-05-02).
- [126] —, *Achilles tendon*, https://en.wikipedia.org/wiki/Achilles_tendon, (Last access on 2018-05-23).
- [127] —, *Anterior cruciate ligament*, https://en.wikipedia.org/wiki/Anterior_cruciate_ligament, (Last access on 2018-05-23).
- [128] —, *Bone*, <https://en.wikipedia.org/wiki/Bone>, (Last access on 2018-05-23).
- [129] —, *Osteon*, <https://en.wikipedia.org/wiki/Osteon>, (Last access on 2018-05-23).
- [130] —, *Calcaneal spur*, https://en.wikipedia.org/wiki/Calcaneal_spur, (Last access on 2018-05-24).

- [131] ———, *Collagen*, <https://en.wikipedia.org/wiki/Collagen>, (Last access on 2018-05-24).
- [132] J. WOLFF, *Das gesetz der transformation der knochen*, DMW - Deutsche Medizinische Wochenschrift, 19 (1893), pp. 1222–1224.
- [133] B. WOPENKA, A. KENT, J. D. PASTERIS, Y. YOON, AND S. THOMOPOULOS, *The tendon-to-bone transition of the rotator cuff: A preliminary raman spectroscopic study documenting the gradual mineralization across the insertion in rat tissue samples*, Applied Spectroscopy, 62 (2008), pp. 1285–1294.
- [134] K. YIP, *The rotator cuff*, <http://www.orthopaedicclinic.com.sg/shoulder/the-rotator-cuff-2/>, (Last access on 2018-05-23).
- [135] L. ZHAO, A. THAMBYAH, AND N. D. BROOM, *A multi-scale structural study of the porcine anterior cruciate ligament tibial enthesis*, Journal of Anatomy, 224 (2014), pp. 624–633.
- [136] Q. ZUO, S. LU, Z. DU, T. FRIIS, J. YAO, R. CRAWFORD, I. PRASADAM, AND Y. XIAO, *Characterization of nano-structural and nano-mechanical properties of osteoarthritic subchondral bone*, BMC Musculoskeletal Disorders, 17 (2016).